The RESEARCH LABORATORY
of
ELECTRONICS
at the
MASSACHUSETTS INSTITUTE OF TECHNOLOGY
CAMBRIDGE, MASSACHUSETTS 02139

A Touch Lab Report

Encoding and Decoding of Shape in Tactile Sensing

Balasundara I. Raju and Mandayam A. Srinivasan

RLE Technical Report No. 630

September 1999

A Touch Lab Report

Encoding and Decoding of Shape in Tactile Sensing

Balasundara I. Raju and Mandayam A. Srinivasan

RLE Technical Report No. 630

September 1999

This work has been supported through NIH grant NS33778 and the NSF Pittsburgh Supercomputer Center grant MSS940007P.

The Research Laboratory *of* Electronics
MASSACHUSETTS INSTITUTE OF TECHNOLOGY
CAMBRIDGE, MASSACHUSETTS 02139-4307

Encoding and Decoding of Shape in Tactile Sensing

by

Balasundara I. Raju

Submitted to the Department of Mechanical Engineering
on January 16, 1998, in partial fulfillment of the
requirements for the degree of
Master of Science in Mechanical Engineering

Abstract

This thesis is concerned with the biomechanical bases of tactile sensing and their implications to neural response of Slowly Adapting Type-I (SA-I) mechanoreceptors in the skin. In addition, possible non-linear mechanisms used by the central nervous system (CNS) for decoding tactile information from the afferent nerve fibers were also investigated.

To investigate the mechanics of touch, a high resolution three dimensional multilayered finite element model of a primate fingerpad was developed. Predictions of the model matched empirically obtained surface displacements very well, thereby validating its biomechanical behavior. The model was used to simulate static indentation of the fingertip by rigid objects of different shapes such as rectangular bars, cylinders, and sinusoidal step shapes. The corresponding surface pressure distribution was found to be highly dependent on the curvature of the object that indented the finger. A simple model for surface pressure as a function of the indenting object's curvature and the local depth of indentation was developed. To study the mechanism of transduction by the mechanoreceptors (transformation of the mechanical stress state into neural signals), 18 mechanical quantities were obtained from the calculated stress and strain tensors, and were matched with experimentally recorded neural response data. Three quantities – maximum compressive strain, maximum tensile strain and strain energy density – were found to be related to the neural responses of SA-I nerve fibers through a simple scaling-threshold model and are thus considered to be possible *relevant stimuli* for SA-I afferents.

To investigate the inverse problem of decoding (computation of surface loads from neural response) by the CNS, a non-linear shift-invariant system for modeling the encoding process, which treats the surface pressure as input and neural responses as output, was developed. Because of the non-linearities due to the relevant stimulus measures and threshold parameter, a simple inverse transformation cannot be applied. A signal estimation algorithm using the univariate non-linear optimization technique was employed to decode the surface pressure from the neural responses. The decoding was demonstrated for both the ideal case where no sensor noise is present, as well as the case where the sensor noise (assumed to be additive Gaussian) is present, as long as the signal-to-noise ratio is greater than 20 dB.

Thesis supervisor: Dr. Mandayam A. Srinivasan
Title: Principal Research Scientist

Contents

1 Introduction 10
- 1.1 Overview . . . 10
- 1.2 Motivation . . . 11
- 1.3 Thesis Overview . . . 12

2 Background 14
- 2.1 Anatomy of the Human Fingertip . . . 14
  - 2.1.1 Fingertip skin . . . 15
  - 2.1.2 Mechanoreceptors . . . 16
- 2.2 Previous Studies in Human Tactile Sensing . . . 17
  - 2.2.1 Neurophysiological studies . . . 18
  - 2.2.2 Psychophysical studies . . . 19
  - 2.2.3 Biomechanical Studies . . . 20
  - 2.2.4 Systems Approach . . . 21
- 2.3 Need for Further Studies . . . 21
- 2.4 Description of Object's Shape . . . 22

3 Development of High Resolution Finite Element Model 24
- 3.1 Need for an Optimum High Resolution Model . . . 24
- 3.2 Development of the Solid Model . . . 25
- 3.3 Development of the Finite Element Model . . . 27
- 3.4 Verification of the Model . . . 29

4 Mechanical Signals in Tactile Sensing 31
- 4.1 Motivation . . . 31
- 4.2 Methods . . . 33
  - 4.2.1 Three dimensional finite element models . . . 33
  - 4.2.2 Simulations . . . 33
- 4.3 Results . . . 35
  - 4.3.1 Surface pressure distributions caused by rectangular bars . . . 35
  - 4.3.2 Surface pressure distributions caused by cylindrical shapes . . . 38
  - 4.3.3 Surface pressure distributions caused by sinusoidal step shapes . . . 40
  - 4.3.4 Subsurface strain measures . . . 44
  - 4.3.5 Dependence of surface pressure and subsurface strain measures on the shape of the object . . . 48
  - 4.3.6 Relationship between surface pressure and object curvature . . . 49
- 4.4 Discussion . . . 49
  - 4.4.1 Surface pressure . . . 49

4.4.2 Subsurface strain measures . . . 53
4.4.3 Receptor depths . . . 53

5 Relevant Stimulus **55**
5.1 Motivation . . . 55
5.2 Methods . . . 55
5.2.1 Simulation of neurophysiological experiments involving stimulus shapes indented onto the monkey finger pad . . . 55
5.2.2 Receptor locations . . . 57
5.2.3 Stress/Strain measures . . . 57
5.2.4 Comparison of recorded neural data and strain measures . . . 58
5.2.5 Generation of SSRP from population response . . . 59
5.3 Results . . . 61
5.3.1 Influence of force of indentation on the population response and SRP 61
5.3.2 Influence of receptor location on the SSRP . . . 63
5.3.3 Correlation coefficient is alone not a good indicator for determining relevant stimulus . . . 68
5.3.4 Determination of the relevant stimulus . . . 69
5.3.5 Goodness of fit for the four candidates based on step indentations . 71
5.3.6 Predicted neural response for step indentations . . . 72
5.3.7 Indentation by rectangular bars . . . 72
5.3.8 Goodness of fit for the four candidates based on bar indentations . 74
5.4 Discussion . . . 76

6 Decoding **79**
6.1 Linear Systems . . . 79
6.2 Shift-Invariant Systems . . . 80
6.3 Idealizations of the real system . . . 82
6.4 Illustration of Shift-Invariance . . . 83
6.5 System Identification using Impulse Response Functions . . . 86
6.6 Decoding as an Optimization Problem . . . 88
6.7 Example of Optimal Decoding using the Univariate Method . . . 90
6.8 Decoding in the Presence of Noise . . . 91
6.9 Summary of Systems Approach . . . 94

7 Summary and Future Work **96**
7.1 Summary . . . 96
7.1.1 Model development . . . 96
7.1.2 Biomechanical studies . . . 96
7.1.3 Neurophysiological studies . . . 97
7.1.4 Systems approach . . . 97
7.2 Future Work . . . 98

References **100**

List of Figures

1-1 Sequence of events leading to tactile sensing 11

2-1 The human fingertip 14
2-2 Mechanoreceptors innervating the human fingertip 16
2-3 Ramp and hold stimulus used to distinguish 4 types of mechanoreceptive afferents 18

3-1 Development of the solid model 26
3-2 3D finite element model of the primate fingertip 27
3-3 Line load indentation of the monkey fingertip 29

4-1 Surface pressure distributions due to indentation by a 3 mm wide rectangular bar 37
4-2 Surface pressure distributions due to indentation by a 1.5 mm wide rectangular bar 38
4-3 Surface pressure distributions due to indentation by cylinders 39
4-4 Surface pressure distributions due to indentation by step 1 42
4-5 Surface pressure distributions due to indentation by step 5 45
4-6 Subsurface strain measures for two different DOIs due to indentation by step 1 46
4-7 Subsurface strain measures for two different DOIs due to indentation by step 5 47
4-8 Dependence of surface pressure and subsurface strain measures on the shape of the object 50
4-9 Model for surface pressure as a function of local depth of indentationa and curvature of the object 51
4-10 Quantitative model for skin surface pressure under shaped objects 53

5-1 Experimentally recorded spatial response profile (SRP) for sinusoidal step and rectangular bar indentations 60
5-2 Extraction of simulated spatial response profile (SSRP) from the population response 61
5-3 Influence of force of indentation on the population response and the SSRPs 64
5-4 SSRPs for step 1 with maximum compressive strain as the candidate measure for 10 receptors 65
5-5 Step 1 SSRPs for three strains 66
5-6 Step 1 SSRPs for three stresses 67
5-7 Step 1 SSRP for three invariants 68
5-8 Receptor model based on recordings using step shapes 71
5-9 Comparison of predicted SRP and recorded SRP for the three step shapes . 73
5-10 SSRPs for indentation by 3 mm wide rectangular bar 74

5-11 SSRPs for indentation by 1.5 wide rectangular bar 75
5-12 Receptor model based on recordings using rectangular bars 76
5-13 Comparison of predicted SRP and recorded SRP for the two rectangular bars 77

6-1 Input-output model of the human tactile system 80
6-2 Illustration of shift-invariance 82
6-3 Locations of the point load used to test shift-invariance 84
6-4 Strain energy density distribution due to a point load. 85
6-5 Impulse response functions for e_{11}, e_{22} and e_{12} 88
6-6 Block diagram representation of the encoding process using impulse response functions 89
6-7 Algorithm describing the univariate method 91
6-8 Input x(n) and the corresponding output y(n) chosen to illustrate the working of the univariate method 92
6-9 Error function for the example problem 92
6-10 Working of the Univariate method 93
6-11 Decoding in the presence of noise 94
6-12 Percentage error in decoding as a function of SNR 95

List of Tables

2.1 Comparison of the four mechanoreceptors in the primate fingerpad 17

5.1 Correlation coefficients between SSRP and recorded SRP for three strain measures 69

5.2 Determination of relevant stimulus 70

6.1 Model parameters ($Sener = \frac{A}{r^m}$) for strain energy density for all the locations 86

Abbreviations

CNS - Central nervous system

DOI - Depth of indentation

PCL - Patran command language

SRP - Spatial response profile

SSRP - Simulated spatial response profile

Sener - Strain energy density

1 Introduction

1.1 Overview

This thesis is concerned with biomechanical bases of human tactile sensing, the implications of such a study to the neural behavior of mechanoreceptors embedded in the skin, and the development of systems approach to coding and decoding of tactile information.

Each of the five sensory systems in humans has unique features. The sense of touch is unique in that there is a direct interaction with the object being touched, unlike in vision, hearing, and smell, wherein the information source is located elsewhere. Certain properties of objects like mechanical compliance can be realized only through touch. Unlike in vision, hearing, or smell, during touch, one can modify the signals that are imposed on the skin by moving one's finger over the object and exploring it. A study of the human tactile system will lead to a better understanding of human interaction with surroundings and will also aid engineers in the development of tactile communication aids, teleoperation systems, intelligent robots and virtual environments.

The sequence of events resulting in human tactile sense can be divided into four events for the ease of analysis: First, the object contacts the skin and this leads to a distribution of forces on the skin surface. Second, these surface force distributions lead to sub-surface distributions of mechanical stresses and strains, depending on the mechanical filtering properties of the skin. Third, these stresses and strains are transduced into neural impulses by the mechanoreceptors in the skin. Finally, these neural impulses reach the brain where the object is perceived. Figure 1-1 shows the above sequence of events.

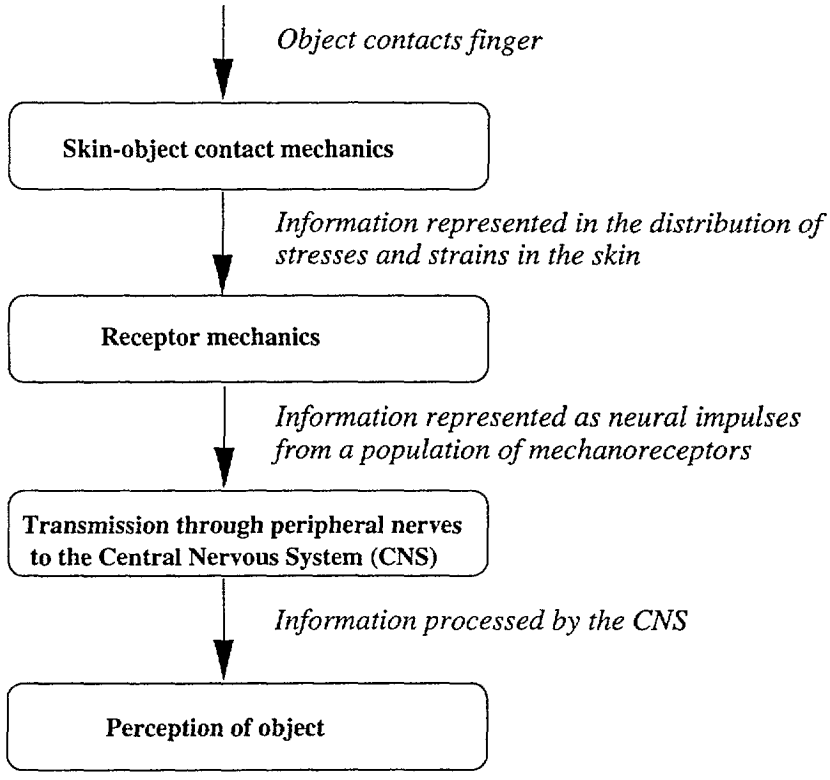

Figure 1-1: Sequence of events leading to tactile sensing.

Human tactile sensing has been studied mostly through neurophysiological studies (recording neural responses of peripheral nerves), psychophysical studies (evaluating responses of human subjects to tactile stimuli) or biomechanical studies (mechanistic modeling of fingerpad, determination of stress/strain measures etc.). Neurophysiological studies have provided information on the neural behavior of the mechanoreceptors and the peripheral nerves that innervate these receptors. Psychophysical studies have yielded insights on the relationship between the stimuli applied to the skin and the overall perception of humans. Biomechanical studies have sought to establish a link between the mechanics of contact between objects and the finger to neural recordings from afferent nerve fibers.

1.2 Motivation

An understanding of the human tactile system requires the understanding of each of the steps described in Figure 1-1. Though experimental techniques to record neural responses

of afferent nerve fibers exist, no techniques exist to observe the stress-state inside the finger or measure the pressure distributions on the surface of the finger. Finite element simulations provide a way to obtain both the stress-state inside the finger and the pressure distributions on the surface of the finger when an object is indented onto the finger. The results of these simulations can be used to (1) study the relationship between the surface pressure distributions and shape of the object that indents the finger (2) determine which of the tensorial stress-strain measures, or a combination of the measures (referred to as *relevant stimulus*) can be related to experimentally recorded neural responses and (3) construct neural responses from a population of mechanoreceptors and reduce the need for invasive neurophysiological experiments. Such studies would provide a link between macroscopic mechanistic phenomena and the molecular mechanisms of nerve-impulse generation (for example, stretch activated ionic channels). The study would aid in the development of tactile communication devices in rehabilitation, the development of tactile sensors for intelligent prostheses, and the development of human-machine interfaces for interaction with virtual environments and teleoperation systems.

1.3 Thesis Overview

This thesis describes a study of tactile sensing using a three dimensional finite element model of the primate fingertip. Various biomechanical and neurophysiological experiments are simulated using the model. A systems approach to tactile sensing and perception is also developed.

Chapter 2 provides background information on the anatomy of the human fingertip and summarizes previous work in human tactile sensing. The need for further biomechanical studies and the relevance to neurophysiological studies is discussed. A systems approach to tactile information processing is described.

Chapter 3 describes the development of a high resolution finite element model of the fingertip and its validation through comparison with empirical data.

Chapter 4 explains the biomechanical aspects of indentation of various shaped objects

on the fingerpad. The relationship between the surface pressure and the geometry of the contacting object is studied.

In chapter 5, the link between the stress/strain measures and experimentally recorded neural responses is investigated. Both chapters 4 and 5 are written so that they can be read more or less as independent papers.

Chapter 6 develops a systems approach to tactile sensing. The (spatial) impulse response functions for subsurface strain measures is obtained. A non-linear optimal signal estimation technique is used to achieve decoding of neural responses to infer surface pressure from the neural responses.

Chapter 7 summarizes the significance of the present work and discusses future research directions.

2 Background

2.1 Anatomy of the Human Fingertip

The human fingertip is a complex organ. The major structural components that make up the fingertip are the skin, subcutaneous tissues mostly composed of fat, bone and nail. Figure 2-1 (a) shows a cross-sectional view of a human fingertip. A typical human fingerpad is about 10 to 20 mm in diameter and the length of the distal phalanx (endmost bone) varies between 20 to 30 mm. The skin on the palmar side is thick compared to most parts of the body and is used for grasping as well as fulfilling sensory functions. The palmar skin is also characterized by the presence of finger prints. The following subsection contains a detailed anatomical description of the fingertip skin.

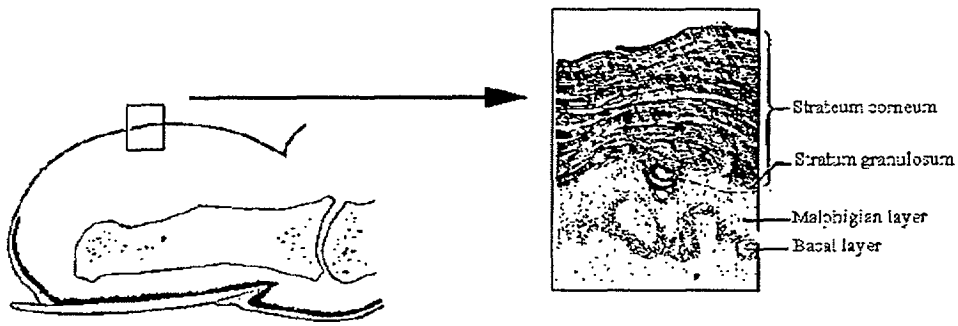

Figure 2-1: (a) Cross-section through a finger (adapted from O'Rahilly (1969)). (b) Different layers in the epidermis (adapted from Thomine (1981)).

2.1.1 Fingertip skin

The fingertip skin can be subdivided into an outer layer called epidermis, and an inner layer called dermis. The epidermis, in turn, is made up of five layers as shown in Figure 2-1 (b). The topmost layer is the *stratum corneum* which consists of dead keratinized cells with no detectable intercellular spaces. This layer is considered almost water-proof (Lockhart *et al.*, 1965). The next layer is the *stratum lucidum* which contains cells that have lost their nuclei and cell boundaries. It is typically present only in the palmar or plantar skin and is about two or three cells thick. The third layer is the *stratum granulosum* which contains granules produced during chemical changes occurring within cells as they progress to the topmost layer. This layer is also about two to three cells thick. The fourth layer is the *malphigian layer* which consists of a thick, multicellular layer of polygonal cells which get flatter as they approach the surface. This layer is the site of cellular multiplication and plays a significant part in skin regeneration. The bottom most layer is the *stratum basale*, which is separated from the bottom dermis by a fine acellular structure called the basement membrane. The stratum basale is attached to the basement membrane by means of protoplasmic prolongations known as hemidesmosomes. The dermis is attached to the basement membrane by collagen or retinacular fibrils, which thus indirectly fasten the dermis to the epidermis. The epidermis and dermis are separated by internal ridges called intermediate and limiting ridges.

The dermis consists of a superficial *papillary layer* and a deeper *reticular layer*, and is made up of collagen fibers, elastin fibers, blood vessels and nerve endings. The papillary layer is a close knit network of fibrous and elastic tissue. The reticular layer contains thicker collagen fibers than the papillary layer, and has numerous elastin fibers that run mostly parallel to the skin's surface.

The surface of the finger is characterized by the presence of ridges. The direction of these ridges reflect that of the underlying internal ridges. Also, most of the epidermal and dermal layers run parallel to these ridges. The spacing between the ridges is about 500 μm in the human fingertip.

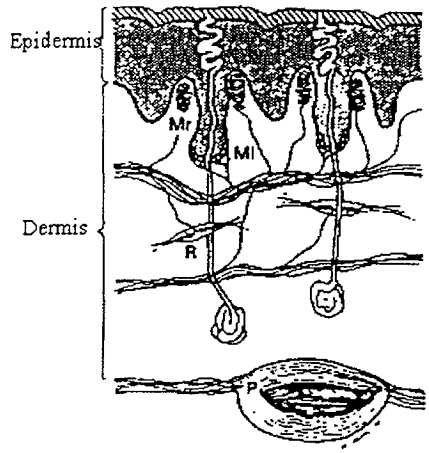

Figure 2-2: Cross-section through a fingertip skin showing the four mechanoreceptors (adapted from Johansson and Vallbo (1983)): Mr - Meissner's Corpuscles; MI - Merkel Discs; R - Ruffini Corpuscles and P - Pacinian Corpuscles. The figure is not drawn to scale.

2.1.2 Mechanoreceptors

The human fingertip skin is innervated by a variety of peripheral afferent nerve fibers. The receptors at the end of the nerves can be classified broadly as mechanoreceptors, thermal receptors and nociceptors (pain receptors). Among the mechanoreceptors in the human fingertip skin, four types have been identified and their locations are shown in Figure 2-2. These are the Meissner's Corpuscles, Merkel Discs, Ruffini Corpuscles and Pacinian Corpuscles. These four mechanoreceptors vary in their size, location and neural behavior. Table 2.1 summarizes some of the properties of these mechanoreceptors.

The nerve fibers innervating the mechanoreceptors have been classified primarily based on their adaptive properties in response to time-varying indentation on the most sensitive part of the fiber's receptive field. A "ramp and hold indentation" as shown in Figure 2-3 is applied to the finger and responses of the corresponding peripheral afferents are recorded. Two of the afferents respond only to the ramp (dynamic) phase of the stimulus and are referred to as the Rapidly Adapting (RA) and the Pacinian (PC) afferents. The other two afferents respond to both the ramp (dynamic) as well as the hold (static) phase of the stimulus and are referred to as the Slowly Adapting Type-I (SA-I) and Slowly Adapting

	Merkel	Ruffini	Meissner	Pacini
Location	Basal layer cells of the epithelial glandular ridges	Dermis	Dermal papillae protruding upward into the epidermis	Deeper layers of dermis, subcutaneous fat
Depth	0.7–1.0 mm	0.8-1.5 mm	0.5–0.7 mm	1.5 –2.0 mm
Size	10 μm	500 – 1000 μm long, 200 μm in central zone and 30-40 μm diameter near the poles	100 $\times$ 50 μm	long axis 0.3 – 1.5 mm, diameter 0.2 – 0.7 mm
Shape	Oval or rounded	Ellipsoidal	Ellipsoidal	Ovoid
Morphological Classification	Un-encapsulated, Epidermal	Encapsulated, Dermal	Encapsulated, Dermal	Encapsulated, Dermal
Structure	Groups of 5–10 cells at a site	4–5 layers of lamellar cells covered by a basement membrane	Each fiber has a irregular discoidal form oriented at right angles to the long axis of the corpuscle	Several layers of concentrically packed lamellar cells, subcapsular space filled with fluid
Sensitivity to Stimuli	displacement and velocity	displacement and velocity	velocity	velocity
Innervating Afferent Fiber	Slowly Adapting type I (SA-I)	Slowly Adapting type II (SA-II)	Rapidly Adapting (RA)	Pacinian (PC)

Table 2.1: Comparison of four mechanoreceptors found in the primate fingerpad. Adapted from Dandekar and Srinivasan (1995).

Type-II (SA-II) afferents. From Table 2.1 it can be seen that all the mechanoreceptors are located within the top 2 mm of the skin surface.

2.2 Previous Studies in Human Tactile Sensing

This section summarizes some of the salient works in the field of human tactile sensing. The work done in human tactile sensing can be categorized into three distinct areas:

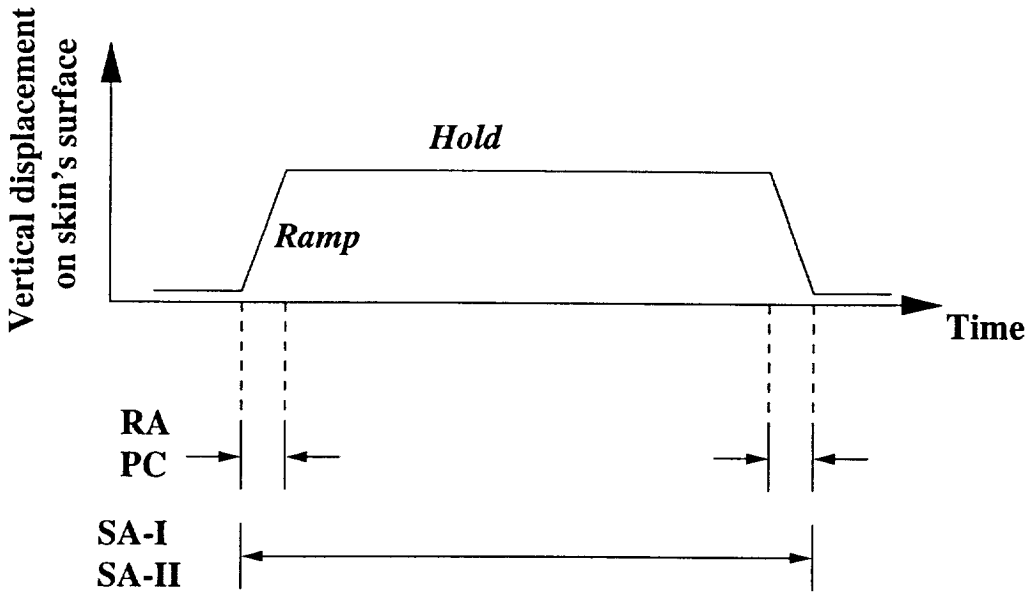

Figure 2-3: The four afferent nerve fibers innervating the mechanoreceptors are classified based on their response to time-varying stimuli such as the one shown. The RA and PC afferents respond only to dynamic stimuli while the SA-I and SA-II afferents respond to both dynamic as well as static stimuli.

neurophysiology, biomechanics, and psychophysics. Recent works have also included the systems approach, which combines both the biomechanical and neurophysiological approaches.

2.2.1 Neurophysiological studies

Neurophysiological studies in tactile sensing have involved applying a known object to the fingertip of a monkey or human, recording the peripheral neural responses, and analyzing the data to infer the neural behavior of the mechanoreceptors. These works include the study of neural behavior of the mechanoreceptors such as the mechanical-to-electrical transduction mechanism, size of receptive fields, sensitivity, threshold, and innervation density. Mountcastle and co-workers studied extensively the relation between neural response and perception (Mountcastle and Powell, 1959; Mountcastle *et al.*, 1972). Loewenstein and Skalak (1966) studied the mechanical-to-electrical transduction in the pacinian corpuscle. Knibestol and Vallbo (1970) established that there are at least four classes of cutaneous mechanoreceptors in the human fingertip. Knibestol (1973; 1975) studied the stimulus-response functions of slowly and rapidly adapting afferents and developed math-

ematical models for the discharge rate as functions of stimulus intensity. Johansson (1978), and Johansson and Vallbo (1979) studied the receptive field characteristics of the human mechanoreceptors and their innervation densities. These, and other works are well reviewed in Darian-Smith (1984), and Johansson and Vallbo (1983). Later studies have also focused on the relationship between the properties of the object contacting the fingertip such as its shape, compliance etc., and the responses of the afferent nerve fibers. Phillips and Johnson (1981; 1981a) indented monkey fingerpads with rectangular bar shapes and recorded the afferent neural responses. Srinivasan and LaMotte (1987) indented sinusoidal step shapes to monkey fingerpads and recorded the afferent neural responses under both static and dynamic conditions. These works led to hypothesis that the geometrical feature of the object that is encoded by the afferent responses is its curvature (LaMotte and Srinivasan, 1993). To summarize, neurophysiological studies utilized peripheral neural recordings to learn about the neurophysiological properties of the afferents, as well as the relationship between the responses and properties of the objects indenting the fingerpad.

2.2.2 Psychophysical studies

Psychophysics is concerned with the quantitative relationship between physical stimuli and the resulting behavioral responses of human subjects under carefully designed test conditions. Unlike neurophysiology, psychophysics adresses the overall behavior of the tactile system including the final subjective perception. Some specific earlier works in this area include the study of vibrotactile perception (Verillo *et al.* , 1969), roughness perception (Lederman and Taylor, 1972), spatial resolution (Loomis, 1979), and texture discrimination (Lamb, 1983) during touch. Though psychophysical studies were initially done independently, later they were often combined with neurophysiological studies in order to relate the peripheral neural responses to perception (Talbot *et al.* , 1968). A good review of earlier psychophysical and neurophysiological research in tactile sensing is presented in Loomis and Lederman (1986). Later efforts have involved tactile discrimination of curvature (Goodwin *et al.* , 1991), tactile discrimination of softness (Srinivasan and LaMotte, 1995) and tactile discrimination of thickness (John *et al.* , 1989; Ho and Srinivasan, 1996). Psychophysical evidence that four "channels" participate in perception was reviewed by Bolanowski *et. al.* (1988). These four channels are believed to have unique properties with regard to their frequency response, threshold, temperature dependence, etc. To summa-

rize, psychophysics utilized subjective human perception to study the overall mechanism of touch.

2.2.3 Biomechanical Studies

The biomechanical approach to tactile sensing focuses on the mechanical aspects of touch including determination of mechanical properties of skin and other fingertip tissues, mechanistic modeling of the fingerpad, computation of stress-strain measures in the vicinity of the mechanoreceptors, and a study of the relationship between these stress-strain measures and recorded peripheral neural responses. The study of mechanical properties of the skin in general also contributed to the effort in this direction. For example, the mechanical properties of the skin were found to be strongly dependent on species, age, sex, exposure and hydration (Tregear, 1966; Lanir, 1987), which implies that *in vitro* measurements of the mechanical properties of the skin could vary considerably. Skin has also been found to exhibit viscoelastic behavior and has rate-dependent stress-strain relations (Fung, 1981). Phillips and Johnson (1981b) in their study of relationship between subsurface strain measures and recorded neural impulses, modeled the finger as an infinite, isotropic, linear elastic, homogeneous medium, and found that maximum compressive strain measured at a depth of 0.75 mm was the best mechanical measure that could be linearly related to SA-I afferent responses. Srinivasan (1989) modeled the finger as an incompressible fluid enclosed by an elastic membrane and was able to predict the experimentally measured deformations on the surface of the finger. Gulati and Srinivasan (1996) indented human fingers with shaped objects, measured the temporal force responses and proposed a non-linear Kelvin type model to describe the overall mechanical behavior of the fingerpad. Dandekar and Srinivasan (1996) developed two dimensional and three dimensional finite element models of primate fingertips in order to relate subsurface strain measures to recorded neural responses of SA-I afferents. Maximum compressive strain and strain energy density were found to be the best candidates that could be linearly related to the responses of SA-I afferents. Recent work includes the development of pressure sensors to experimentally determine the surface pressure distributions during tactile contact (Pawluk, 1997), and modeling of fingertip pulp for ergonomic studies during tasks such as typing (Serina, 1997). To summarize, the biomechanical studies have aided the neurophysiological studies in relating the mechanical quantities such as stress and strain to recorded neural responses.

2.2.4 Systems Approach

The systems approach uses input-output relationships to model the behavior of the tactile system. A system is an abstraction of anything that takes an input, operates on it, and produces an output (Karu, 1995). A physical process can then be represented as a mathematical transformation between the input and the output. The use of systems approach has led to significant advances in other fields such as vision, telecommunications, radar etc. In the case of human tactile sensing, the surface force distributions form the input, as the entire information about the indenting object is available to the human in the form of surface loads within the region of contact. The corresponding neural responses can then be considered as the output. This approach, thus integrates both the biomechanical and neurophysiological approaches. The systems approach has two components: the *encoding problem* and the *decoding problem*. The encoding problem is the computation of neural responses based on the surface force distributions. This problem has been studied using plane strain assumption in Johnson and Phillips (1981b). The problem is also of interest to the robotics community and there have been several studies in this area (Fearing and Hollerbach, 1985; Speeter, 1992; Howe and Cutkosky, 1993). Decoding is the inverse problem of computation of surface pressure distributions based on the neural responses. This problem has been studied mostly by the robotics community (Rossi *et al.* , 1991; Pati *et al.* , 1988; Fearing and Hollerbach, 1985). The combined study of both encoding and decoding from both human and robot tactile sensing perspectives was presented in Karason *et. al.* (1998). To summarize, the systems approach uses overall input-output relationships to study tactile sensing.

2.3 Need for Further Studies

Currently, the most advanced model used for biomechanical studies on tactile coding of object shapes is the three dimensional finite element model developed by Dandekar and Srinivasan (1996). However, this model had limitations in that the size of the elements on the surface of the fingertip was not high enough to simulate indentation by steeply curved surfaces like the edges of bars. This means that the edge enhancement effects of SA-I responses cannot be effectively studied using that model. Higher resolution of the mesh on the surface will be useful not only in capturing steep curvatures, but will also useful in

preventing aliasing that could occur if enough sampling points are not used in the contact region. Higher resolution for the subsurface mesh will also be useful in predicting the response from a population of mechanoreceptors without aliasing. Thus a high resolution version of the existing model needs to be developed[1].

In the analysis by Dandekar and Srinivasan (1996), the relevant stimulus for SA-I afferents was evaluated based only on two dimensional models. The three dimensional model was used only to confirm the predictions of the 2-D models. A better approach would be to use the 3-D model itself to evaluate the relevant stimulus.

The systems approach simplifies the study of tactile sensing without having to resort to time-consuming finite element simulations, or experimental recordings. However the systems approach that have been used till now (Karason *et al.*, 1998) models the fingerpad as an infinite, flat, elastic space, which means the indentation by shapes cannot be fully studied. A better approach would be to take the curvature of the finger into account while using the systems approach, which can be done using the finite element model.

The inverse problem of decoding (i.e., obtaining surface pressure distributions from neural responses) has been studied only using linear systems approach. As will be shown in this work, a non-linear model is be needed to model the behavior of the static response of SA-I afferents. Hence non-linear signal estimation techniques are needed to decode surface pressure distribution (and consequently object's shape) from the distribution of neural responses.

2.4 Description of Object's Shape

In this thesis we study the indentation of objects that are rigid and are convex shaped. This section briefly describes the definition of shape as used in this thesis. In general, any geometrical attribute of the object can be used to quantify its shape. For example,

[1]Even though we study human tactile sensing, most of the neurophysiological recordings are done on monkeys. Thus the finite element model developed is that of monkeys and not of humans. In this thesis, we will use the term human tactile sensing to distinguish it from robot tactile sensing. The term actually refers to primate tactile sensing.

the coordinates of the points on the surface of the object with respect to some fixed axis, or the local slope of the object at each point on the object's surface as a function of the coordinates of the point can both be used to describe shape. However both these measures are not invariant with respect to translation or rotation of the object because they depend on the choice of the coordinate axes used. A better measure, which does not depend on the particular choice of coordinate axes, is the object's curvature. From differential geometry, it is known that the curvature distribution of an object's surface uniquely determines the form of the surface (Gauss, 1827). The curvature of the object has also been shown to be related to the responses of the mechanoreceptors in the finger (Srinivasan and LaMotte, 1991). In this thesis we consider the object's curvature to be an indicator of its shape.

3 Development of High Resolution Finite Element Model

This chapter describes the development of the high resolution 3D finite element model of the primate fingertip, and verification of the model through comparison of prediction of simulations with experimentally observed data.

3.1 Need for an Optimum High Resolution Model

In order to accurately model the contact of the fingerpad with objects [1] that have high curvatures such as the edges of bars, the deforming body should be able to conform to the steep curvature of the indenting rigid body. This is possible only if there are sufficient nodes on the deforming body in the contact region. In addition, a high mesh density at subsurface depths is needed to compute the subsurface strain measures without aliasing effects. Also higher resolution for the model improves the accuracy of the finite element simulation results. However, as the resolution of the model increases, the computational effort also increases. The 3-D model described in Dandekar and Srinivasan (1996) had about 8500 nodes and elements, and the size of the elements on the surface was about 500 μm. The model took about 30 minutes on the CRAY C90 supercomputer to solve each contact problem of indentation to a given depth by a cylinder. Further increase in the number of nodes will lead to even higher computational times. Thus it becomes necessary to optimize the resolution of the finite element mesh by using varying mesh densities throughout the model, with high mesh density only near the region of contact.

[1] Only rigid, convex objects are considered in this work.

3.2 Development of the Solid Model

The development of the model is divided into two steps: (1) development of the solid model and (2) development of the finite element model. A solid model is a model of the geometry of the object consisting of geometrical primitives such as curves (bounded by two points), surfaces (bounded by four curves) and solids (bounded by six surfaces). Curves, surfaces and solids are also referred to as lines, patches and hyperpatches respectively. A finite element model on the other hand contains elements and nodes, which are usually created after the solid model is defined. The advantage of separating the development of the solid model from that of the finite element model is that the same solid model can be used to generate different finite element models with different mesh densities. The development of the finite element model is not however totally independent of that of the solid model. For example, if the entire solid model is filled with only one solid, the resulting finite element model will not capture the geometry of the finger accurately, irrespective of the number of elements used. Also, generating a high resolution finite element model in general requires a solid model with high number of internal solids so as to ensure acceptable topology for the elements (aspect ratios close to 1, angles close to 90 degrees).

The first step in the development of the solid model is to obtain the geometry of the fingertip. Since the detailed internal geometry of the fingertip is not currently available, only the external geometry of the finger was used to develop the model. The internal geometry was idealized – it was assumed that the finger contains layers of tissues, with each layer being a homogeneous material. The process of obtaining the external geometry of the fingertip is described in detail in Dandekar and Srinivasan (1996). The external geometry of the finger was specified in the form of coordinates of points on the surface of the finger. For convenience, the finger was divided into 49 axial cross-sections, and at each cross-section, 72 points on the surface of the finger were specified.

To facilitate the generation of a model with varying mesh densities, the finger was divided into a number of sections in 3 orthogonal directions, radial (r), circumferential (θ) and axial (z) as shown in Figure 3-1 (a). It was decided to have 18 sections in the circumferential direction, 5 layers in the radial direction and 16 slices in the axial direction.

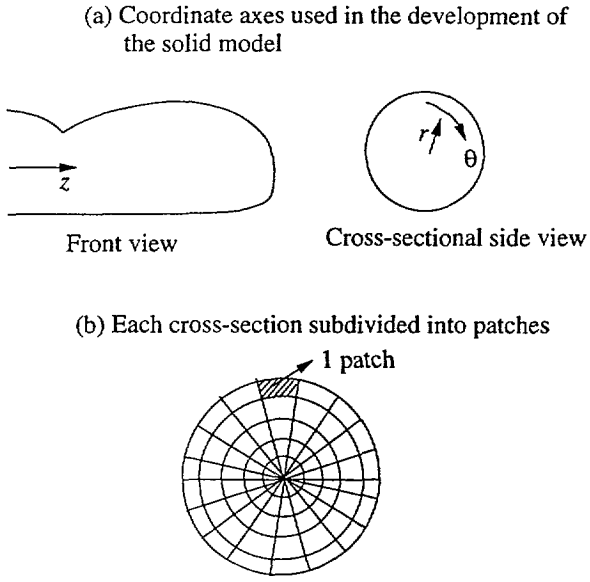

Figure 3-1: Development of the solid model

To begin with, the points specifying the boundary of each cross-section were joined together in a circular fashion and subdivided into a set of 18 curves (arcs). These curves were then scaled to obtain 4 more set of curves, which were concentric to the curves on the boundary, but had smaller radii. Thus, a total of 90 curves were created per cross-section. Patches were then created between pairs of curves to obtain 90 patches per section (Figure 3-1 (b)). The process was repeated for all the 49 cross-sections. Solids were then created by joining surfaces in four adjoining sections, so as to maintain C_2 continuity (continuity of curvature). Joining 4 contiguous axial cross-sections (patchwise) for all the 49 cross-sections results in 16 "slices", and a total of $16 \times 90 = 1440$ solids. Additionally, 3 more slices were created at the tip of the finger, as geometry data were not available at the tip. Thus the entire fingertip solid model contained $1440 + 3 \times 90 = 1710$ hexagonal solids.

All the above steps were done using the software PATRAN. The software also provides a convenient programming environment called Patran Command Language (PCL) which was used to automate the development process.

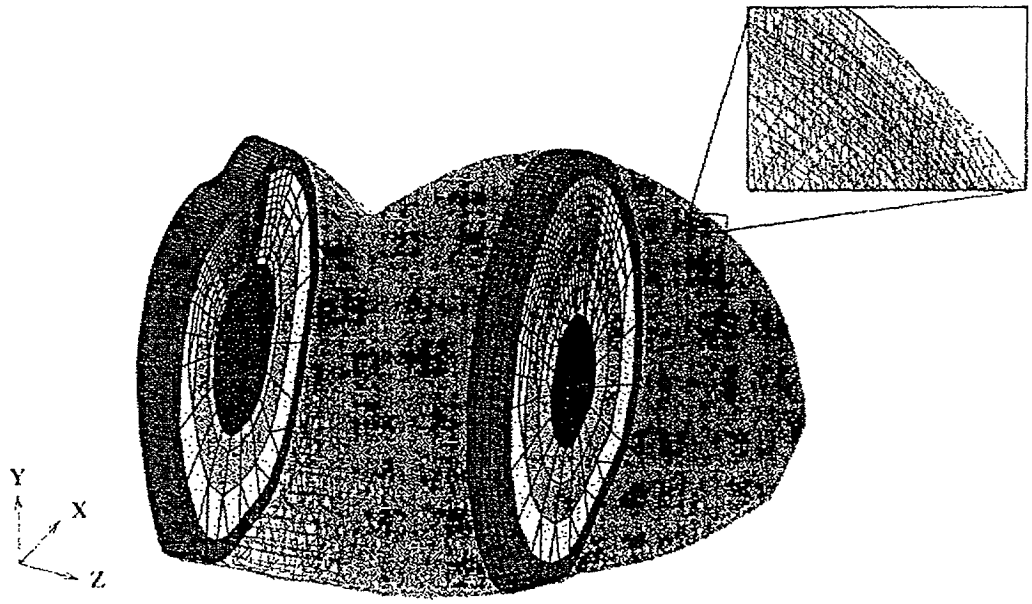

Figure 3-2: An optimal high resolution finite element model of the primate fingertip. The mesh resolution is high in the pulp region (element size is about 170 microns) where the finger would be in contact with objects and is lower in the bottom half portion of the finger. Also along the axis of the finger the mesh resolution is lower as we move toward the proximal end: The slice shown at the center has four elements in the axial direction whereas the slice at the proximal end has only one element in the axial direction. The inset shows that the region which appears to be fully shaded is actually composed of a mesh of elements and appears continuous because the mesh density is very high.

3.3 Development of the Finite Element Model

Having developed the solid model, the next step is to develop the finite element model, which is done by "filling" the solids with elements. The mesh density within a solid will depend on the number of elements chosen to fill that solid. In order to provide flexibility in varying the mesh density throughout the model, a general program was written in PCL. The program allows the user to choose the number of elements within each of the 90 solids in one axial slice. The same number of elements is followed throughout all the slices. However, from one slice to another, the number of elements in the axial direction can be varied so as to have fewer elements near the ends, where contact with objects are not likely to occur. This flexibility in choosing the mesh density makes it possible to choose high mesh density in the portion of the fingertip that would contact objects, and at the same

time limits the total number of elements for the model.

Figure 3-2 shows the finite element model that was developed. It can be seen that the mesh density is high only in the top pulp region and is very coarse in the nail region. The number of elements in the top half of the model is an order of magnitude greater than the number of elements in the bottom portion. All the elements in the model were either 8 noded isoparametric elements or 6 noded wedge elements. The entire model had about 30,000 nodes and 30,000 elements. The size of the elements in the top surface region was at most 170 μm.

The model developed here can be compared to the earlier model developed by Dandekar and Srinivasan (1996). The earlier model had 8500 nodes and elements and had a resolution of 500 μm on the top surface of the finger. By comparison, the current model has three times the resolution, and three times the number of nodes. Had a simpler task of subdividing the previous model been taken, the new model would have had $3^3 = 27$ times the number of nodes of the previous model. However the current model has only a three fold increase in the number of nodes. Thus the *increase in the number of nodes* has been reduced by almost an order of magnitude. For 3D problems, the computational time goes at least as the square of the number of nodes. Thus the computational time for the analysis using the current model has been *reduced by about two orders of magnitude* compared to the model that would have resulted by a simple subdivision of elements.

To complete the model development, material properties and boundary conditions have to be specified. At present no consistent material properties of fingertip tissues *in vivo* is available. The published data on material properties varies considerably. The best data consistent with *in vivo* biomechanical experiments is presented in Dandekar and Srinivasan (1996) and the same properties are used in the present model. The layers in the finger correspond to different tissues inside the finger. The outermost layer represents the epidermis, the second layer represents the dermis, the next two layers represent layers of fat, and the innermost layer represents the bone. All the layers were assumed to be linear elastic and isotropic. The ratio of the Young's Moduli of the five layers were chosen to be $10^4 : 10^3 : 10^3 : 10^3 : 10^8$ (Dandekar and Srinivasan, 1996), based on matches between

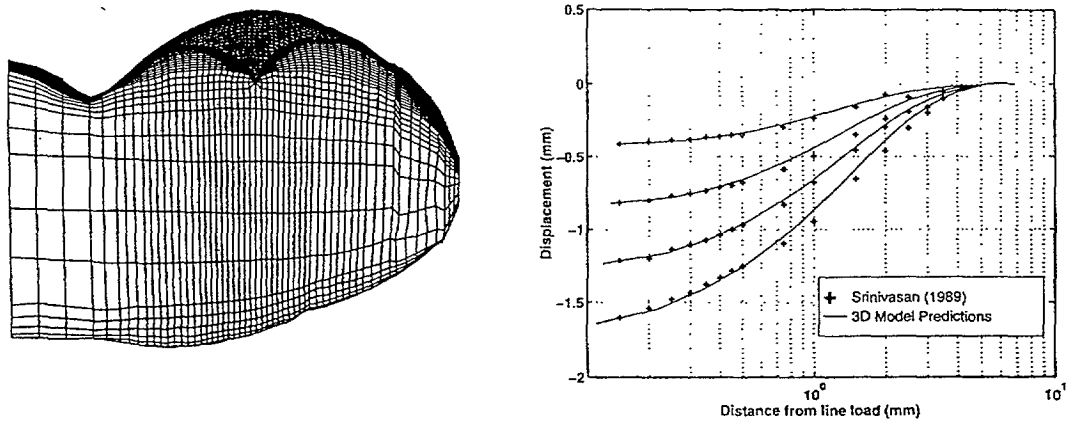

Figure 3-3: Line load indentation of the monkey fingertip. The line load was indented into the monkey finger model to a depth of indentation (DOI) of 2 mm. The figure on the left shows the deformed model superimposed over the undeformed model. The vertical displacements of the nodes in the deformation region of the finger in this side profile are compared with the experimental results from Srinivasan (1989) in the figure on the right. The four plots correspond to DOIs of 0.5, 1.0, 1.5 and 2.0 mm. For all the DOIs, the model predictions match the empirical data very well, thus validating the model.

model predictions and experimental data on fingertip surface deflection under a line load. The Poisson's ratio of all the layers was taken to be 0.48 (nearly incompressible). The boundary conditions consisted of fixed boundary conditions at all the nodes corresponding to the finger nail and also all the nodes at the proximal edge of the fingertip. Since the material properties were obtained by matching simulations under small displacement formulations (Dandekar and Srinivasan, 1996) with experimental data, small displacement formulations were used for all the simulations described in this work.

3.4 Verification of the Model

This section describes biomechanical validation of the finite element model with experimental data. The experimental data for comparison is taken from Srinivasan (1989) in which monkey fingertips were indented with a thin bar positioned perpendicular to the axis of the finger. Vertical displacements were obtained as a function of the distance from the location of the load for a number of points lying perpendicular to the load. The same

experiment was simulated on the finite element model. The thin bar was modeled as a 'line load' and all the nodes under the load were moved down vertically. Figure 3-3 shows the deformed mesh superimposed on the original mesh, and a comparison between the experimental predictions (Srinivasan, 1989) and the model predictions. It can be seen that the model predictions match very well with the experimental data, thus validating the model.

4 Mechanical Signals in Tactile Sensing

4.1 Motivation

During manual exploration and manipulation, the mechanics of contact between the skin and the contacting object plays an important role in determining the response of mechanoreceptors embedded in the skin, and consequently, in tactile perception. In these tasks, primates predominantly use their fingerpads owing to the fine spatial resolution due to the high density of mechanoreceptors and also the high degree of dexterity due to fine motor control that can be achieved. It has been hypothesized that the response of each mechanoreceptor is determined by the stresses and strains at its immediate neighborhood. The collection of the stresses and strains at all mechanoreceptor locations represent spatial sampling of the mechanical state in the fingertip. This mechanical state is determined by the mechanics of object-skin interactions, which are governed by: (1) the geometric (e.g. shape) and material properties (e.g., compliance) of the object (2) the geometric and material properties of the finger, and (3) the contact conditions such as the average depth of indentation, or, equivalently, the net contact force. The mechanoreceptors then transduce the stresses, strains or a combination (hereafter referred to as the mechanical state) in their vicinity into neural impulses, which convey information about the object properties and contact conditions through the SA-I, SA-II, RA and PC afferents to the central nervous system (CNS). It is evident that to study the process of information coding during touch, one has to know the mechanical state in the fingertip when the finger contacts an object.

No experimental techniques exist to directly observe the mechanical state within the fingertip in contact with an object. To overcome this difficulty Johnson and Phillips (1981b)

developed an analytical mechanistic model of the fingertip to numerically compute the distribution of the stresses and strains. They assumed the fingertip to be mechanically equivalent to a flat and homogeneous elastic medium of infinite extent and were able to predict well the responses of SA-Is to static indentations of rectangular gratings. However, because this model does not take into account either the geometry of the fingertip, or the inhomogeneous composition of tissues within the fingertip, it is unable to model well the contact interactions with arbitrarily shaped objects. For example, in touching a planar surface that is large relative to the size of the finger, the actual contact region would occupy a small portion of the object surface, whereas the semi-infinite model would predict that the entire surface of the object would be in contact. Therefore, finite element models of primate fingertips that capture the external geometry and the tissue layers within the fingertip were developed. Srinivasan and Dandekar (1996) developed 2-D finite element models of the primate fingertip. These models were able to predict the static responses of SA-I receptors only along a cross-section. Subsequently three dimensional finite element models that predicted well the deformations on the surface of the finger (Dandekar and Srinivasan, 1996) were developed. This chapter describes the use of a high resolution 3D finite element model for the investigation of the mechanistic bases underlying tactile sense during static contact with rigid and frictionless objects.

From the principles of contact mechanics, it is clear that the entire information about the shape, orientation, and the amount of indentation of a frictionless rigid object indenting the fingertip is uniquely contained in the surface pressure distribution within the region of contact. Pressure on the skin surface is non-zero only within the region of contact. Tactile mechanoreceptors can gather information about the object that contacted the finger only by tracking the loads on the skin within the region of contact. For example, when our finger touches a knife-edge, the surface pressure is present only in the narrow region of the skin that contacts the edge. In contrast, if we touch a flat plate with the same force of indentation, the surface pressure will be spread over a wider region and will have a lower magnitude. Therefore, the mere extent of surface pressure distribution conveys some information about the shape of the object that is in contact with the finger. In addition, the spatial variations in pressure intensity within a contact region give more detailed information about object shape. From a systems point of view, the surface pressure distribution can

therefore be considered as the "input" to the tactile system. The corresponding responses of the population of mechanoreceptors can be considered as the "output" of the tactile system.

Using a Cray C90 supercomputer the static indentation of various objects on the fingertip is simulated. All the objects are assumed to be rigid and frictionless. Rectangular bars (Phillips and Johnson, 1981b), circular cylinders (Srinivasan and LaMotte, 1991) and sinusoidal step shapes (Srinivasan and LaMotte, 1987) are indentors for which SA-I responses have previously been recorded. The same objects and indentation depths were simulated to obtain the surface pressure distribution in the region of contact.

4.2 Methods

4.2.1 Three dimensional finite element models

The 3D finite element model of the primate fingertip that is used was described in Chapter 3 and is summarized here for convenience. The model has four layers with different elastic moduli governing the stiffnesses corresponding to the epidermis, dermis, adipose tissue and bone. In order to study the mechanics of contact between the finger and steeply curved objects such as the edges of bars, the model must have sufficient spatial resolution, and consequently a large number of nodes in the contact region. However, increasing the number of nodes arbitrarily will lead to very high computational times even with a supercomputer. Hence an optimal high resolution model of the monkey fingertip that has a large number of nodes in the pulp region of the finger where contact occurs and less number of nodes in other locations, was developed. The size of the elements in the contact region is about 170 microns. The model has about 30,000 nodes and elements, corresponding to about 90,000 degrees of freedom. Such a high number of degrees of freedom necessitated the use of the Cray C90 supercomputer. All the simulations to study the pressure distributions on the surface of the finger were done using this high resolution model of the monkey fingertip.

4.2.2 Simulations

Simulation of static contact between the finger and an object can be done under two modes – prescribed depth of indentation (DOI) or prescribed force of indentation. When the

object is indented up to a prescribed DOI, the area of contact and the force required to indent the object are not known a priori. Therefore, only when an object is smaller than the fingertip, has sharp boundaries, and is indented to sufficient DOI that the edges are in complete contact with the finger, the contact region is known. Except for this special case, the contact region (defined as the region having non-zero pressure) is governed by the deformation of the fingertip, which, in turn, depends on the pressure distribution within the contact region whose extent is unknown. Therefore, simulations involving contact interactions are generally nonlinear, and need to be done iteratively i.e. the indentation is done in increments. More details can be found in Chapter 5 in Abaqus/Standard User's Manual (1995). The case of prescribed force of indentation is similar except that the object is now moved toward the finger until the necessary force gets reflected onto the object. In our models however, the amount of force, usually specified in gram weights or Newtons is only in pseudo units. This is because the exact values of Young's Modulus (a measure of stiffness) of the tissues are not known under *in vivo* conditions. This problem can be easily overcome by converting the prescribed force of indentation into one with prescribed DOI, as long as the equivalent DOI is known from the actual biomechanical experiments. (For a given pair of contacting surfaces of elastic objects and a given prescribed force of indentation there is only one DOI). Thus, in our simulations whenever we needed to indent up to a prescribed force of indentation, we first indent the object up to the corresponding DOI and then use the force that was reflected back to perform other simulations that might need the same force of indentation.

In the case of indentation by sinusoidal step shapes (referred to simply as "steps"), the steps were indented at different lateral locations (along the x axis - see Figure 3-2 for axis conventions used in this work) with respect to the finger. The location of the step is taken to be the location of a reference point on the step and is indicated in the figures using a + mark. The lateral distance is measured from the center of the fingertip surface, which is taken to be the origin ($x = 0$).

Although the model is of high spatial resolution, since the surface of the finger model is actually polyhedral due to the finite number of nodes, artifacts will be introduced in the surface pressure distributions wherever the surface of the finger has local bumps. The

artifacts will manifest as spurious peaks. Median filtering (Gonzalez and Wintz, 1987) is a commonly used technique to eliminate such artifacts and has been used extensively in digital image processing techniques to enhance visual images. In our calculations, a 4x1 median filter was used to eliminate spurious peaks in the surface pressure distributions. Matlab software package was used for this purpose.

Each of the prescribed depth of indentation simulations for the rectangular bar indentors took about 2 hours and 40 minutes on the CRAY C90 supercomputer to be solved. The prescribed force of indentation problems for the sinusoidal indentors took about 3 hours and thirty minutes to be solved. The computations averaged about 700 MFLOPS.

4.3 Results

4.3.1 Surface pressure distributions caused by rectangular bars

Rectangular bars have a shape that has constant zero curvature in the flat portion and infinite curvature at the edges. Two bars of 3 mm and 1.5 mm widths were used to study the pressure distributions that are produced on the surface of the fingertip when in contact with rectangular bars.

Rectangular bar – 3 mm wide

This section describes the features of surface pressure distribution when the monkey fingertip model is indented by a 3 mm wide rectangular bar that is much longer than the fingertip. The axis of the bar is parallel to the axis of the finger and is placed at the center of the fingertip surface (x=0). The bar is placed such that the flat portion is parallel to the top portion of the finger. The bar is indented up to a maximum DOI (measured with respect to the topmost point on the finger) of 1.33 mm. Figure 4-1 shows the deformed finger and the surface pressure distribution for DOI equal to 0.33, 0.67, 1.0 and 1.33 mm. When the DOI is 0.33 mm, neither of the edges of the bar contact the finger. The area of contact, which is the portion of the finger that actually touches the bar, is small. The surface pressure is maximum at the point of the finger that got indented the most and decreases as we move away from that point along both the lateral (x) and axial (z) directions. When the DOI is 0.67 mm, the left edge of the bar comes in contact with the finger, but not the right edge,

because of the asymmetry of the finger. The contact area has increased in both the lateral and axial directions. Along the lateral direction, the surface pressure remains flat for most of the contact region, except under the left edge of the bar where the pressure begins to show a peak. When the DOI is increased to 1.0 mm, the left edge of the bar fully contacts the finger whereas the right edge indents the finger only slightly. The width of contact in the lateral direction begins to saturate at 3 mm but continues to increase in the axial direction. The surface pressure along the lateral direction shows a higher peak under the left edge and a lower peak under the right edge, but is approximately flat in between the two edges. When the DOI is 1.33 mm, both edges fully contact the finger. The extent of contact in the lateral direction does not increase beyond 3 mm, but continues to increase in the axial direction because the bar is longer than the finger along the finger axis. The surface pressure under both the edges show sharp peaks compared to the other regions where the pressure is more or less flat. For all the DOI, along the axial direction of the finger the pressure attains higher values near the center of the contact region and decreases smoothly away from the center.

Rectangular bar - 1.5 mm wide

When the width of the rectangular bar is reduced from 3 mm to 1.5 mm, the general features of the pressure distribution remain approximately the same, but specific events such as contact by the left edge or by both edges, happen at a lesser DOI. Figure 4-2 shows the monkey finger model indented by a 1.5 mm wide rectangular bar for DOI of 0.33 and 0.67 mm. When the DOI is 0.33 mm, the left edge of the bar just touches the finger while the right edge does not touch the finger. The situation is similar to that of the 3 mm bar at a DOI between 0.33 mm and 0.67 mm. The surface pressure starts to show a slight peak only under the left edge. When DOI is 0.67 mm for the 1.5 mm bar, both the edges fully contact the finger and the situation is similar to that of the 3 mm bar at a DOI = 1.33 mm: the surface pressure shows two sharp peaks corresponding to the two edges of the bar. In this case the width of contact in the lateral direction does not increase beyond 1.5 mm, which is the width of the bar.

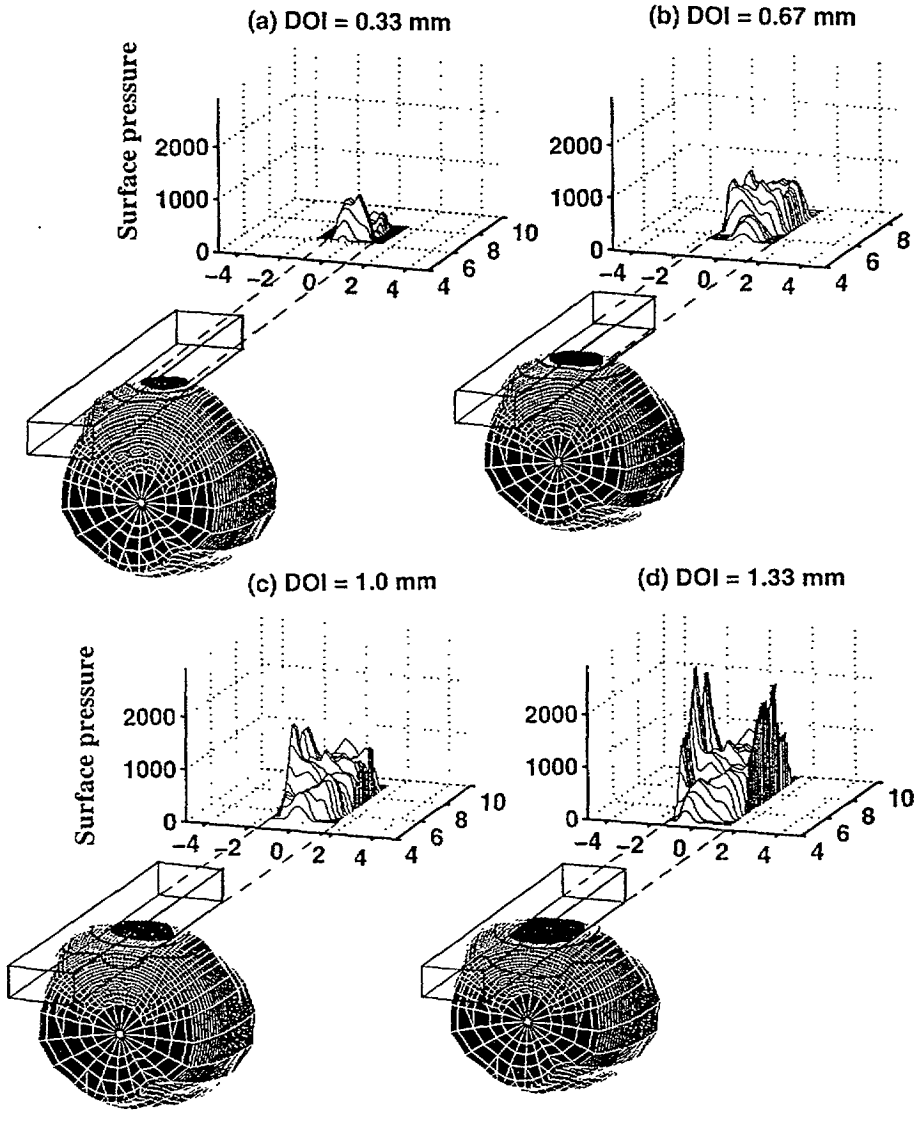

Figure 4-1: Monkey fingertip indented by a rectangular bar of width 3.0 mm. The bar was placed at the center of the finger and indented onto the fingerpad. Only a portion of the finger is shown. The region of contact for DOI = 0.33, 0.67, 1.0 and 1.33 mm is shown by the dark shaded region at the top of the fingertip surface. It can be seen that the extent of contact increases with increasing DOI, but saturates along the lateral direction at a width equal to the width of the bar. Additionally, two contours of constant vertical displacements are shown on the finger. The corresponding pressure distributions on the skin surface are plotted. Panels (c) and (d) indicate that the surface pressure forms a peak when the edges of the bars come into contact. The surface pressure has dimensions of force/area in pseudo units. Pressure in Pascals can be calculated by multiplying the values shown by E/10,000 where E is the Young's Modulus (in Pascals) of the top layer of the skin.

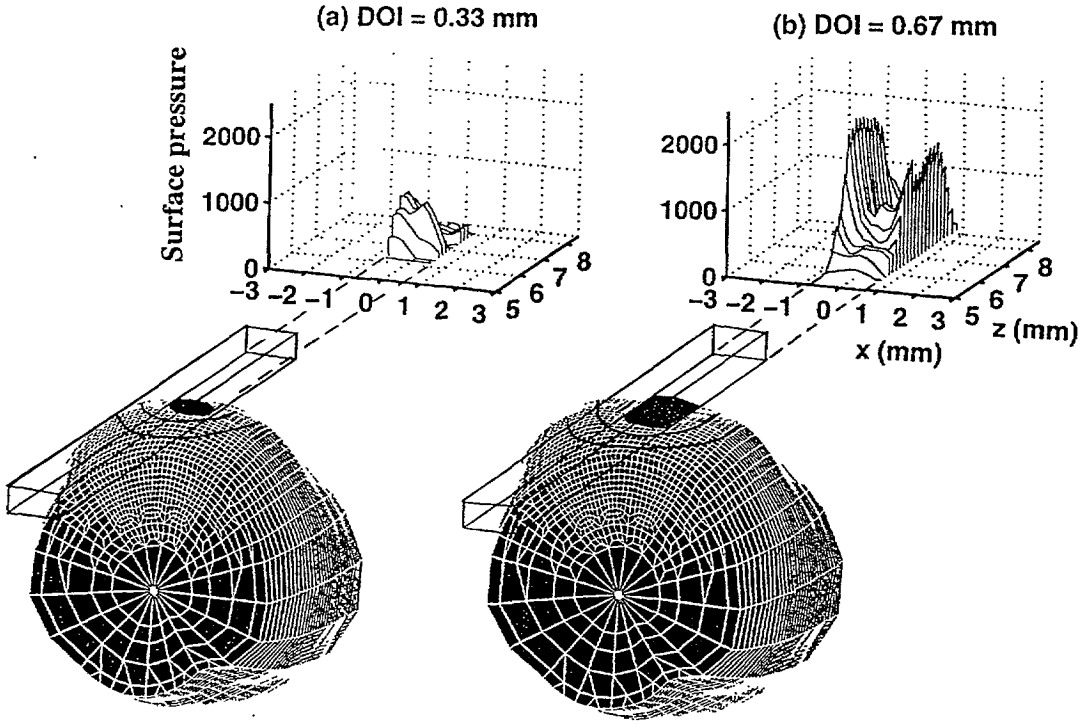

Figure 4-2: Monkey fingerpad indented by a rectangular bar of width 1.5 mm. The pressure distributions on the skin surface for DOI = 0.33 and 0.67 mm are shown. The extent of contact is shown on the finger by the shaded region on the fingertip surface. When DOI = 0.33 mm, the left edge just touches the finger and causes pressure peaks to arise. When DOI = 0.67 mm both the edges fully contact the finger and the surface pressure has two sharp peaks at the locations where the edges contact the finger.

4.3.2 Surface pressure distributions caused by cylindrical shapes

A cylinder is an object whose shape is characterized by zero surface curvature along its axis and a constant curvature (equal to the reciprocal of the radius) perpendicular to it. Two cylinders, one with a diameter of 3 mm (small cylinder) and another with a diameter of 9 mm (large cylinder) were used to study the pressure distributions that are produced when finger pad comes in contact with cylindrical objects. The 3 mm diameter cylinder has a high curvature, 3 times that of the 9 mm diameter cylinder. As in the case of rectangular bars, the axes of the cylinders are placed parallel to the finger axis during indentations.

Figure 4-3 shows the surface pressure distributions due to cylindrical indentors. At a DOI of 0.33 mm, the surface pressure distribution for both the cylinders is of the same

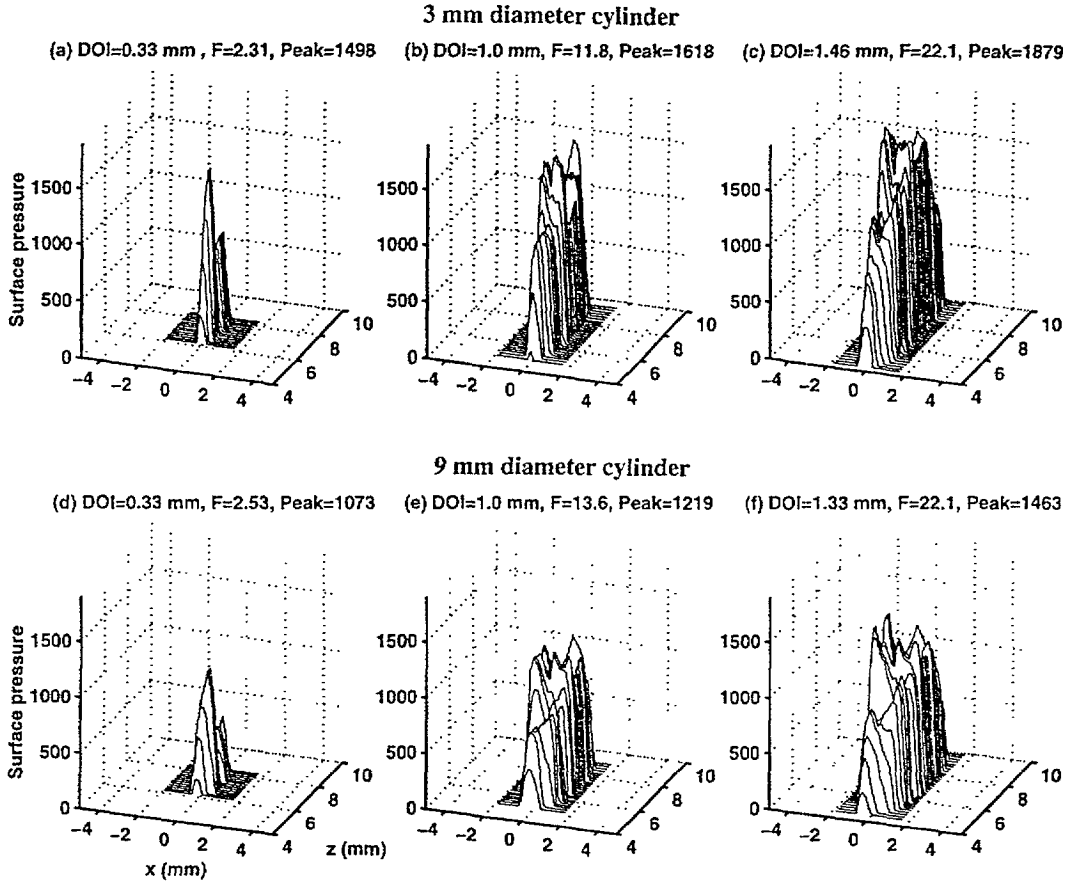

Figure 4-3: Monkey fingertip indented by cylindrical indentors. The top panels show the surface pressure distributions when a cylinder of diameter 3 mm is indented into the fingertip. In each panel, the DOI, force required for that indentation (F, expressed in gwt) and the peak pressure (Peak) are shown on top. The bottom panels show the pressure distributions for the case of indentation by a 9 mm diameter cylinder. The left and middle sets of panels show results for prescribed DOIs of 0.33 mm and 1.0 mm respectively. The right set of panels is for a prescribed force of indentation, equal to that required to indent the 9 mm diameter cylinder to a DOI of 1.33 mm. For a given DOI or force, the 3 mm diameter cylinder shows higher peak pressures and lower contact widths compared to those caused by the 9 mm diameter cylinder. At any locus, non-zero pressure indicates that the point is inside the contact region between the cylinder and the fingertip.

general shape, except that for the smaller cylinder, the peak magnitude is higher and the area of contact is smaller. The total force required to indent the bigger cylinder was actually about 10% higher (the total force can be obtained by integrating the surface pressure over the area of contact). At a DOI of 1.0 mm, the surface pressure distribution for both the cylinders shows a more flat response. The characteristic peaks that were present under the edges of rectangular bars are absent. For the same DOI, the surface pressure is higher and the width of contact is smaller for the smaller cylinder, as in the case of the rectangular bars. The total force required to indent the bigger cylinder was about 15% higher. Since the difference in pressure is partly due to the different forces required to indent the two indentors, in one simulation we fixed the force of indentation to be constant and the results are shown in the right panel. It is seen that the surface pressure is about 30% higher for the smaller cylinder compared to the larger cylinder.

4.3.3 Surface pressure distributions caused by sinusoidal step shapes

Srinivasan and LaMotte (1987) indented monkey fingertips with sinusoidal step shapes and recorded the neurophysiological response of cutaneous mechanoreceptors. The same experiment was simulated using the monkey fingertip model. The geometry of the steps is discussed in detail in Srinivasan and LaMotte (1987). The step has a bottom flat portion, then a convex curved portion, followed by a concave curved portion, and then a top flat portion that is 0.5 mm higher than the bottom. The flat portions of the step have zero curvature whereas the convex portion has a positive curvature and the concave portion of the step has a negative curvature. In the simulations, the step is indented onto the finger up to a force of about 2.33 gwt [1] and the indentation is repeated after moving the step laterally to subsequent locations in a direction perpendicular to the axis of the finger.

Step 1 - Steep Step

This section describes the results for step 1, which has a half-wavelength of 0.450 mm and is considered to be a steep step. Figure 4-4 shows the surface pressure distributions and the extent of contact in the lateral direction for six different locations of the step as it is indented onto the finger pad with same forces at all locations. When the step is at x=2 mm

[1] In the experiments by Srinivasan and LaMotte (1987) the force of indentation was 8 gwt. See Section 5.3 for comments on the differences due to the two forces.

(i.e., the sharpest point of the step, is 2 mm to the right of the center of the finger pad), only the bottom flat part of the step contacts the finger (Figure 4-4 (a)). The pressure distribution is diffuse and is spread over a region. As the step is lifted up, moved from right to left above the finger, and then indented onto the finger, the convex portion of the step comes into contact with the finger in addition to the flat bottom part (Figures 4-4 (b) and (c)). In Figure 4-4 (b), the surface pressure shows a flat portion to the left and a small peak to the right corresponding to the convex portion. In Figure 4-4 (c) , the surface pressure is dominated mostly by the peak under the convex portion. In Figure 4-4 (d) only the steep convex portion contacts the finger. The surface pressure peak has increased and the contact area has decreased. From Figures 4-4 (b) through (d) it can be seen that the surface pressure under the steep convex portion of the step progressively increases in magnitude, while the area of contact decreases. With further movement of the step to the left, both the convex portion and the top flat portion of the step come into contact with the finger(Figure 4-4 (e)). The pressure distribution has two disconnected regions: a high peak on the left under the convex portion of the step and much lower values under the top flat portion of the step. The pressure distribution is spatially separated into two regions because the concave portion of the step does not come into contact with the finger. With further movement of the step to the left, the convex portion barely touches the finger and the top flat portion contacts the finger more, as seen in Figure 4-4 (f). The left peak has decreased in magnitude and the right peak has increased to the extent that both the peaks are comparable. When the step is moved even further to the left, the top flat portion would contact the finger completely and the loading on the finger is identical to that of the contact by the bottom flat portion of the step. Therefore the pressure distribution will be identical to that of Figure 4-4 (a). It can also be seen that the concave portion of the step does not contact the finger at any time. In summary, as the steep step is moved from right to left starting from the bottom flat portion of the step contacting the finger, the pressure distribution is initially diffuse, then increases to a peak, then a second (discontinuous) portion starts to appear on the right, then the left peak decreases in magnitude and vanishes, and finally the pressure distribution assumes the original shape we started with. Comparing Figures 4-4 (a) through (f), the maximum pressure is seen to be inversely related to the area of contact between the step and the finger. In all the figures the peak pressure occurs at the point where the sharpest point of the step touches the finger.

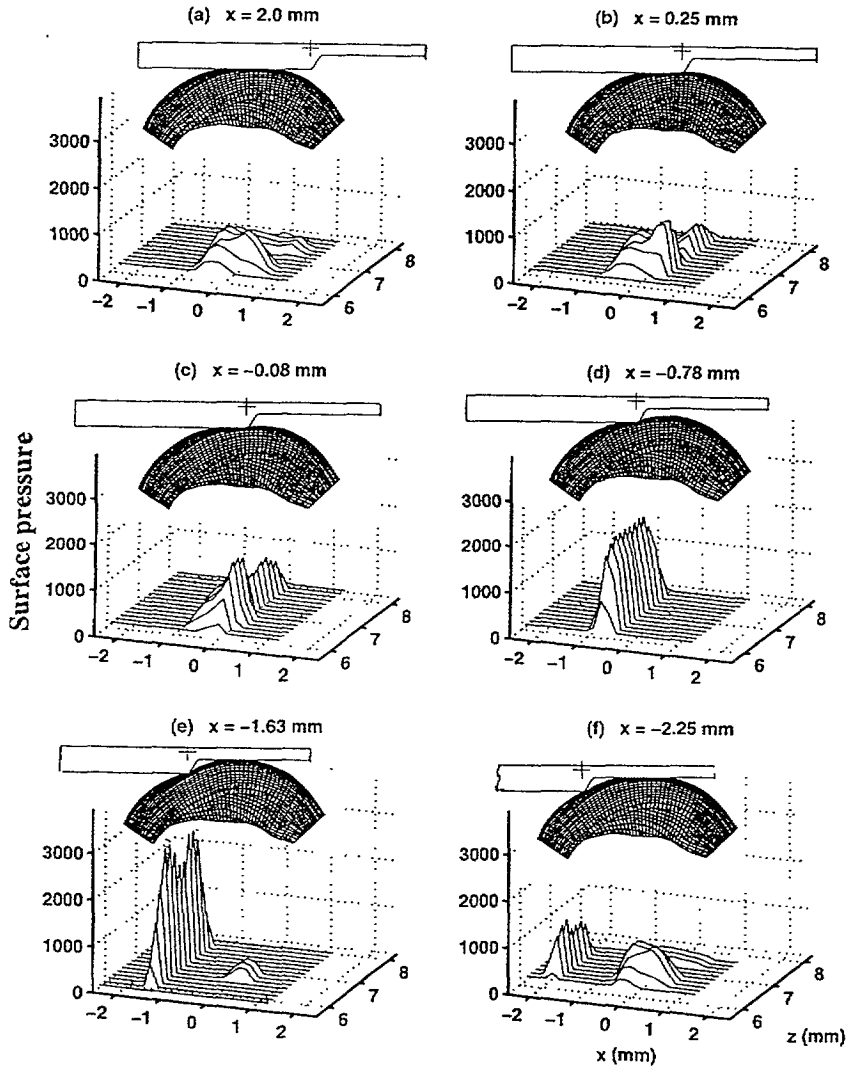

Figure 4-4: Monkey fingertip indented by the steep sinusoidal step (step 1). The step was indented into the finger up to a prescribed force of indentation. The pressure distribution on the skin surface and the extent of contact region in the lateral direction is shown for six cases - for each case the step was located at a different position with respect to the finger. The location of the step is the location of the reference point shown on the step by a + mark and is indicated above each of the figures (note: x=0 corresponds to the center of the finger pad surface). The plots show the corresponding surface pressure distributions. In panels (a) through (d), there is only one contact region. In panels (e) and (f) there are two contact regions. In panels (b) through (f) the surface pressure shows a peak at the location directly under the most curved convex part of the step (denoted by the + mark). For all the figures, the scale used in plotting the surface pressure is only approximately the same as the scale used to show the contact between cross-sections of the finger and the step.

Step 5 - Gradual Step

The gradual step is also sinusoidal and hence is similar in shape to the steep step, except that the curvature of the curved portion is lower than that of the steep step. The half-wavelength of the gradual step is 3.134 mm, making the curved portion of the step to be much wider than that of the steep step.

Figure 4-5 shows the extent of contact and surface pressure distribution for six locations of the step. Since the step has a wider curved portion, the locations of the step spanned a wider region compared to that of the steep step. When the step is at x = 2 mm (Figure 4-5(a)), only the bottom flat portion contacts the finger. The contact mechanics is identical to that of the steep step at x = 2 mm (see Figure 4-4 (a)). In Figure 4-5 (b) the convex portion of the step comes into contact with the finger, in addition to the bottom flat portion. The surface pressure shows a peak under the convex portion and a flat portion under the flat part of the step. In Figure 4-5 (c) only the convex portion of the step touches the finger. The pressure distribution has some peaks, but is more diffuse than in Figure 4-4 (d) for step 1. In Figure 4-5 (d) both the convex and the some of the concave portions of the step touch the finger. The pressure distribution is diffuse with a reduction in its magnitude owing to an increase in contact area, and shows a downward slope to the right where the concave portion contacted the finger. In Figure 4-5 (e), the convex, concave and the top flat parts of the step contact the finger. The surface pressure shows a left peak corresponding to the convex portion of the step and a right peak corresponding to the flat portion of the step. In between the two peaks the pressure shows a drop, corresponding to the concave portion of the step. The pressure magnitudes are much lower than before and the contact area is high. In Figure 4-5 (f), the concave part of the step and the top flat part of the step touch the finger. The surface pressure shows a peak under the flat portion and a drop in its magnitude under the concave portion of the step. When the step is moved to the left further, the finger would be fully in contact with the top flat portion of the step and the pressure distribution will be identical to Figure 4-5 (a), in the case of the steep step (Figure 4-4 (a)).

Comparing Figures 4-4 and 4-5 it can be seen that unlike in the case of the steep step, the area of contact for the gradual step does not become disconnected. The peak pressures

in the case of the steep step is higher than the peak pressures in the case of the gradual step, but the area of contact is lower for the steep step. For example, for the same force, the highest pressure for the steep step is about 2000 (which occurs near x = -1.63 mm) whereas the highest pressure for the gradual step is less than 1000.

4.3.4 Subsurface strain measures

In the fingertip, the merkel cells that innervate the SA-I afferents are known to be located at approximately 0.75 mm below the skin surface (Phillips and Johnson, 1981b). Since the mechanical state influences the neural response rates of the SA-I afferents, in this section we discuss the mechanical state at a depth of 0.75 mm.

Indentation by step 1

Figure 4-6 shows a plot of two strain measures, strain energy density (energy of deformation in a unit volume element) and axial stress (normal stress component along the finger axis i.e. along z direction in units of force per unit area) at a depth of 0.75 mm for two different DOIs. The step is located at x=-1.63 mm. While strain energy density is a scalar, does not have an orientation and is always a positive quantity, axial stress is one of the components of the stress tensor, acts in a specific direction along the axis of the finger and could be either compressive or tensile. From Figure 4-6, three points are evident. First, the shape of the strain energy density distribution is very different for the two DOIs. At the smaller DOI, the distribution shows only a single peak, whereas at the higher DOI two separate peaks are seen. Second, in the case of axial stress, even though the distribution is similar to the strain energy density distribution at the lower DOI, the distribution is quite different at a higher DOI in that two separate peaks are not seen. Third, even though the surface pressure had two disconnected regions in the case of lower DOI (Figure 4-4 (e)), the strain energy density and axial stress have no separate disconnected regions – this indicates that the mechanical state at a depth of 0.75 mm is a low pass filtered version of the pressure on the surface of the finger. At higher DOIs, the filtering is not severe enough to blur the strain energy density distribution, but is strong enough to blur the axial stress distribution. An implication is that a mechanoreceptor population triggered by strain energy density as relevant stimulus will have a better spatial resolution than that triggered by axial stress as the relevant stimulus.

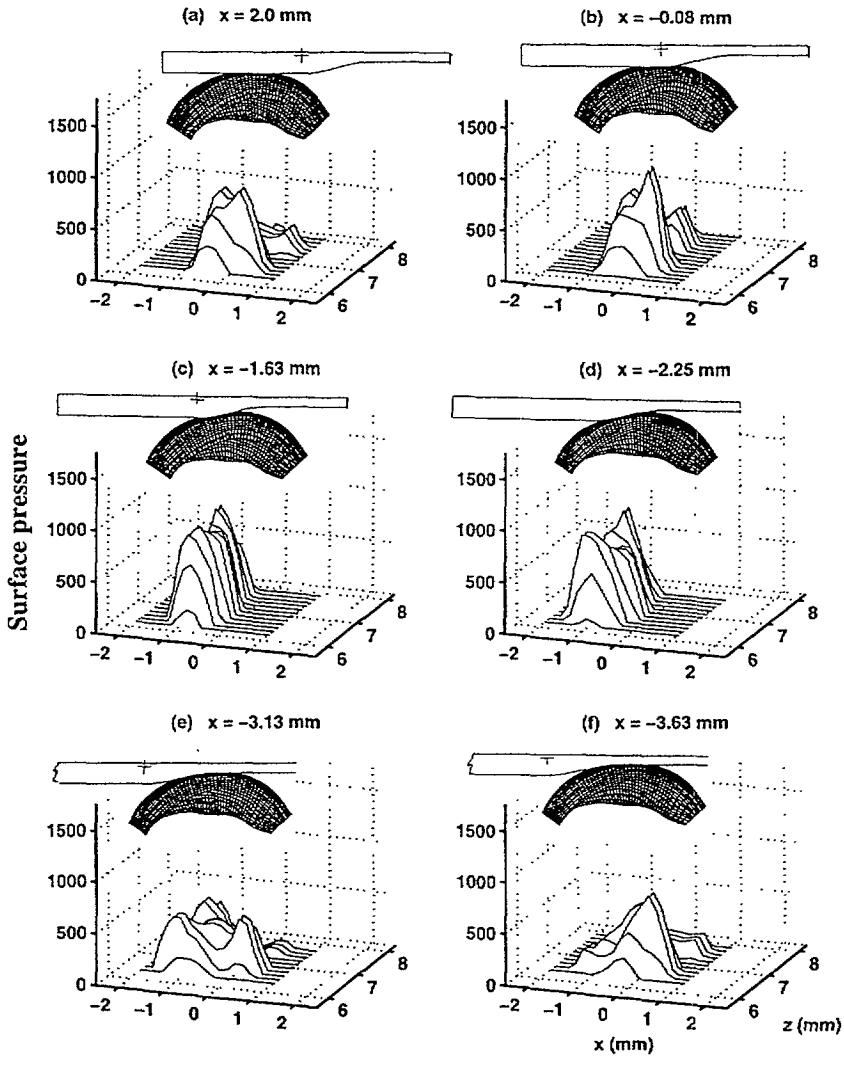

Figure 4-5: Monkey fingertip indented by the gradual sinusoidal step (step 5). The step was indented up to a prescribed force of indentation, the same force used in the indentation of the steep step. The pressure distribution on the skin surface and the extent of contact region are shown for six locations of the step indicated on top of each of the figures. Note that these locations are not the same as that shown in Figure 4-4 for step 1. For this gradual step, the contact region is continuous at all step locations. As in the case of step 1, the surface pressure shows the highest peaks under the most curved convex portion of the step. But the peak pressures are smaller and the contact regions are wider than those for step 1 indented with the same overall force.

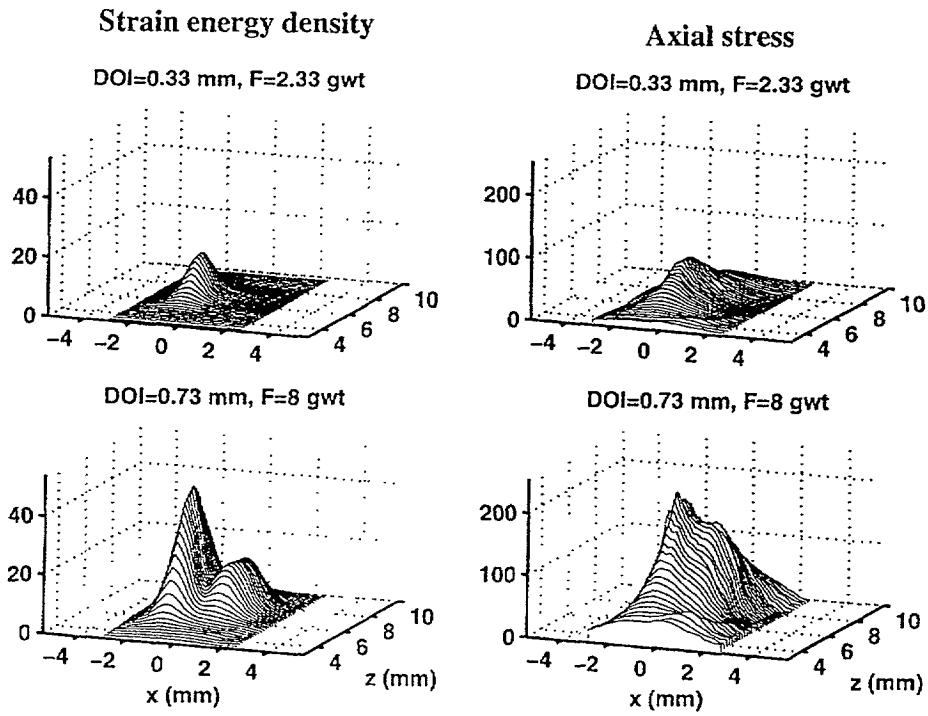

Figure 4-6: Subsurface strain measures for two different DOIs when step 1 is indented onto the monkey fingertip. The step is located at x = -1.63 mm (panel (e) in Figure 4-4 corresponds to this location). Distribution of two strain measures, strain energy density, and axial stress (normal stress component along the finger axis) are shown at a depth of 0.75 mm from the skin surface for two different DOIs. The lower DOI corresponds to the plots used to create Figure 4-4. The higher DOI of 0.73 mm corresponds to a force of 8 gram weight used by Srinivasan and LaMotte (1987). The axial stress is compressive. It can be seen that in the case of strain energy density, the distribution at lower DOI has only one peak. From Figure 4-4(e) it can be seen that the flat portion of the step barely touches the finger and hence does not cause a second peak in subsurface strain energy density. At a higher DOI, the strain energy distribution has two peaks which correspond to the two disconnected contact regions. In the case of axial stress, however, the distribution at both DOIs show only one peak.

Indentation by step 5

Figure 4-7 shows similar plots as Figure 4-6, but for the case of indentation by step 5. The step is located at x = -3.13 mm (see Figure 4-5 (e)). The main difference compared to step 1 is that even at the higher force of 8 gwt, strain energy density does not have two peaks. This is because in the case of this gradual step, the surface pressure does not contain two disconnected regions that are present for the steep step. Although the pressure distribution has two mild peaks (Figure 4-5(e)), after low pass filtering, the subsurface strain energy

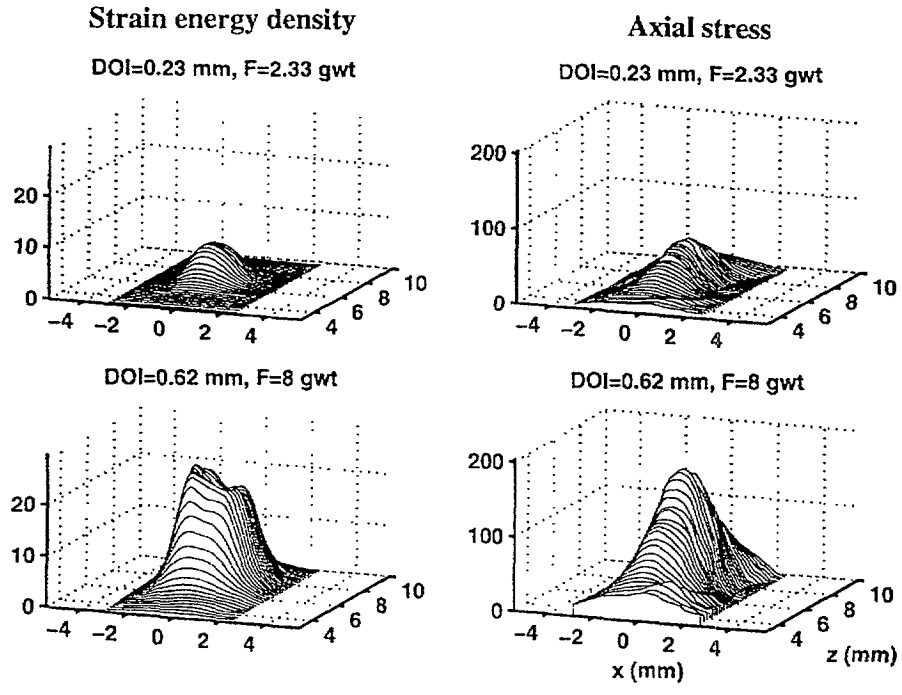

Figure 4-7: Subsurface strain measures for two DOIs (0.23 and 0.62 mm) when step 5 indented onto the monkey fingertip. The step is located at x = -3.13 mm (see panel (e) in Figure 4-5 which corresponds to this location). Same format as in Figure 4-6. In this case, even at the higher DOI, the strain energy density does not show two distinct peaks, in contrast to the corresponding case for step 1 (see Figure 4-6).

density is blurred out and contains mostly only a single peak. Axial stress shows only one peak and is similar to that of step 1. It is interesting that in spite of significant differences in the contact areas for steps 1 and 5 (as indicated by the extent of non-zero pressures in Figures 4-4 and 4-5), because of the blurring effects of low pass filtering by the skin, the subsurface quantities shown in Figures 4-6 and 4-7 have approximately the same overall widths.

Thus, with regard to encoding of object information by the SA-I afferents, the afferent response depends on (1) the shape of the object (in the case of strain energy density for the same force of indentation, step 5 does not have two separate peaks as does step 1) (2) the amount of loading, specified either by DOI or force of contact between the finger and the object (for the case of strain energy density, lower and higher DOI lead to different shapes

of distributions in the case of step 1), and (3) the strain measure that activates the receptor (strain energy density is different from axial stress).

Comparing Figures 4-4 and 4-5, it can be seen that step 5 requires a lower DOI to attain the same force of indentation (to reach an indentation force of 8 gwt, step 1 required a DOI of 0.73 mm whereas step 5 required only 0.62 mm). This is to be expected since step 5 has a more gradual profile, it has a higher area of contact as compared to step 1, and therefore encounters a higher resistance to indentation, and thus attains the same force for a smaller DOI.

4.3.5 Dependence of surface pressure and subsurface strain measures on the shape of the object

Having discussed the features of both surface pressure and subsurface strain measures, we now focus our attention on what attributes of object geometry (or, shape) determine the surface pressure intensities, and consequently the subsurface strain measures. Figure 4-8 shows the surface pressure distributions and strain energy density distributions at 0.75 mm and 2.5 mm depth from the surface, for the cases of indentation by the 3 mm rectangular bar, and 3 mm and 9 mm diameter cylinders. All the plots in this figure were extracted from the 3-D plots at a particular cross-section of the finger. The 3 mm bar has zero curvature (except at the edges), the 9 mm diameter cylinder has intermediate curvature and the 3 mm cylinder has the highest curvature among the three indentors. At a low DOI of 0.33 mm (when the edges of the rectangular bars do not contact the finger) the shape of the surface pressure distribution for the bar and the cylinders look similar in the overall shape in that all of them have have a single peak at the center. However the peak pressure and contact width are different – the bar has the lowest peak pressure but highest width of contact and the 3 mm diameter cylinder has the highest peak pressure, but smallest contact width. When the DOI is 1.33 mm, the surface pressure for the bar shows peaks at the edges whereas the surface pressure for both the cylinders maintain their overall shape. The strain energy density distribution has been plotted for all the three indentors at two receptor depths, 0.75 mm and 2.5 mm from the surface. When the DOI is 0.33 mm, the strain energy density distributions at both the depths have more or less the same shape. When the DOI is 1.33 mm the strain energy density at 0.75 mm depth is seen to be different

from one shape to another. The bar shows 2 peaks whereas the cylinders show more or less a single peak at the center. The two tiny peaks seen for the case of the 9 mm diameter cylinder is due to irregularities in the finite element mesh used. At a depth of 2.5 mm, the strain energy distributions for all the three indentors are almost identical in shape, and differ only in magnitude.

4.3.6 Relationship between surface pressure and object curvature

This section develops a quantitative model for the surface pressure. Figure 4-9 shows a plot of surface pressure (P) at each point within the contact region as a function of displacement at that point, for the three indentors discussed in the previous section (4.3.5). At a particular depth of indentation (DOI), several points on the finger contact the object and each point will have a different downward displacement (d). The surface pressure is non-zero only in the region of contact, but points that lie outside the region of contact may have non-zero displacements even though the surface pressure at those points is zero. For all the three indentors and for each DOI, the plot of P vs d is seen to be mostly a straight line characterized by two variables, a threshold and a scaling parameter. As the curvature of the indentor increases, P also increases. For all the indentors, the peak value of pressure within the contact region increases along a straight line whose slope is lower than the slope of the P vs d line for a particular DOI.

4.4 Discussion

4.4.1 Surface pressure

Throughout this chapter we studied the surface pressure distributions due to indentations by various shapes (bars, cylinders, sinusoidal shapes). The finite element models provided a way of computing the surface pressure distributions, which currently cannot be experimentally observed at an adequate spatial resolution. The surface pressure distribution is important, as it determines the input to the tactile system from a systems point of view. The task is to relate the object's shape to the surface pressure. We have seen that the surface pressure is influenced by both the curvature of the object and the downward displacement at each point within the contact region where the surface pressure is measured.

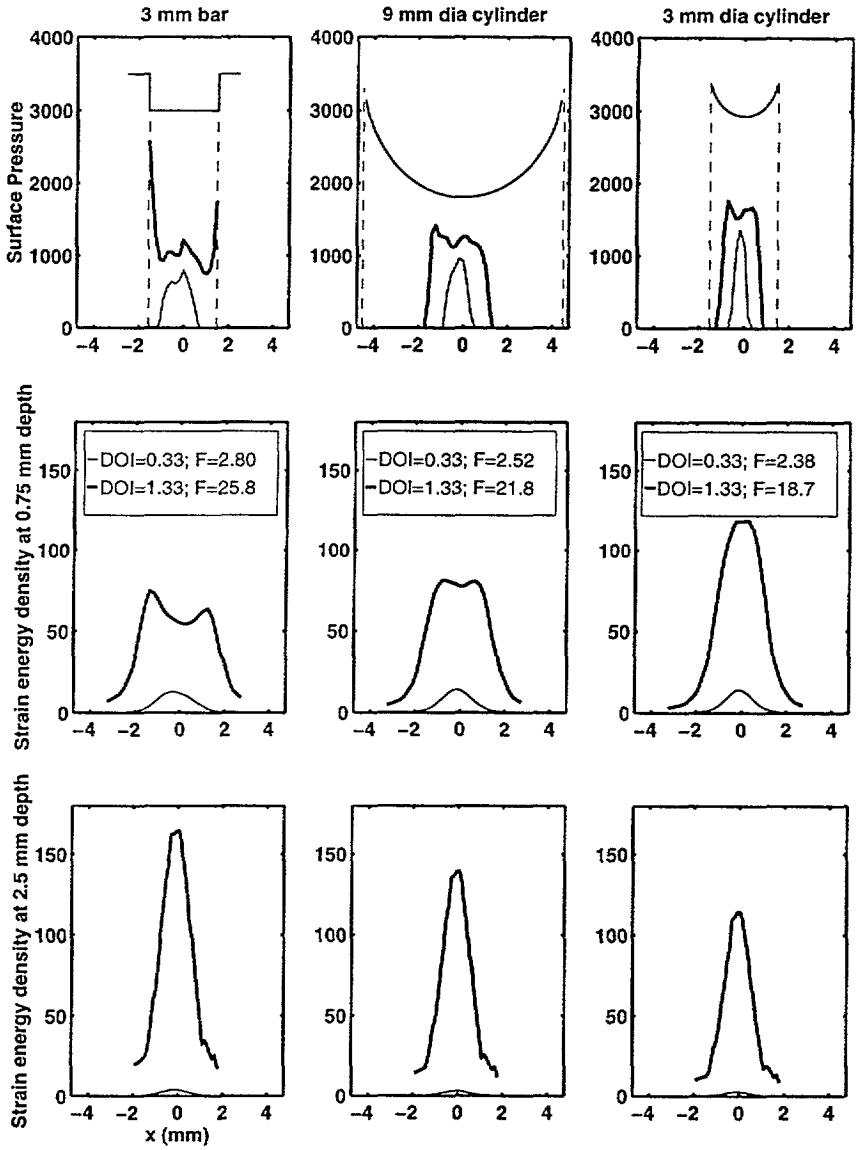

Figure 4-8: Differences in surface pressure distributions and strain energy density due to bar and cylinder indentations. The DOI and force (F) are expressed in mm and gwt respectively. At a low DOI of 0.33 mm (when the edge of the bars do not contact the finger) the shape of the surface pressure distribution for both the bar and cylinder indentations look similar in shape, but the peak pressures and width of contact are different -- the bar has the lowest peak pressure but highest width of contact and the 3 mm diameter cylinder has the highest peak pressure, but smallest width of contact. When DOI=1.33 mm the edges of bars contact the finger and the surface pressure has peaks at the edges. The strain energy density distribution at depths of 0.75 mm and 2.5 mm from the surface are low pass filtered versions of the surface pressure distributions. When DOI is 0.33 mm, the strain energy density looks similar for all the shapes. When DOI is 1.33 mm, the strain energy density distributions at 0.75 mm depth look different for the three shapes, but those at 2.5 mm depth are almost identical in shape, differing only in magnitude.

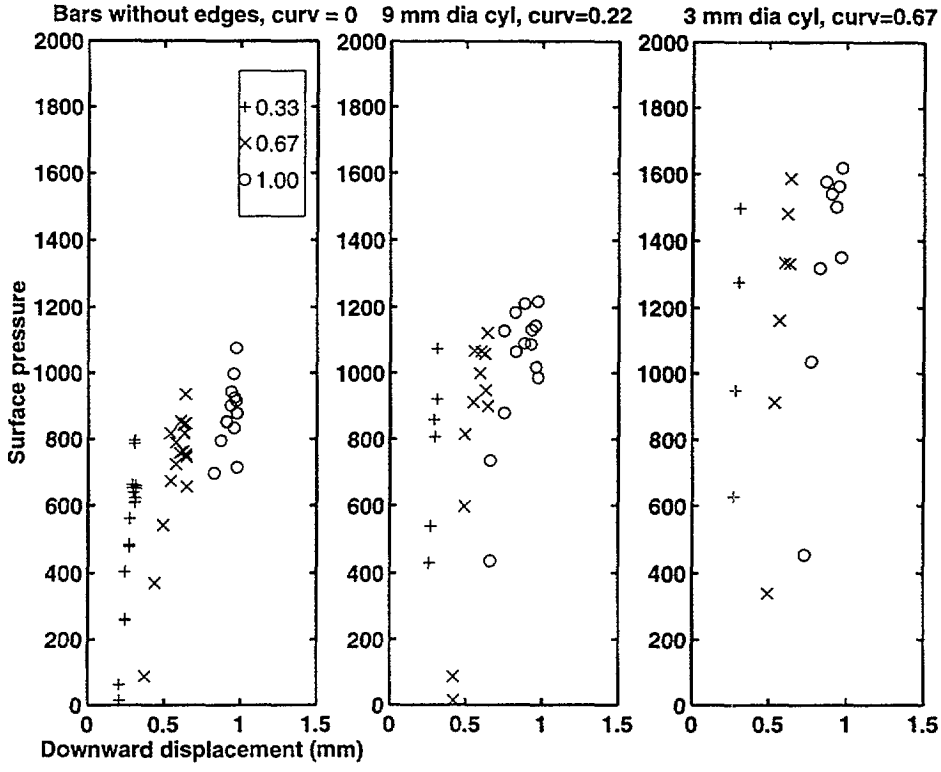

Figure 4-9: Dependence of surface pressure on skin displacement and curvature of the indentor. The left panel contains data from both the 1.5 mm and 3 mm wide bars, but with the edge effects omitted (as the edges have infinite curvature). The x-axis is the vertical displacement at the point where the surface pressure is computed. The values shown in the legend are the DOIs in mm.

Based on the observations from Figure 4-9, we propose the following model for the surface pressure:

$$\mathrm{P} = K_2(d - d_0) + K_3\mathrm{C} \tag{4.1}$$

where P is the surface pressure at a point on the skin surface, d is the vertical displacement of that point, d_0 is a threshold parameter that depends only on the overall depth of indentation (DOI), K_2 and K_3 are scaling constants, and C is a measure of the relative curvature between the finger and the object contacting the finger. The above expression implies that P has two contributions: one purely due to curvature and the other purely due to the downward displacement of the skin surface. Figure 4-10 provides an illustration of this model. To explain this figure, we first assume that the contacting object has zero relative curvature. At a particular point, the surface pressure varies linearly with its vertical displacement, shown by dashed lines with slope K_1. For a given DOI, only points that

are in contact with the object have non-zero pressures. The threshold displacement (d_0) corresponds to the minimum of the displacements of all points within the contact region and generally occurs at a boundary point. Points lying outside the contact region will have displacements smaller than this threshold displacement, but will have zero pressure. The threshold is not a constant – it increases with increasing overall DOI. This is true because, with increasing DOI, the smallest displacement within the region of contact also increases. From Figure 4-10, the value of threshold can be seen to be

$$d_0 = \text{DOI}(1 - \frac{K_1}{K_2}) \tag{4.2}$$

Thus P in Equation 4.1 can be written completely in terms of only three parameters K_1, K_2 and K_3 (for a given overall DOI and relative curvature C).

As the DOI increases (shown by the horizontal arrows), the threshold displacement and the area of contact both increase. Beyond a level of indentation, the area of contact does not increase and the P vs d plot starts to move up at an angle (shown by the angled arrow) whose slope is exactly K_1. This is because there is no more contact mechanics and all points on the indentor have contacted the finger.

We now consider the effect of curvature. If the indentor has a non-zero relative curvature, two additional effects happen: (i) all the P vs d plots are simply shifted vertically upwards (shown by the vertical arrow). The shift is taken to be directly proportional to the relative curvature (ii) the slope K_2 increases with increasing relative curvature. A simple shift implies that all points within the region of contact have a non-zero value of surface pressure. However, for smooth objects without edges (e.g. cylinders) the surface pressure falls to zero at the ends of the contact. This is a limitation of the proposed model. However as seen in Figure 4-9 this model explains most of the features of the surface pressure and is also simple to use. To summarize, the surface pressure distribution, for a given object geometry and DOI, depends on only three parameters: K_1, K_2 and K_3.

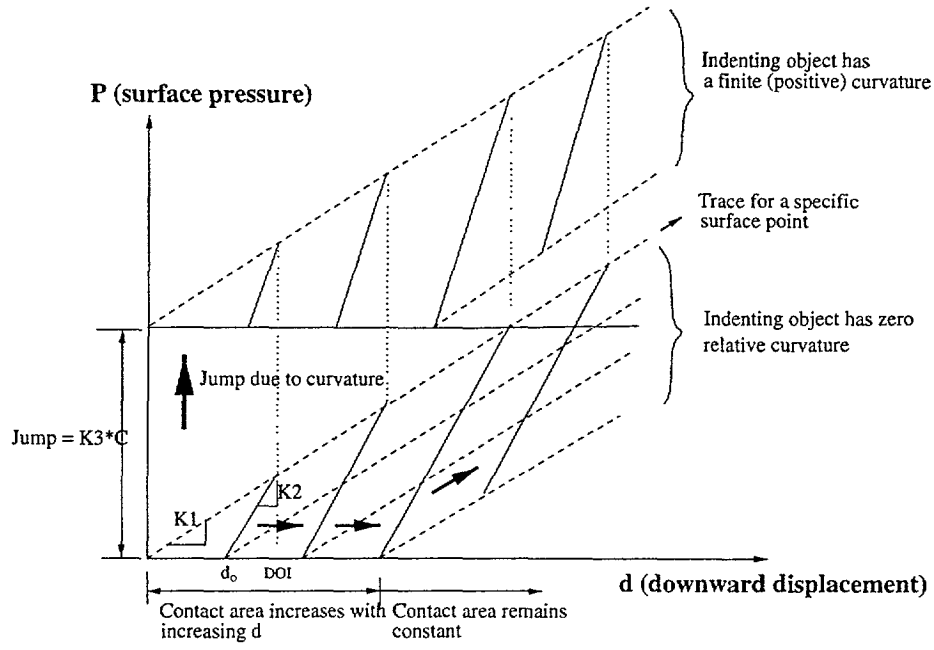

Figure 4-10: Quantitative model for skin surface pressure under shaped objects.

4.4.2 Subsurface strain measures

The subsurface strain measures were found to be low pass filtered versions of surface pressure. Different strain measures had different distributions. This implies that receptors that transduce different strain measures will receive different information to transduce into neural responses. This result is significant not only for human tactile sensing, but also robot tactile sensing.

4.4.3 Receptor depths

The depth at which the strain measures are computed is important because the skin tissues low pass filter the surface pressure distributions. From Figure 4-8 it was seen that if the receptors are at 2.5 mm depth from the surface, the strain energy density becomes blurred enough that there is no identifying difference between the distributions due to different indentors. Thus receptors located at a depth of 2.5 mm cannot properly distinguish between different kinds of shape. Thus it is likely that the deeper receptors like Pacinian

corpuscles are unlikely to aid in shape perception. The merkel cells innervating the SA-I are at about 0.75 mm depth and hence can participate in coding of shape information.

5 Relevant Stimulus

5.1 Motivation

The previous chapter dealt with the mechanistic aspects of tactile sensing – the relationship between object geometry and surface pressure, and the computation of subsurface strain measures. This chapter deals with the link between the subsurface strain measures and experimentally recorded neural impulses of the SA-I afferents. Studying this transduction mechanism requires computation of the strain measures in the vicinity of the mechanoreceptors and also experimental recordings of neural responses of the afferent nerve fiber. Previous studies in this area have used simplified, 2D models of the finger to compute the strain measures. In this chapter, the 3D multilayered finite element model of the finger is used to compute strain measures at the vicinity of the mechanoreceptors. Then, these strain measures are analyzed to see which one of them would best match available recorded neural responses for the case of SA-I afferents [1].

5.2 Methods

5.2.1 Simulation of neurophysiological experiments involving stimulus shapes indented onto the monkey finger pad

All the neurophysiological experiments were simulated using the three dimensional multilayered finite element model of the primate fingertip described in Chapter 3. The model was used to simulate the neurophysiological experiments of (1) Srinivasan and LaMotte (1987) wherein sinusoidal step shapes were indented up to a predetermined force of

[1]The neurophysiological data used in this Chpater is taken from Phillips and Johnson (1981a) and Srinivasan and LaMotte (1987) and the author wishes to acknowledge the same.

indentation and (2) Phillips and Johnson (Phillips and Johnson, 1981a) wherein rectangular bars and gratings were indented up to a prescribed depth of indentation. The nonlinear contact problem between the stimulus shape and the finger pad was solved iteratively until the prescribed force or depth of indentation was reached (more explanation is given in Chapter 4). The stimulus shapes were considered rigid and frictionless. To construct the *simulated spatial response profile (SSRP)* the stimulus object was indented successively at different lateral locations and the problem was solved at each location.

(a) **Sinusoidal Steps:** In the experiments of Srinivasan and LaMotte (1987) six steps were used. In this work three of them denoted as step 1, step 3 and step 5 are used for comparison between the neurophysiological data and simulation results. For the most part, the lateral locations were separated by about 170 microns, which was the spacing between the nodes on the model. It is to be noted that the minimum stepping distance is the spacing between the nodes. To reduce computational effort, the spacing between lateral locations was increased in situations where the sinusoidal portion of the step was away from the central region of the finger pad. Totally about 20 indentations per step were simulated. Since the stepping distance in the experiment was not the same as that in the simulations, a linear interpolation was used to obtain the simulation data at the locations used in the experiment.

(b) **Rectangular bars:** Phillips and Johnson (1981a) used gratings consisting of rectangular bars to indent the monkey finger pad and recorded the SA-I neural response. The gratings were indented up to a prescribed depth of indentation of 1.0 mm. Since simulating the entire experiment using the full grating would be computationally very expensive, only isolated rectangular bars of 1.5 mm and 3 mm width were used. In the simulations, the rectangular bars were indented onto the finger pad up to 1 mm depth in four increments of 0.25 mm each. The bars were stepped laterally at a spacing of 170 μm and the simulation was done for several locations (25 locations for the 1.5 mm bar and 34 locations for the 3 mm bar) to obtain data for constructing the SSRP.

5.2.2 Receptor locations

To study the dependence of SSRP on the location of the receptor, ten receptor locations on a cross section of the fingertip were chosen. The cross sectional plane was located at 5.86 mm from the distal tip of the finger and the receptors were located at 760 microns below the skin surface. The lateral locations of the receptors were x = -2.0, -1.5, -1.25, - 1.0, -0.5, 0, 0.5, 1.0, 1.5 and 2.0, all expressed in mm. The location x = 0 corresponds to the center of the finger pad.

5.2.3 Stress/Strain measures

Indentation of the finger pad by a stimulus shape leads to a distribution of stresses and strains at every point below the skin surface. Stresses, having the units of force/area, measure the intensity of loading (e.g., pressure) at that point. Strains, being a ratio of the change in length to the original length of a material element, are non-dimensional. Both stresses and strains are direction dependent. In the 3D space considered here, they are both 3×3 cartesian tensors (matrices) and have nine components in each of them, of which only six are independent (the matrices are symmetric). Of the six independent stresses, three are normal stresses and three are shear stresses. In this work, the normal stresses are denoted as s11, s22 and s33. The shear stresses are denoted as s12, s23 and s13. Similarly there are six independent strains, of which the three normal ones are denoted as e11, e22 and e33 while the three shear strains are denoted as e12, e23 and e13. It is to be noted that though the three normal strains can be calculated from the three normal stresses by the multiplication of a matrix whose elements are governed by material properties such as stiffness and compressibility, individually they are not directly proportional to the corresponding normal stresses. For example, e11 does not simply scale with s11, but depends on s22 and s33 as well. However, each of the three shear strains are proportional to the three corresponding shear stresses. For example, the shear strain e12 is equal to $\frac{s12}{G}$ where the constant G is the shear modulus of the material of the tissue at the location where the mechanical quantities are measured. Hence in the search for the relevant stimulus by matching the shapes of recorded and simulated SRPs, it is enough to consider either the shear strains or shear stresses. In this thesis, shear strains are used.

From the normal and shear strains defined along the coordinate axes, three principal components can be calculated, two of which represent the maximum and the minimum values of the strains. The three principal strains are denoted as ep1, ep2 and ep3 [2]. Using a much simplified model of the finger pad, the maximum compressive strain was found to be the relevant stimulus for static response of SA-Is by Phillips and Johnson (1981a). In our simulations, ep1 is the maximum compressive strain and ep3 is the maximum tensile strain. The intermediate principal strain ep2 was found to be mostly tensile. In contrast, all the three principal stresses were found to be compressive. Hence they are referred to as maximum compressive stress (sp1), intermediate principal stress (sp2) and minimum compressive stress (sp3).

Additionally, the stress tensor has three "invariant measures" - quantities that do not change with orientation of coordinate axes. The first stress invariant is the mean of the three normal stresses and is referred to as mean normal stress. Physically, the mean normal stress is a measure of the hydrostatic pressure at that particular point. The second stress invariant is related to strain energy density, which is a measure of the distortion at the particular point. The third stress invariant has no known physical significance, but is mathematically equal to the determinant of the stress tensor and is included for sake of completeness. Thus a total of 18 stress and strain measures (3 normal stresses, 3 principal stresses, 3 normal strains, 3 shear strains, 3 principal strains and 3 stress invariants), hereafter referred to as candidate measures were considered in the search for relevant stimulus. In this thesis we will study whether one or more of the above candidate measures is closely related to the experimentally determined spatial response profile (SRP).

5.2.4 Comparison of recorded neural data and strain measures

Figure 5-1 (a) shows the recorded SRP for steps 1, 3, and 5, replotted as the mirror image of Figure 4 in Srinivasan and LaMotte (1987). As the step is moved from *right to left*, first

[2]In solid mechanics, ep1, ep2 and ep3 are commonly referred to as minimum principal strain, intermediate principal strain and maximum principal strain, as compressive strains are assigned a negative sign. With this sign convention, ep1 < ep2 < ep3. Similarly the three principal stresses are denoted as sp1, sp2 and sp3, where sp1 < sp2 < sp3. Alternate names for sp1, sp2 and sp3 are minimum principal stress, intermediate principal stress and maximum principal stress. In plotting the above stress/strain measures, if any particular measure was always found to be negative (i.e., compressive), then its magnitude was used. For example, the maximum compressive strain is always negative and hence its absolute value is used.

the lower flat part of the step is in contact, then the convex part moves towards a centrally located receptor, followed by the concave part and then the upper flat part. The SRP from right to left, first shows a rise to a peak, followed by a dip and then rise to a final value that is about the same as the initial value. The rise in discharge rate occurs when the convex portion of the step is directly above the receptor while the dip occurs when the concave portion is above the receptor. In order to determine if a candidate measure is closely related to the recorded neural responses, it is necessary that the SSRP based on the candidate measure should also have the peak-dip characteristic. SSRPs that did not show the peak-dip characteristic were considered not to match the shape of the recorded SRP. Also, relative to the response to flat parts, since the increase in the neural response rate due to the convex portion of the step is much higher than the decrease in the neural response rate due to the concave portion of the step, the SSRPs whose dip was more than the peak were considered not to match the shape of the recorded SRP. To reduce the long list of 18 candidate measures, we first compared the SSRP of each strain measure due to indentation by step shapes with that of the recorded SRP. Once we narrowed down the list we then used the recorded SRP for the case of rectangular bars (Figure 5-1 (b)) to further reduce the list. The SRPs for both the bars showed two peaks corresponding to the two edges and a dip when the center of the bar was above the receptor and hence candidate measures that did not show this peak-dip-peak trend were considered unlikely to be the relevant stimulus.

In order to mathematically relate the experimentally recorded neural responses to a particular strain measure, a quasi-linear receptor model, same as that used by Phillips and Johnson (1981b), with two parameters representing scaling and threshold was used. The model can be represented mathematically as $R = k(\epsilon - \epsilon_0)$ where R is the neural discharge rate, ϵ is the candidate measure, and k and ϵ_0 are the scaling and threshold parameters respectively.

5.2.5 Generation of SSRP from population response

Figure 5-2 illustrates how the spatial response profile is obtained from the population responses. First, population responses were obtained for several locations of the indentor. For the case of sinusoidal steps, about 22 locations were used. At each location the contact

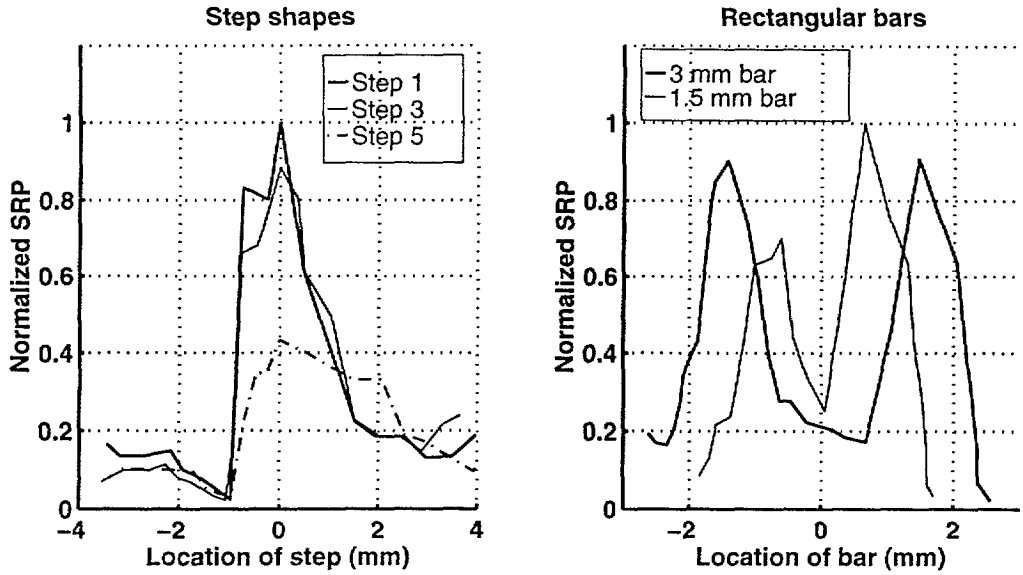

Figure 5-1: Experimentally recorded spatial response profile (SRP) for sinusoidal step and rectangular bar indentations, taken from Srinivasan and LaMotte (1987) and Phillips and Johnson (1981b), respectively. In (a), the SRPs for three steps are shown as mirror images of Figure 4 in Srinivasan and LaMotte (1987). All the three SRPS are normalized with respect to the maximum response rate for step 1. The location of the step is taken to be the lateral location of the sharpest point of the step on the skin surface measured with respect to the center of the receptive field of the receptor. The steps are moved from right to left over successive indentations. The SRPs show a peak when the convex part of the step is directly above the receptor and a dip when the concave part of the step is above the receptor. In (b), the SRPs for indentations by 3 mm and 1.5 mm wide rectangular bars are shown. Both the SRPs are normalized with respect to the maximum response rate for the 1.5 mm bar. The location of the bar is the location of the center of the bar measured with respect to the center of the receptive field. The SRPs show two peaks when the edges of the bars are directly above the receptor and a dip when the center of the bar is above the receptor.

mechanics problem was solved and all the mechanical quantities were obtained. Plotting the value of the candidate measure as a function of receptor location gives the population response - such a population response was obtained for each location of the indentor. From these population responses, the values of the candidate measure for any given receptor location were extracted for each of the indentor locations. These extracted values were then plotted as a function of the step location. In the example shown in Figure 5-2, five step locations were shown. The corresponding five population responses are shown. The values of the population responses at -1.0 mm are extracted and used to plot the SSRP. All the plots were generated using the Matlab software package. Also, a library function

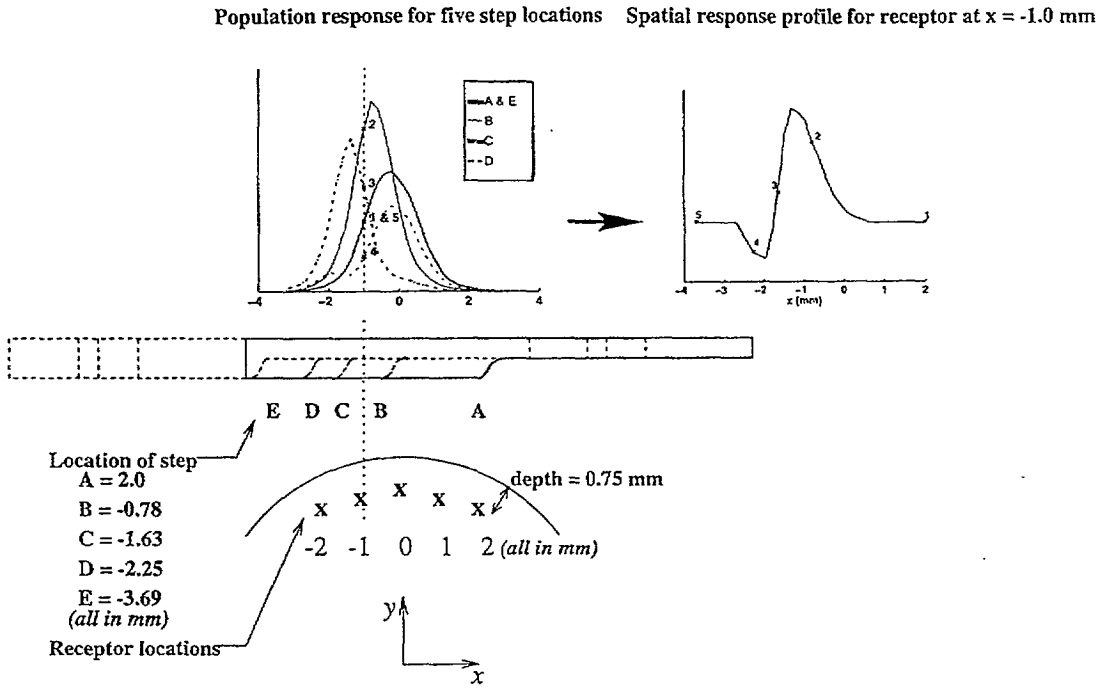

Figure 5-2: Extraction of simulated spatial response profile (SSRP) from the population response. The step (step 1) was moved from right to left over successive indentations. The graph on the left shows population response for five locations of the step denoted by A, B, C, D and E. The values of the population response at a particular receptor location were then extracted from these population responses to generate the SSRP. This example demonstrates how the SSRP for the receptor at x = -1.0 mm was generated. The numbers 1 through 5 denote the values of the population responses corresponding to the receptor located at -1.0 mm for the five step locations. Note that 1 and 5 were the same because the indentations corresponding to A and E are mechanically identical - in both cases only flat portions of the step touch the finger. The values 1 through 5 are plotted with respect to the step location to generate the SSRP for that receptor (graph on the right).

in Matlab was used to compute correlation coefficients to measure the goodness of fit between a candidate measure and the experimentally recorded neural responses.

5.3 Results

5.3.1 Influence of force of indentation on the population response and SRP

In the neurophysiological experiments by Srinivasan and LaMotte (1987) the step shapes were indented up to a force of indentation of 8 gwt. The higher the force of indentation,

the higher is the computational effort required to simulate the experiment. This is because as indentation progresses from initial contact, the contact region gradually changes, requiring computation of the solution (i.e., the determination of stresses and strains within the fingertip) for each increment in force. In this section we demonstrate that a lower force of indentation (approximately 2.33 gwt.) could be used to match experimentally recorded SRPs with those obtained through simulations (SSRPs).

For this purpose, we simulated the neurophysiological experiments for five locations of step 1, with the force of indentation being equal to that used in the experiments. Figure 5-3 shows the population response and SSRPs obtained for the higher force of indentation (corresponding to that used in the experiment) and a lower force of indentation equal to about a third of that used in the experiment. It can be seen that the shape of the population response can be quite different for the two forces of indentation at certain locations. At the higher force of indentation, the population responses have two peaks when the step is located at -1.63 mm, but at the lower force of indentation the population responses have only a single peak. The reason is that at the lower force, only the convex portion of the step is in contact with the finger pad, whereas at the higher force, the upper flat part of the step also comes into contact. At step locations of 2.0 and -3.69 mm also the higher force of indentation leads to two peaks, but these two peaks merge and hence they are not distinguished clearly. But the lower force of indentation leads to only a single peak. For step location at -2.25 mm the higher force of indentation leads to two peaks with almost equal magnitudes but the lower force of indentation leads to two peaks with a smaller magnitude for the second peak. Thus the population responses for the two forces of indentation are quite different. Figure 5-3 also shows the comparison between the SSRPs obtained for five receptor locations. Since the simulations with higher force of indentation are computationally expensive, only four simulations were done with this force (the fifth simulation is identical to the first one, because only the flat portion of the step contacts the finger in both the cases). It can be seen that the shape of the SSRPs are not very different for the two forces of indentation. The same trend is seen for both the forces in SSRPs for the receptors at -2.0, -1.0 and 0.0. For example the receptor at -1.0 mm shows the rise-dip trend for both the forces of indentation. The receptors at +1.0 and +2.0 mm also show similar trends for both the forces of indentation, except that the dip in the graph is shifted

to the right for the case of higher force of indentation. The overall shape is however same for all the receptor locations. The shift in the dip for positive receptor locations does not affect our further analyses because the selection of the relevant stimulus is based on the match between overall shape of the SSRP with that of the experimentally obtained SRP (a shift in the dip or an increase in magnitude does not affect the overall shape). Therefore, from now on, all our results on SSRPs are based on the lower force of indentation.

5.3.2 Influence of receptor location on the SSRP

Figure 5-4 shows the SSRPs for the case of maximum compressive strain for 10 receptor locations, all at a depth of 0.75 mm from the skin surface (Figure 5-2). The SSRPs for the ten locations are all different from one another. For example, none of the receptors at positive locations show the peak-dip trend. All of them show only a single dip. Among the receptors at negative locations many show the peak-dip characteristic. The receptors at -1.5, -1.25 and -1.0 show the peak-dip characteristic that is consistent with the experimentally recorded SRP. The receptors at -0.5 and 0.0 show a dip that is higher in magnitude than the peak and hence their SSRPs do not match that of the experimentally recorded SRP. The receptor at -2.0 does not show the dip and hence its SSRP does not match that of the experimentally recorded SRP. Thus it is clear that the shape of the SSRP greatly depends on the location of the receptor within the finger. Our first objective then is to determine, for a given strain measure, if any of the receptors would show the trend that is consistent with the peak-dip trend seen in the experimentally recorded SRP. In the following paragraphs we illustrate this procedure with several candidate measures and their SSRPs based on five receptor locations, for the case of indentation by step 1. In Table 5.2 we then summarize for all the candidate measures and for all the 3 step shapes, which receptor locations would have an SSRP that can match the experimentally recorded SRP.

Figure 5-5 shows the SSRPs based on three strain measures, namely tensile strain ep3, shear strain e13 and axial tensile strain e33, when step 1 is indented onto the finger pad. These quantities were chosen so as to have one measure from each category of strain - principal, shear and normal. The results are shown for five receptor locations. It can be seen that in the case of ep3, the receptor at -1.0 shows the peak-dip characteristic of recorded SRP (Figure 5-1 (a)). The receptor at -2.0 does not show a dip. The receptor at 0.0 shows a peak that is of higher magnitude than the dip. The receptors at 1.0 and 2.0 show

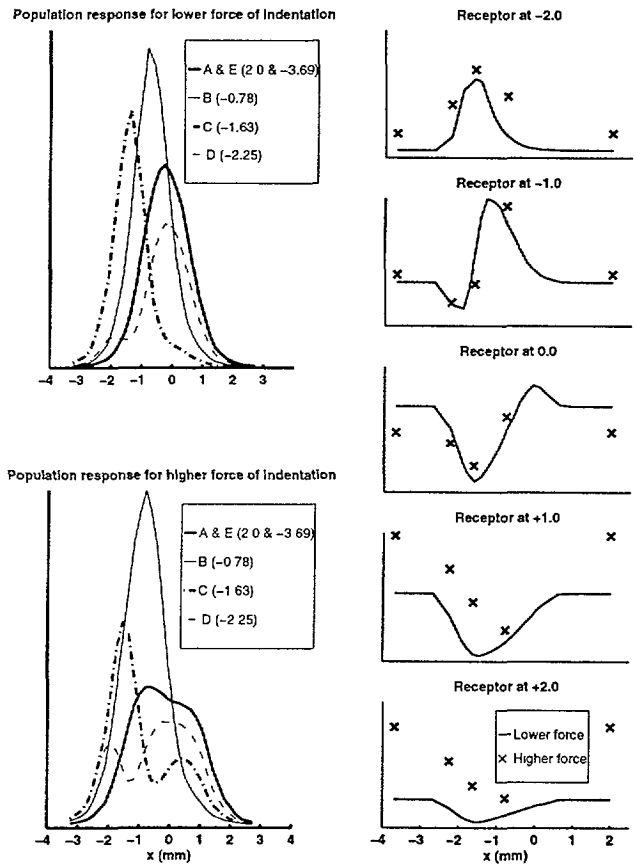

Figure 5-3: Influence of force of indentation on the population response and the SSRPs. The two graphs on the left show population responses obtained from the fingertip model for five locations of step 1. The higher force of indentation (8 gwt.) corresponds to that used in the experiment while the lower force of indentation (2.33 gwt.) corresponds to that used in most of the simulations. For both the cases the response values are individually normalized with respect to their maximum values. The actual peak magnitude for the case of higher force of indentation is about five times higher than the peak magnitude for the case of lower force of indentation. The population responses for the lower force of indentation show only a single peak (except for a small second peak when the step is at -2.25). The population responses for the higher force of indentation show two peaks when the step is at -1.63 mm. Thus the population response is dependent on the force of indentation, except for when only the flat part of the step is fully in contact (i.e., for step locations 2.0 and 3.69 mm). The figure on the right shows the SSRP for both the forces of indentation for five receptors. For the receptors located at -2.0, -1.0 and 0, the shapes of the SSRPs are the same for both the forces of indentation. The receptors at +1.0 and +2.0 also show the same shape for both the forces, except that the dip is shifted to the left for the higher force of indentation.

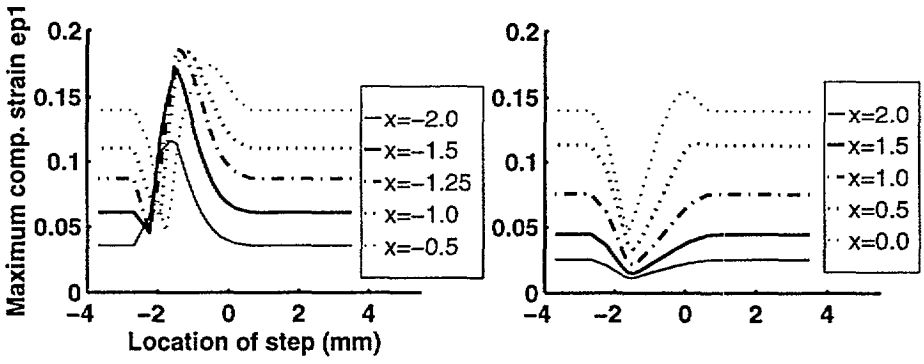

Figure 5-4: SSRPs for step 1 with maximum compressive strain as the candidate measure for 10 receptors. The receptor locations (x) are indicated in mm. The location of the step is the location of the most convex part on the step measured with respect to the center of the finger. The shape of the SSRP depends strongly on the location of the receptor. The receptors located at positive locations (x > 0) show a single dip. All the receptors located at negative locations, except for the one at x = -2.0 mm, show a peak-dip characteristic. Only the receptors at -1.5, -1.25 and -1.0 show the peak-dip characteristic that would match the experimentally recorded SRP (Figure 5-1(a)).

only a dip. In the case of shear strain e13 the receptors at -1.0 and 0.0 show the peak-dip characteristic. In the case of axial strain e33, none of the receptors show the peak-dip characteristic.

Figure 5-6 shows the SSRPs for minimum compressive stress sp3, shear stress s23 and vertical compressive stress s22 for the case of indentation by step 1. As in the case of strains, these stresses represent a candidate from each of three stress types - principal, shear, and normal. In the case of s22, the receptor at -1.0 shows the peak-dip trend of the recorded SRP, while the receptors at other locations do not show the trend. In the case of minimum compressive stress sp3 and shear stress s23, none of the receptors show the peak-dip trend of the recorded SRP.

Figure 5-7 shows the SSRPs for mean normal stress, strain energy density, and the third stress invariant for step 1. These three "invariants" are quantities that do not change with

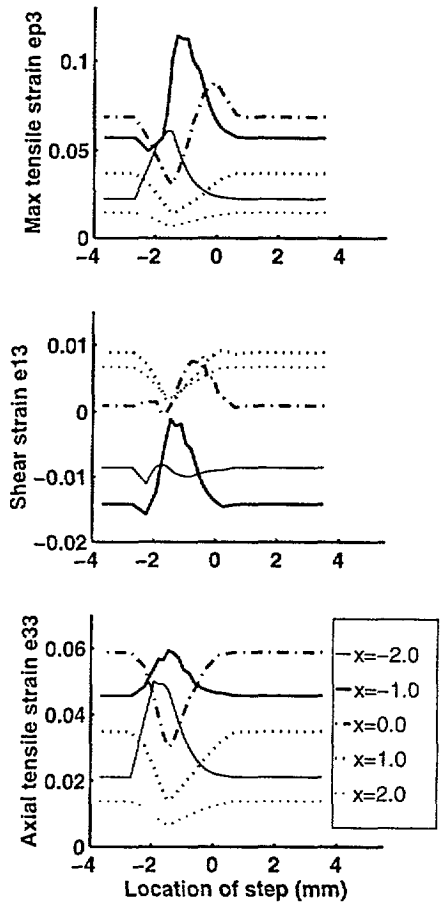

Figure 5-5: Step 1 SSRPs for three strains - maximum tensile strain ep3, shear strain e13 and axial strain e33. The SSRPs are shown for five receptor locations. The SSRP for all the three strains depends on the location of the receptor. For example, in the case of maximum tensile strain, the receptor at -1.0 shows the peak-dip trend whereas the receptors at other locations do not show the trend.

orientation at that location. The receptor at -1.0 shows the peak-dip trend for both mean normal stress and strain energy density. The receptors at other locations do not show the peak-dip trend. The third stress invariant at -1.0 shows a very sharp peak and a broad dip that is the mirror image of the empirical SRP and hence is unlikely to be the relevant stimulus.

Thus it is clear that the location of the receptor plays an important role in determining the kind of mechanical stimulus it receives. At a given location, it is also clear that the

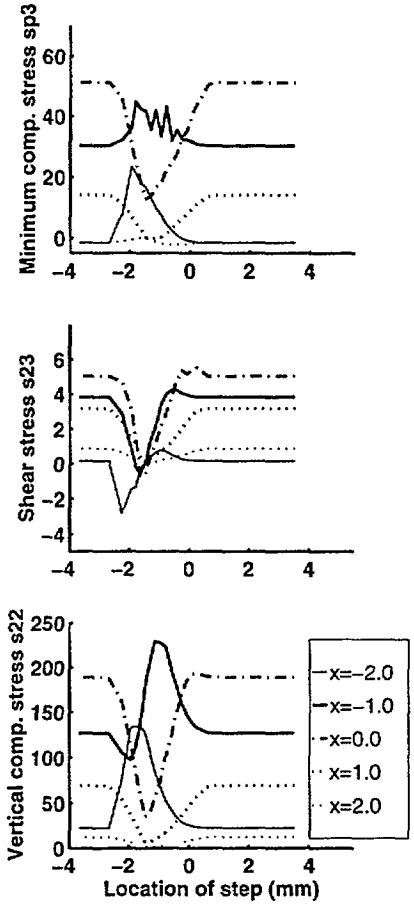

Figure 5-6: Step 1 SSRPs for three stresses - minimum compressive stress sp3, shear stress s23 and vertical compressive stress s22. The SSRPs depend on the location of the step. Whereas s22 has only one location (-1.0) that showed the peak-dip characteristic, the other two stress measures do not have any receptor locations at which the peak-dip characteristic emerges.

shape of the SSRP depends on the candidate measure. If the receptors were to linearly transduce any one of the above candidate measures above a certain threshold into neural responses, then the shape of the SSRP should match that of the experimentally recorded SRP.

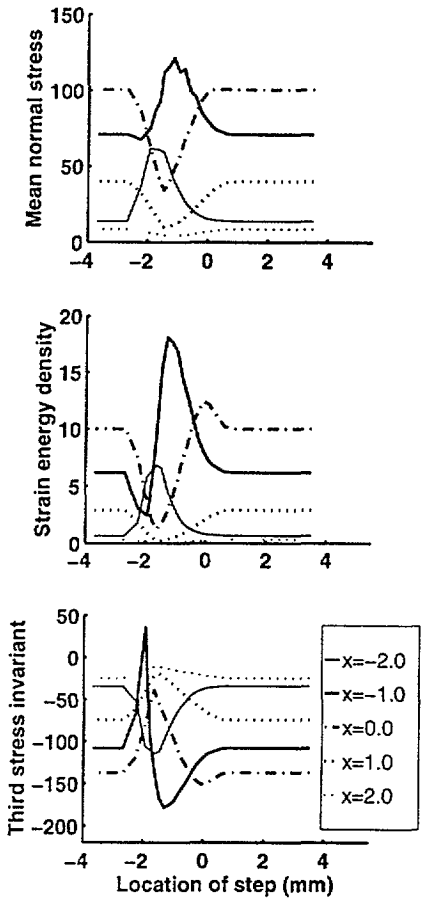

Figure 5-7: Step 1 SSRPs for mean normal stress, strain energy density and the third invariant of stress tensor. As in the previous four figures, the receptor location dominantly influences the SSRP.

5.3.3 Correlation coefficient is alone not a good indicator for determining relevant stimulus

In order to determine the relevant stimulus for SA-I receptors under static stimuli a goodness of fit measure, usually the correlation coefficient, has been used in previous works (Phillips and Johnson, 1981b; Srinivasan and Dandekar, 1996). Correlation coefficient is a measure of how well two sets of data points match each other in the overall sense and does not depend upon the specific features of the two set of data points. In this section we illustrate that the correlation coefficient alone cannot be used to infer the relevant stimulus. Table 5.1 shows the correlation coefficient between the SSRP as predicted by

Location (mm)	Max comp. strain ep1	Min comp. stress sp3	Strain energy density
-2.00	0.9631	0.9377	0.9565
-1.50	0.9716	0.9485	0.9543
-1.25	0.9557	0.9233	0.9339
-1.00	0.9159	0.9691	0.9483
-0.50	0.8087	0.9651	0.7452
0.00	0.9255	0.9378	0.9120
+0.50	0.9468	0.9161	0.9413
+1.00	0.9401	0.9262	0.9228
+1.50	0.9357	0.9220	0.9169
+2.00	0.9354	0.7804	0.9212

Table 5.1: Correlation coefficients between SSRP and recorded SRP for three strain measures, for the case of indentation by step 1. The recorded SRP was taken from Srinivasan and LaMotte (1987).

the strain measures and the experimentally recorded SRP for three candidate measures: maximum compressive strain ep1, minimum compressive stress sp3, and strain energy density. For each strain measure the correlation coefficients are tabulated for ten receptor locations. Two points can be noted: First, in the case of maximum compressive strain and strain energy density, even though the receptors at positive locations did not match the shape of the experimental SRP (no peak-dip characteristic), some of them have high correlation coefficients. Second, in the case of minimum compressive stress, even though none of the SSRPs at ten different locations matched the recorded SRP, many of them show high correlation coefficients. Hence by using correlation coefficient alone it is not possible to decide which strain measure best matches the experimental SRP.

5.3.4 Determination of the relevant stimulus

SSRP based on the mechanical stimulus should predict the shape of experimental SRP for all three step shapes

Since the experimental SRPs were recorded from the same peripheral nerve for all the three steps, two conditions should hold: (1) The SSRPs predicted by the relevant stimulus should be able to match the shape of the corresponding experimental SRPs for all three step shapes - step 1, step 3 and step 5; (2) there should be at least one matching receptor

Strain measure	Step 1 alone	Step 3 alone	Step 5 alone	Common
Normal strain e11	-1.0, -1.25, 1.5	-1.0, -1.25	none	none
Normal strain e22	-1.0, -1.25	-1.0, -1.25	-0.5	none
Normal strain e33	none	none	none	none
Shear strain e12	0	none	none	none
Shear strain e23	none	none	none	none
Shear strain e13	0, -0.5, -1.0, -1.25, -1.5	0, -0.5, -1.0, -1.25, -1.5	-1.0, -1.25	-1.0, -1.25
Max comp. strain ep1 (Min principal strain)	-1.0, -1.25, -1.5	-1.0, -1.25, -1.5	-0.5, -1.0	-1.0
Intermediate principal strain ep2	none	none	-1.0, -1.25	none
Max tensile strain ep3 (Max principal strain)	-0.5, -1.0	-0.5, -1.0	-0.5, -1.0	-0.5, -1.0
Normal stress s11	none	none	none	none
Normal stress s22	-1.0, -1.25	-1.0	none	none
Normal stress s33	-1.0	-1.0	none	none
Max comp. stress sp1 (Min principal stress)	-1.0, -1.25	-1.0, -1.25	none	none
Intermediate principal stress sp2	none	none	none	none
Min comp. stress sp3 (Max principal stress)	none	none	none	none
Strain energy density	-1.0, -1.25, -1.5	-1.0, -1.25	-1.0	-1.0
Mean normal stress	-1.0	-1.0	-0.5	none
Third stress invariant	none	none	none	none

Table 5.2: Determination of relevant stimulus. Eighteen strain measures are used in the search for relevant stimulus. The table shows the receptor locations in mm for which the shape of the SSRP matches that of the recorded SRP for three step shapes.

location that is common to all three steps. The SSRPs based on all the 18 strain measures were obtained for all the three steps at 10 receptor locations and plots similar to that in Figures 5-4 through 5-7 were obtained. From these figures the receptor locations which match the experimental SRP were obtained. Table 5.2 lists the receptor locations for which the SSRP based on the strain measures matched that of the experiments for step 1, step 3 and step 5 and also locations which are common to all three step shapes.

Thus it can be seen that there are only four quantities that have a common receptor location that can match the shape of the experimental SRP for all the three step shapes - maximum compressive strain ep1, maximum tensile strain ep3, shear strain e13, and strain energy density. These four quantities are therefore considered as possible candidates for

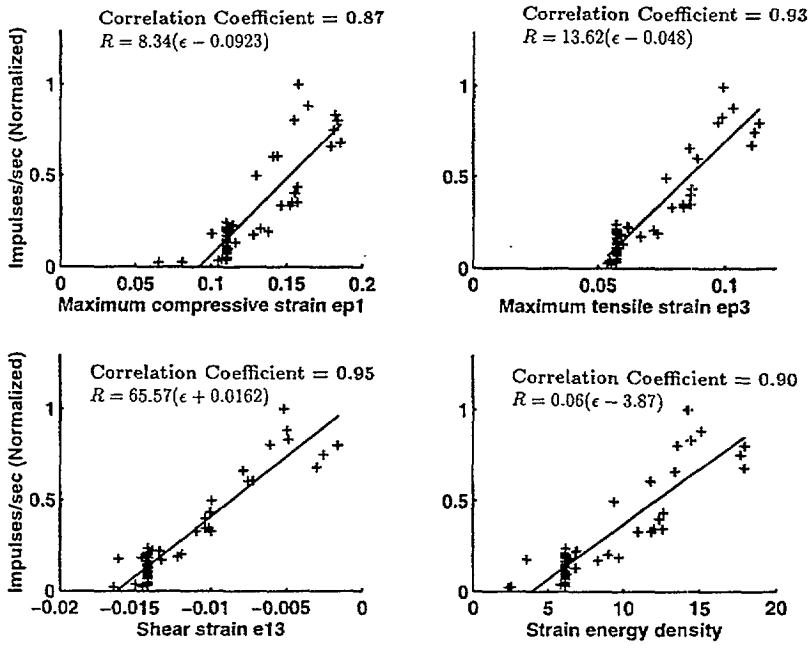

Figure 5-8: Recorded neural discharge rates vs computed candidate measures based on data for sinusoidal steps 1, 3 and 5, plotted for the four relevant stimulus candidates. The goodness of fit and the best linear model are indicated for each of the candidates. All the values for the candidate measures were extracted from the receptor located at -1.0 mm.

relevant stimulus for the SA-I receptors.

5.3.5 Goodness of fit for the four candidates based on step indentations

Figure 5-8 shows the plot of experimentally recorded neural response for all the three steps against each of the four strain measures. The best linear fit is shown by a straight line. The best strain measure is the one which has minimum spread or equivalently maximum correlation coefficient. It can be seen that shear strain e13 has the highest correlation coefficient. However the best fit model for e13 suggests that the threshold is -0.016 and all values of e13 below that value will evoke no response. The other quantities, ep1, ep3 and strain energy density have positive thresholds. It is to be noted that in relating the e13 strain to the neural responses, the absolute value was not chosen (as was done for ep1) because e13 was not negative at all locations.

5.3.6 Predicted neural response for step indentations

Figure 5-9 shows the predicted neural responses for the three steps based on the four candidate strain measures. It can be seen that the strain measures, maximum compressive strain, maximum tensile strain and strain energy density are able to predict the experimentally recorded by Srinivasan and LaMotte (1987) in the case of steps 1 and 3. In the case of step 5, the three strain measures predict a higher value for the SSRP as compared to the recorded SRP. The shear strain e13 is able to predict well the SRP for all three step shapes.

Thus based purely on sinusoidal step shapes, there are four candidates for the relevant stimulus for SA-I receptors - maximum compressive strain ep1, maximum tensile strain ep3, shear strain e13, and strain energy density. Of these four, shear strain e13 is a slightly better candidate in terms of predicting the recorded SRP.

5.3.7 Indentation by rectangular bars

Dependence of SSRP on receptor location

Figure 5-10 shows the SSRPs for the case of indentation by a 3 mm wide rectangular bar. Only the four strain measures, maximum compressive strain ep1, maximum tensile strain ep3, shear strain e13 and strain energy density, which emerged as likely candidates from the results on step indentations, are used. As in the case of step indentations, results for five receptor locations are shown. It can be seen that once again the SSRP depends on the location of the receptor. In the case of ep1, ep3 and strain energy density the receptor located close to the center of the finger shows the peak-dip-peak characteristic of the recorded SRP (Figure 5-1 (b)). In the case of e13 strain, none of the receptors show the peak-dip-peak characteristic.

Figure 5-11 shows the SSRPs for the case of indentation by 1.5 mm wide rectangular bar. Again, the SSRP depends on the location of the receptor. In the case of e13, none of the receptors show the dip at the center. The results are similar to that of the 3 mm wide bar, but the dip at the center is seen to be less.

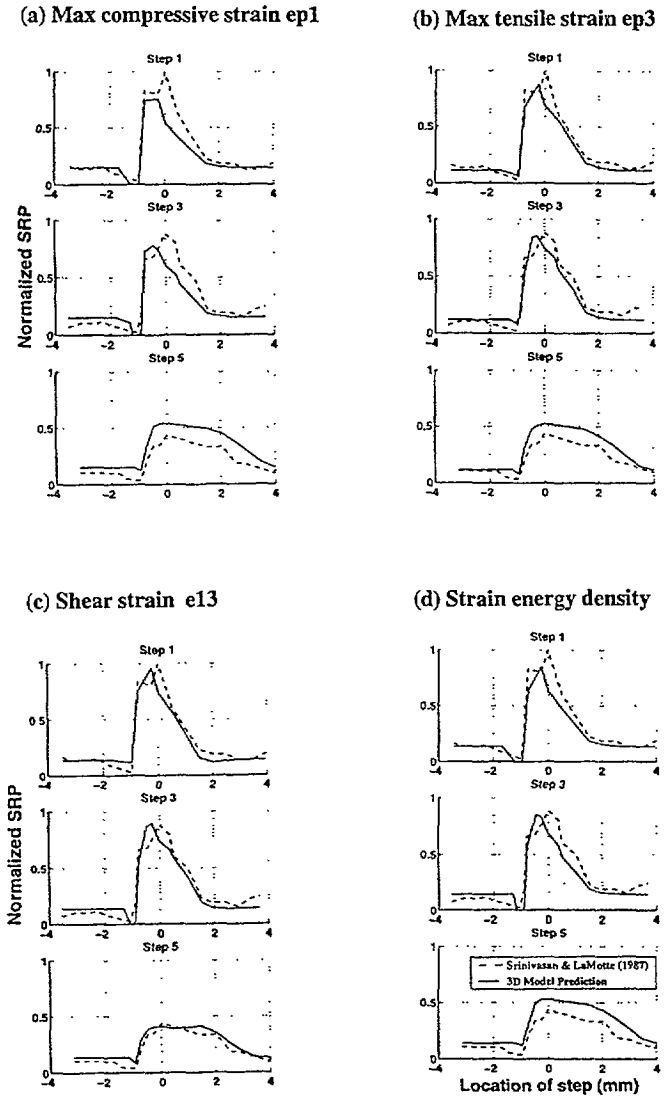

Figure 5-9: Comparison of predicted SRP (solid line) and recorded SRP (dashed line) for the three step shapes plotted for each of the four relevant stimulus candidates. All the four candidates are able to predict the shape of the three recorded SRP quite well. Maximum compressive strain ep1, maximum tensile strain ep3, and strain energy density generally underestimate the response for steps 1 and 3, and overestimate the response for step 5. The shear strain e13 is able to predict the response for all the three steps well.

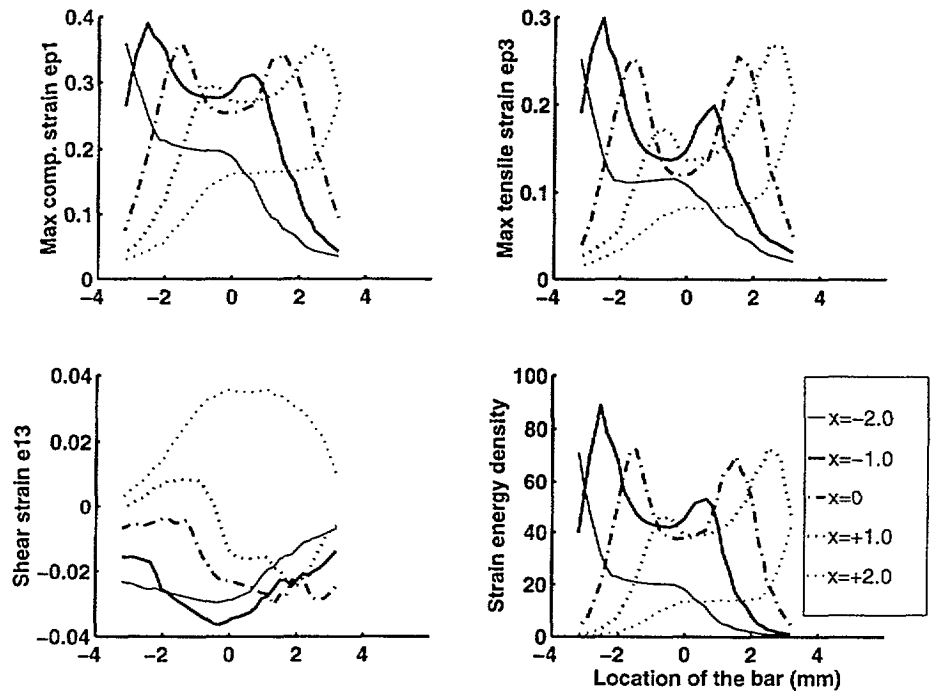

Figure 5-10: SSRPs for indentation by 3 mm wide rectangular bar, used in the experiment by Phillips and Johnson (1981a). In the case of maximum compressive strain ep1, maximum tensile strain ep3, and strain energy density, the receptors at the center of the finger pad show the symmetric edge enhancement effects present in the recorded SRP (Figure 5-1 (b). At other locations, the SSRP for a receptor at a positive location is nearly the mirror image of the SSRP for the receptor at a corresponding negative location. For example, the SSRP at x=- 2.0 mm is the mirror image of the SSRP at x=+2.0 mm. Shear strain e13 does not show the peak-dip-peak characteristic of the recorded SRP.

5.3.8 Goodness of fit for the four candidates based on bar indentations

Figure 5-12 shows a plot of experimentally recorded neural responses (Phillips and Johnson, 1981a) for both the 3 mm and 1.5 mm wide bars against each of the four candidates. The straight line shows the best linear fit. It can be seen that ep1, ep3 and strain energy density fit the recorded data fairly well. The e13 shear strain, however, does not fit the recorded data at all and has a very low correlation coefficient. Among ep1, ep3 and strain energy density, strain energy density has the highest correlation coefficient.

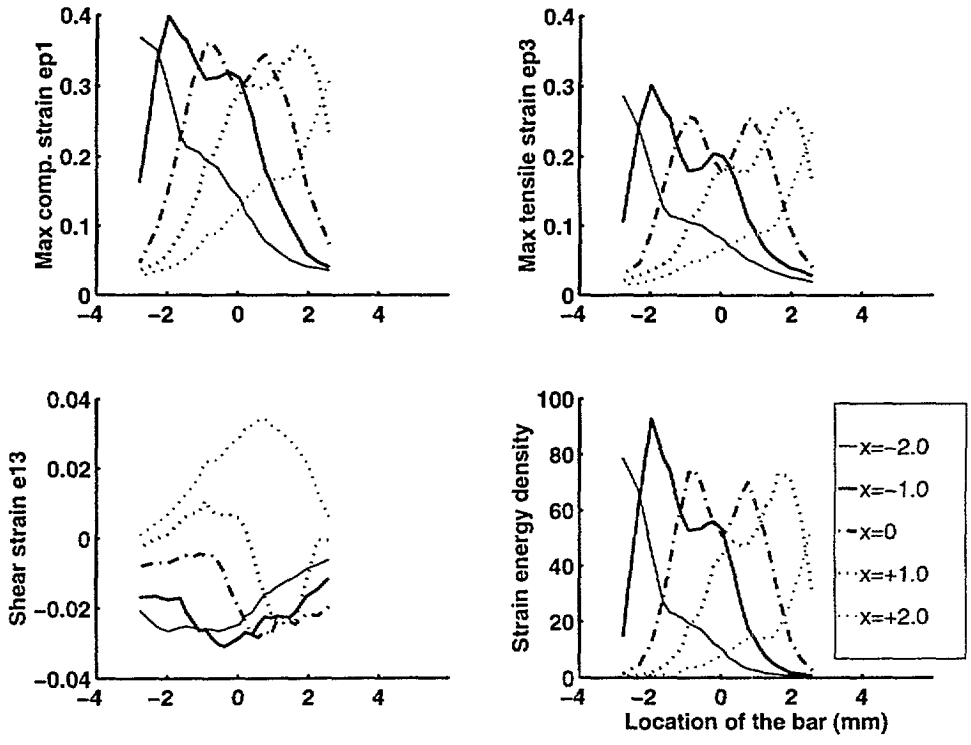

Figure 5-11: SSRPs for indentation by 1.5 wide rectangular bar, used in the experiment by Phillips and Johnson (1981a). As in the case of 3 mm bar (Figure 5-10), only the SSRP for the receptor close at the center of the finger pad shows the symmetric edge-enhancement due to the two edges of the bar. Shear strain e13 does not show the edge enhancement and its shape does not match the recorded SRP.

Predicted SRP for bar indentations

Figure 5-13 shows the predicted neural responses for both the 3 mm and 1.5 mm wide bars based on the four strain measures. The measures ep1, ep3 and strain energy density all show the dip at the center and have two peaks that correspond to the two edges of the bars. The prediction is better in the case of 3 mm bar than the 1.5 mm bar. It is to be pointed out that rectangular bars have sharp edges at their ends and to simulate the indentation of such shapes, the mesh density should be high enough so that the deformed mesh can approximate the high curvature. This is particularly important if the width of the bar is small, in which case the bar width becomes comparable to the element size. Previous attempts with low mesh density models did not show the sharp dip at the center of the 1.5 mm wide bar (Dandekar and Srinivasan, 1996). The current model has a much higher mesh density and has been found to be able to show the dip at the center. The reduced

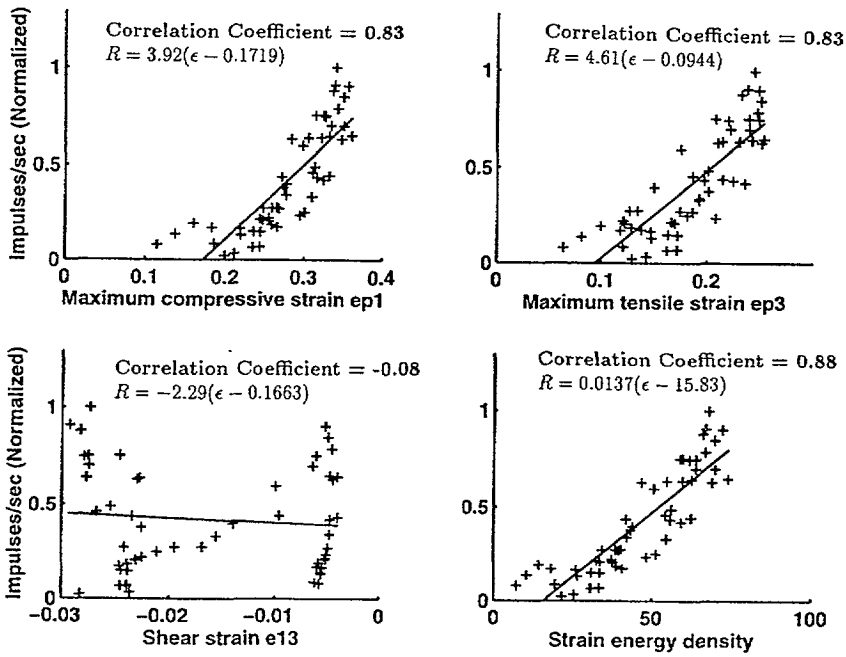

Figure 5-12: Recorded neural discharge rate vs. computed candidate measures based on data for 3 mm and 1.5 mm wide rectangular bars, plotted for the four relevant stimulus candidates. The goodness of fit and the best linear model are indicated for each of the candidates. All the values for the candidate measures were extracted from the receptor located at 0 mm. Of the four candidates, good linear fits are obtained from maximum compressive strain ep1, maximum tensile strain ep3, and strain energy density. Shear strain e13 does not fit the recorded neural data at all.

dip at the center in the case of 1.5 mm bar is due to the artifact of the simulation and arises because the element size cannot be made infinitesimally small. It is expected that with an even higher mesh density the prediction will be better and the correlation coefficients will also be higher. The shear strain e13 does not predict the neural response of either of the bars. Based on the results of bar indentations, it is unlikely that shear strain e13 is a candidate for the relevant stimulus of SA-I receptors.

5.4 Discussion

This chapter focused on the identification of the relevant stimulus for the SA-I afferents. The relevant stimulus provides the link between the mechanical stresses and the neural re-

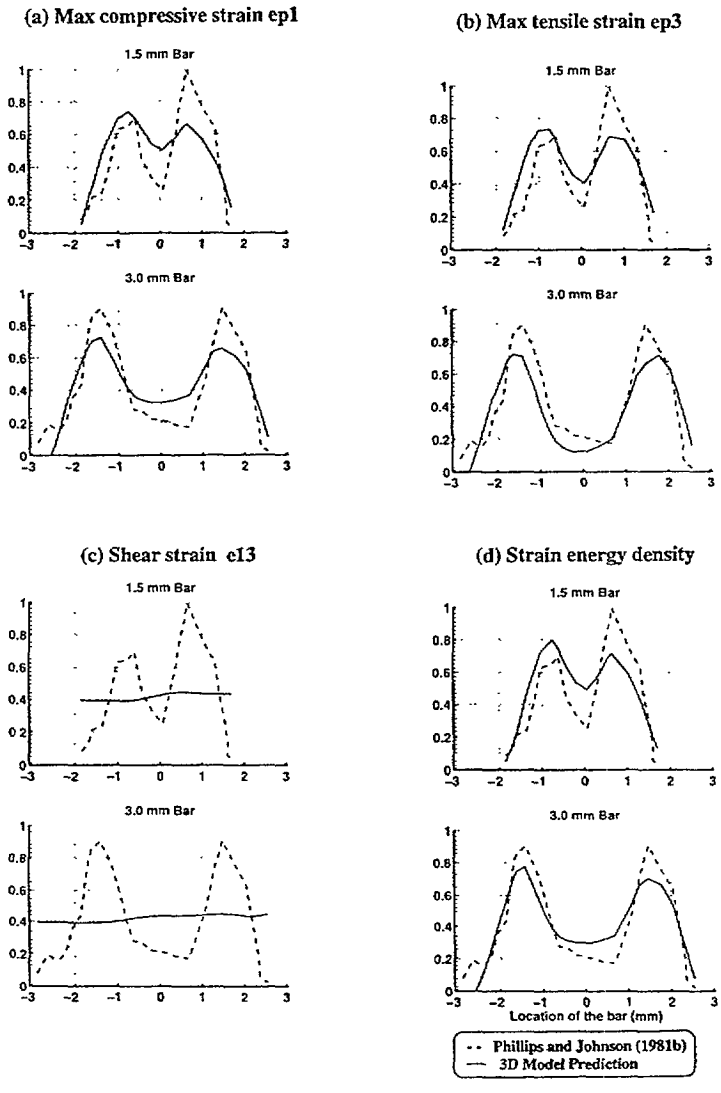

Figure 5-13: Comparison of computed SSRP and recorded SRP for the two rectangular bars. Three candidate measures, the maximum compressive strain ep1, maximum tensile strain ep3, and strain energy density, are able to predict the recorded SRP. The prediction is better for the case of the 3 mm bar than for the 1.5 mm bar, owing to the spatial resolution limitations in the simulations. The smaller the bar, the higher the resolution of the mesh that is needed to model the indentation accurately. Hence for the same mesh density, the prediction is better for the 3 mm bar. Shear strain e13 is not able to predict the recorded SRP.

sponses. The study of relevant stimulus requires experimental data of neural recordings. Currently, such data is available for indentation experiments for two indentors. Based on simulations with the first class of indentors (sinusoidal steps), the long list of 18 strain measures was reduced to four. Based on further simulations with the second class of indentors (rectangular bars), only three measures remained. These are maximum compressive strain, maximum tensile strain, and strain energy density. Maximum compressive strain was found to be the relevant stimulus for SA-I afferents based on the simplified model by Phillips and Johnson (1981b). The present study which uses a more realistic model has shown that there are two additional strain measures that are also candidates for the relevant stimulus. The correlation coefficients of fit for the above three candidate measures are almost equal. Hence purely based on the current work, it is not possible to determine the best candidate among the three. However based on physical considerations it might be possible to argue in favor of one of them. Strain energy density is a measure of the distortions at a point and is also orientation independent. Both maximum compressive strain and maximum tensile strain are orientation dependent and hence the receptors must be oriented in a certain direction if they are to code these strains. Strain energy density is thus likely to be a better candidate. It is possible that further simulations might reduce the list further.

6 Decoding

The previous two chapters dealt with coding of object information into neural responses by the SA-I mechanoreceptors. This chapter deals with the inverse problem of decoding – how a central processing unit like CNS would decode the neural responses to obtain information about the object that contacted the finger. In order to study the problem of decoding we introduce the idea of non-linear shift-invariant systems. The motivation for using this approach is that well developed tools like convolution, which are used to analyze linear shift-invariant systems, can be applied to model the tactile system even in the presence of certain non-linearities. The use of linear and shift-invariant approach to model systems have led to significant advances in other fields such as vision, telecommunications and radar.

6.1 Linear Systems

A system is an abstraction of anything that takes an input, operates on it, and produces an output (Karu, 1995). The actual physical process, when viewed as a system, can then be represented as a mathematical transformation between the input and the output. In general this transformation may not be unique, may be non-linear etc. Figure 6-1 shows a systems representation of the human tactile encoding process. The input to the system is the pressure distribution on the surface of the finger. The output is the neural response from a population of afferent nerve fibers. The transformation describes the way the surface pressure is converted into neural response, which depends on the mechanics of the fingerpad and the receptor transduction.

In certain classes of systems, the transformation may obey superposition and scaling –

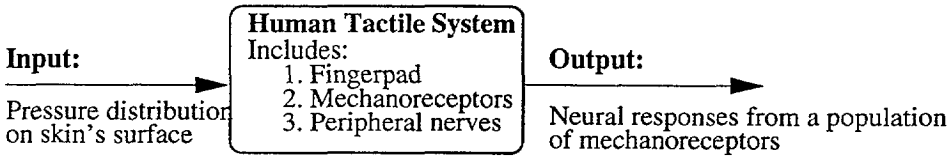

Figure 6-1: Input-output model of the human tactile encoding process.

the output due to two different inputs is the sum of the outputs due to the individual inputs, and scaling the input by some factor, also scales the output by the same factor. Such systems, which obey superposition and scaling are called *linear systems*. Based on the studies in the previous chapters, the human tactile system is seen to be non-linear for two reasons: (1) the relevant stimulus for SA-I afferents (maximum compressive strain, maximum tensile strain, or strain energy density) is a non-linear combination of the individual stress/strain measures and (2) the receptor model has a threshold parameter which also makes the transformation non-linear. This is true even for the case where the materials inside the finger are considered linear elastic, and the deformations that occur are considered small – that is, even if both material and geometric linearity are assumed to hold good.

6.2 Shift-Invariant Systems

A system is shift-invariant if a shift in the input leads to an identical shift in the output. When we say that the input is shifted, we mean that location of all the loads on the surface of the finger is laterally shifted. We now evaluate under what conditions shift-invariance holds true. Figure 6-2 shows a generic mechanical system – some loads are applied to the surface and there is a boundary which imposes a constraint that no point on that boundary can move. Load P1 (at location A) leads to a certain distribution of stresses and strains within the system. If the same load is applied at another point B (denoted as P2), then the stress-strain distribution will be more or less identical, except that they are now laterally shifted because the load itself has been shifted. If we assume that all the mechanoreceptors are identical, the distribution of neural responses will also be a simple shift compared to the distribution due to P1. Thus, between the loads P1 and P2, there is no difference in the behavior of the system except for a shift in the position. However an identical load applied

to point C, or D will not lead to a simple shift in the distribution of stresses and strains. This is because there is a difference in geometry at these points. Between points A and C, point C is closer to the fixed boundary and hence will not undergo the same mechanical behavior as the point A. Between points A and D, point D has a larger local curvature and hence the mechanical behavior at point D will not be identical to that at point A. However points A and B are similar in that both have the same local curvature and are both far away from the fixed boundary. Hence while the mechanical system is shift-invariant with respect to points A and B, it is not shift-invariant with respect to points A and C, or A and D. It is also evident that, even in the case of constant curvature (between points A and B), one has to compute strains and stresses in a curvilinear coordinate system – the cartesian stress and strain components will obviously change if the point of application of load is changed. In this chapter, we assume that the finger is more or less flat so that the stresses and strains can be computed in the xyz cartesian coordinate system. This assumption is however not required to develop the systems approach. Also such an assumption does not mean that the curvature of the finger can be neglected as this will mean that the contact of shaped objects cannot be simulated accurately. This assumption only simplifies the computation required. We now state the conditions under which shift-invariance for mechanoreceptor response holds good:

- The curvature of the body must be constant over the region where shift-invariance is evaluated.
- The boundary conditions should be far away from the region of where shift-invariance is evaluated.
- All the mechanoreceptors should be identical.

The human finger does not have a constant curvature. Also during touch, not all points of contact will be far away from the nail region that imposes the fixed boundary conditions. Also, the mechanoreceptors are not identical to one another. Hence the human tactile is not, in general a strictly shift-invariant system.

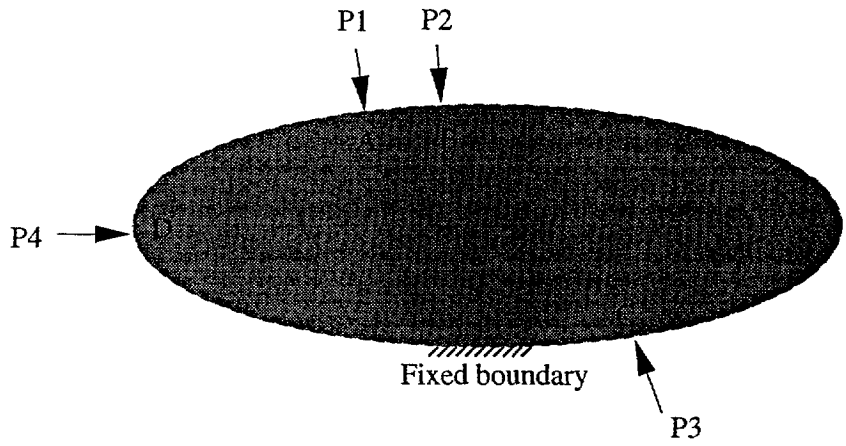

Figure 6-2: Illustration of shift-invariance. Both points A and B are located far away from the boundary and the surface curvature is same at both points. If the material distribution around points A and B is the same, both the points see the same conditions in terms of geometry and material distribution. Hence the stress strain distributions due to one of them, is simply the stress strain distributions due to the other, but shifted by a distance equal to the distance between the two points. However a loading at C is quite different from that at A or B because of the fixed boundary condition. Also the loading at D is different because the curvature at point D is different from that at A or B.

6.3 Idealizations of the real system

Thus the tactile system is neither linear nor shift-invariant in a strict sense. We now make simplifying assumptions that can help us make the problem more tractable. First we consider the shift-invariance property. If the loading on the finger is such that the area of contact is quite small, the curvature of the finger within the area of contact will be nearly constant. Also, if only the pulp region in the fingerpad is used for tactile sensing, the region of contact will be quite far away from the nail region which imposes the fixed boundary condition. With the further assumption that all the mechanoreceptors are identical, we can then model the finger as being approximately shift-invariant within the region of contact. We also note that since the region of contact is considered small, we can always define a local coordinate system that is cartesian. Similar assumptions of shift-invariance, though broad in nature, have led to significant advancements in fields like robot vision (Horn, 1986). Next we consider the linearity property.

In all the simulations described in this thesis (Chapter 3-5), both material and geometric linearity have been assumed. This assumption is valid as long as the deformations

inside the finger are small. We now assume that the threshold in the receptor model is very small and can be neglected. This linearizes the receptor mechanics. However, we are still left with one non-linearity – all the three possible relevant stimuli (maximum compressive strain, maximum tensile strain and strain energy density) are non-linear measures of the cartesian stress-strain components. Of the three, we will consider strain energy density, which for physical reasons is likely to be a better candidate than the other two. The non-linearity in strain energy density arises because it is a weighted sum of the *product* of the cartesian stresses and strains. We will retain this non-linearity in our further analyses. To summarize, based on our assumptions, we are left with a *non-linear but shift-invariant system* [1].

In order to further simplify our analysis, we limit ourselves to the case of plane-strain, incompressible problems. This assumption, however, is not a requisite for our further analysis, but simplifies our analysis. Under these conditions the expression for strain energy density becomes (Dieter, 1988)

$$\text{Sener} = G(e_{11}^2 + e_{22}^2 + 0.5e_{12}^2) \tag{6.1}$$

where Sener is the strain energy density, G is the Shear Modulus of the material where the strain energy density is computed, and e_{11}, e_{22}, and e_{12} are the three components of the strain tensor under plane-strain assumptions.

6.4 Illustration of Shift-Invariance

We now illustrate that the assumption of shift-invariance is reasonable for the human tactile system. A point load (spatial impulse) was applied to the high resolution finite element model of the fingertip (Chapter 3) and the strain energy distribution was computed at a depth of 760 microns from the surface. The simulation was repeated 24 times after changing the location of the load each time. In all the simulations, the load had the same magnitude and was applied normal to the surface. The locations of the load are shown in Figure 6-3.

[1] It is to be noted that the individual stresses and strains are linear with respect to the loads applied on the surface when contact region does not change with loading.

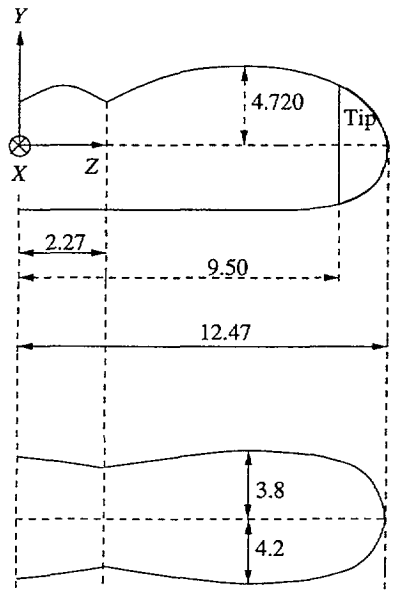

Loc #	X (mm)	Y (mm)	Z (mm)	
1	1.403	2.996	4.068	
2	1.677	3.696	5.009	
3	1.832	4.067	5.983	
4	1.907	4.239	6.893	
5	1.917	4.243	7.807	
6	1.818	4.013	8.809	
7	0.094	3.656	4.067	
8	0.098	4.380	5.204	
9	0.100	4.720	6.137	
10	0.098	4.839	6.893	Top region
11	0.099	4.752	7.958	
12	0.100	4.358	8.993	
13	-2.100	3.282	4.084	
14	-2.370	3.726	5.208	
15	-2.507	3.940	6.136	
16	-2.528	3.987	7.047	
17	-2.413	3.806	7.961	
18	-2.180	3.425	8.997	
19	1.668	3.627	9.761	
20	0.913	2.438	11.501	
21	0.111	4.003	9.754	Tip region
22	0.055	2.643	11.510	
23	-1.987	3.104	9.752	
24	-1.569	1.977	11.500	

Figure 6-3: Locations of the point load used to test shift-invariance. The first 18 locations are located on the top portion of the finger and the last six locations are located at the tip of the finger. All dimensions are in mm.

Figure 6-4 shows an example of the point load simulation when the load is located at location # 10. The *point spread function,* which is the distribution of strain energy density [2] to the point load, is seen to be more or less radially symmetric. This radial symmetry helps us to reduce the 2D distribution into a 1D distribution:

$$\text{Sener} = \frac{A}{r^m} \tag{6.2}$$

where Sener is the strain energy density, A is a scaling parameter and m is an exponent. The data was fit so as to obtain the best A and m through the least squared error method.

[2] which is also the same as the distribution of neural response if we assume that the threshold is zero and that all mechanoreceptors are identical and continuously distributed.

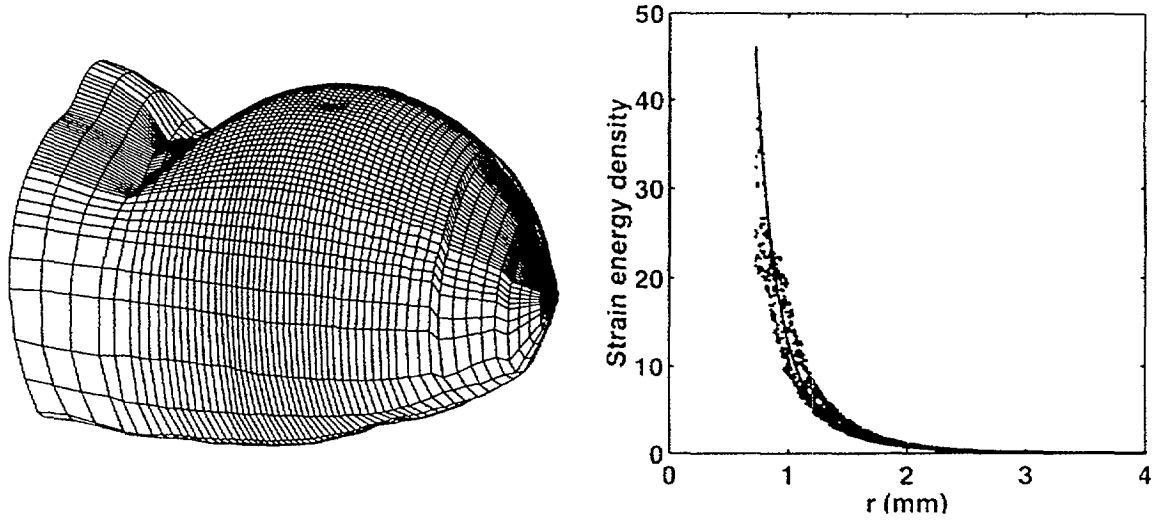

Figure 6-4: A point load applied to the finger. The left panel shows the deformed mesh. The right panel shows the *point spread function* -- strain energy density has been plotted as a function of the radial distance between the point of application of load and the point at which the strain energy density is computed (r). The distribution was found to fit the model $Sener = \frac{12.8}{r^{3.96}}$ with a correlation coefficient of 0.96, thus indicating radial symmetry.

This procedure was repeated for all the 24 locations and the best fit model was obtained at each location and the obtained values of A and m are tabulated in Table 6.1. Two features are evident from the table: First, for each location, the correlation coefficient is high. This indicates that it is possible to use radial symmetry to reduce the 2D distribution into a 1D distribution. Second, for the first 18 locations, the model parameters do not vary much from location to location. The standard deviation in the parameters A and m are only 10% and 4.8% of the mean respectively. If we accept an error of 10%, then we can say that the strain energy density distribution does not change considerably within the 18 locations (which included the top portion of the finger). Thus the distribution of strain energy density, is approximately shift-invariant within that region. When all the 24 locations are included, the standard deviations in the parameters A and m increase to 17.7% and 6.2% and the shift-invariance is less likely to hold true. This is to be expected, based on the discussion in Section 6.2.

Location #	A	m	R^2
1	9.094	3.881	0.954
2	11.754	3.792	0.975
3	11.373	3.732	0.984
4	11.493	3.738	0.987
5	12.293	3.777	0.983
6	11.907	3.798	0.980
7	11.854	3.983	0.963
8	12.851	3.981	0.978
9	13.629	4.041	0.980
10	12.805	3.959	0.961
11	13.975	4.082	0.980
12	13.369	4.172	0.980
13	12.820	4.272	0.971
14	13.176	3.999	0.979
15	11.967	3.828	0.986
16	10.990	3.666	0.988
17	10.285	3.548	0.987
18	11.168	3.698	0.983
19	17.464	4.189	0.974
20	14.760	4.301	0.888
21	20.042	4.336	0.982
22	14.671	4.320	0.909
23	14.757	3.957	0.990
24	14.619	4.470	0.915
Mean (all 24 loc)	13.046	3.98	0.969
Std (all 24 loc)	2.315	0.246	0.027
Mean (first 18 loc)	12.045	3.886	0.978
Std (first 18 loc)	1.231	0.189	0.01

Table 6.1: Model parameters ($Sener = \frac{A}{r^m}$) for strain energy density for all the locations. R^2 is the correlation coefficient of the fit.

6.5 System Identification using Impulse Response Functions

With the simplifying assumptions made in Section 6.3, the computation of neural responses reduces to the computation of the strain energy density distributions as described by Equation 6.2 [3]. The coding problem, then requires the computations of the three strain components. Since the strain components anywhere in the finger are linear functions of the load applied on the surface and are also shift-invariant, these components, for an arbitrary

[3]Since the threshold is assumed to be zero, the neural response is a scaled value of strain energy density.

loading, can be obtained as a convolution of impulse response functions and the applied load function:

$$e_{11}[n] = h[n] * P[n] \tag{6.3}$$

$$e_{22}[n] = g[n] * P[n] \tag{6.4}$$

$$e_{12}[n] = f[n] * P[n] \tag{6.5}$$

The function h[n] represents the e_{11} strain distribution due to an impulse load on the surface of the finger. Similar meanings hold for g[n] and f[n]. In the above equations, the '*' symbol represents the convolution operation, the argument [n] is used to denote the discrete spatial coordinate [4], and P[n] is the load distribution applied on the surface of the finger. The convolution operation for discrete signals is defined as

$$e_{11}[n] = \sum_{i=-\infty}^{\infty} h[i]P[n-i] \tag{6.6}$$

Once e_{11}, e_{22} and e_{12} are obtained, strain energy density can be computed. In order to obtain the functions h[n], g[n] and f[n], a point load was applied to a 2D finite element model on the surface and the distributions of the three strain components were obtained at a depth of 760 microns from the surface. Figure 6-5 shows the three impulse response functions along with their (spatial) frequency responses. It can be seen that h[n] and g[n] are almost identical except for a difference in sign, which is expected since the material has been assumed to be nearly incompressible. The functions h[n] and g[n] are found to be low pass filters whereas f[n] is found to be a bandpass filter.

The systems representation of the tactile system can now be expressed in terms of a block diagram and is shown in Figure 6-6. This representation also includes a noise term N(n) which is assumed to occur at the input to the mechanoreceptor (sensor). The encoding problem is the computation of neural responses, given the surface loads (surface pressure distribution). This can be easily accomplished by using Equation 6.2. However the decoding problem, which is the computation of surface pressure distribution from the

[4]The function h[n] is simply a digitized (sampled) version of the continuous e_{11} distribution. In the computations described here, all the samples are spaced 170 microns apart.

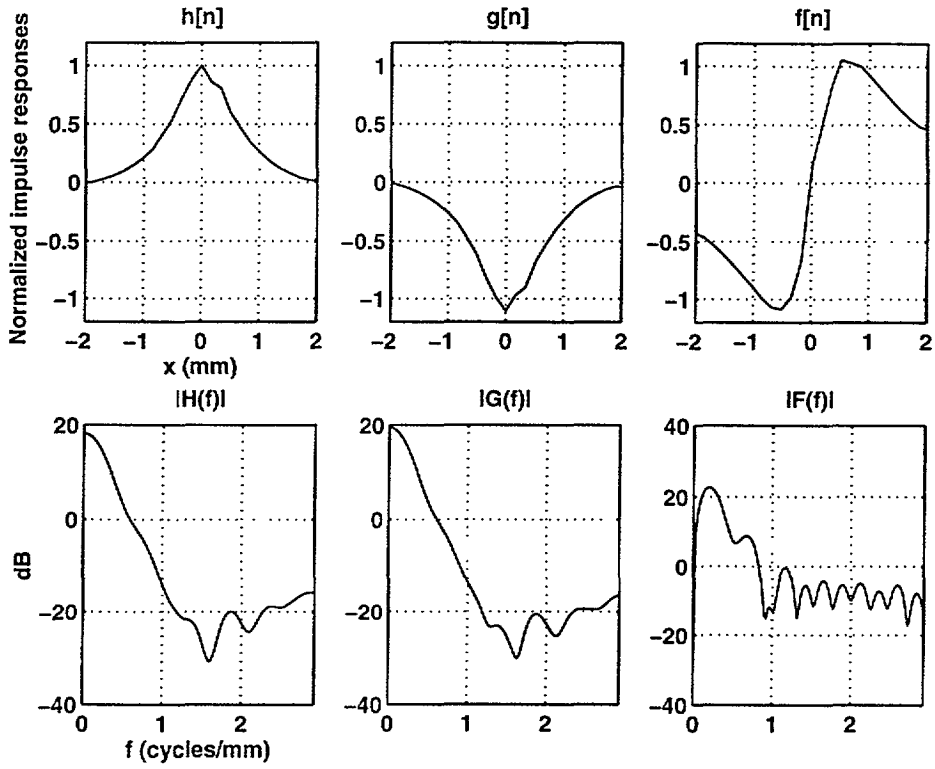

Figure 6-5: Impulse response functions for e_{11}, e_{22} and e_{12} and their (spatial) frequency responses. For example h[n] is the distribution of e_{11} strain when an impulse load is applied to the surface of the finger. For the frequency response, only the magnitude is plotted. Note that $e_{11} \sim e_{22}$ because of plane strain assumption and nearly incompressible material.

neural responses, is not trivial, since the overall system is non-linear and hence an inverse transform cannot be taken. In the remainder of this Chapter, we develop an iterative method to solve this decoding problem.

6.6 Decoding as an Optimization Problem

We treat the problem of decoding as an optimization problem, where the aim is the find the best surface load distribution P[n] that optimizes some performance criterion. The criterion adopted here is the minimization of the square of the error of the output defined as:

$$Error = \sum_{n=0}^{M-1} (R_p[n] - R[n])^2 \tag{6.7}$$

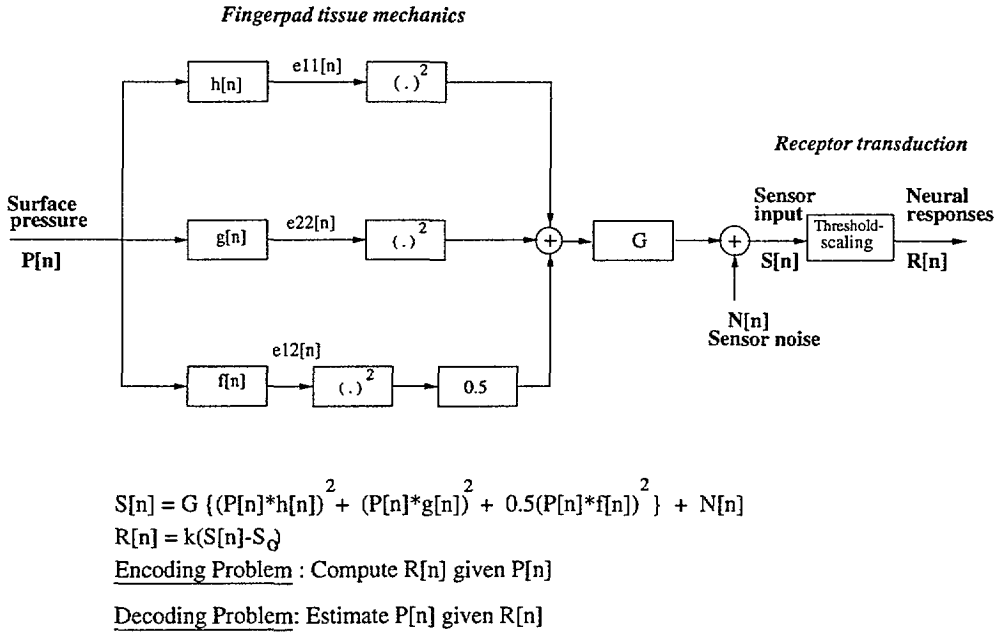

Figure 6-6: Block diagram representation using impulse response functions. If the threshold parameter in the receptor model is neglected, R[n] is a scaled version of S[n] and without loss of generality we can take S[n] to be the neural response.

where $R[n]$ is the known output, $R_p[n]$ is the output computed from P[n] and M is the length of the output R[n]. The best P[n] is taken to be the one that minimizes the above error. Again we reiterate that, since the threshold value in the receptor model is assumed to be zero, strain energy density can be considered as the neural response (that is we use R[n] and S[n] interchangeably in Figure 6-6).

To solve the above non-linear optimization problem, the *univariate method* (Rao, 1984) is employed. As the length of P[n] is known beforehand (Length(P[n] = Length(R[n]-Length(h[n]+1), the problem is to find N numbers that minimize the error in Equation 6.7, where N = Length(P[n]). Since the *vector* P[n] has in general length greater than 1, this is a multidimensional problem. In the univariate method, this is converted to several one-dimensional problems. The method starts by assuming P[n] to be some arbitrary value for all the N values of n. Then the first element of P[n] namely P[0] is changed with all other P[n] held at constant values and for each value of P[0] the error described in Equation 6.7 is evaluated. The P[0] that leads to the minimum error is taken to be the best P[0]. For example if P[0] can take any of 1000 values, the error function is computed for all the 1000

possible values of P[0] and the one for which the error is minimum is chosen. A similar procedure is done for the other P[n] – each time only one element of P[n] is changed with the other elements held constant and a one-dimensional problem is solved. When one such cycle is completed for all n, the procedure is repeated again till no more reduction in error can be obtained. The algorithm that describes this procedure is shown in Figure 6-7.

It is to be noted that the univariate method does not rely on gradients. The method is simple to implement. Theoretically it can be applied to find the minimum of any function that possesses continuous derivatives. However if the function to be minimized has a steep valley, the method may not converge. This situation usually arises when the search space for each of the P[n] is not fine enough. Further details about this method can be found in Rao (1984). In the next section we demonstrate the univariate method through an example.

6.7 Example of Optimal Decoding using the Univariate Method

To demonstrate the univariate method we use an input that has a length 2. In this and the following sections, the input P[n] will be referred to as x[n] and the output R[n] (or S[n]) will be referred to as y[n], which is consistent with the notation used in Signal Processing literature. We first consider the case when there is no sensor noise, i.e., N[n] is zero. Figure 6-8 shows an input x[n] = [20 14], and the corresponding output y[n] computed using the expression in Figure 6-6. The problem at hand is to use only y[n] to compute the input x[n] which is assumed unknown. The solution can then be checked with the known x[n] to see if the method worked.

Figure 6-9 shows the error as a function of x0 and x1, the two elements of the vector x[n]. The error is seen to be minimum for x = [20 14]. Figure 6-10 shows the method in action. The procedure starts by assuming the solution space to be [x0 x1] = [10 10] (arbitrarily chosen). At the end of the first attempt the solution becomes [24 10]. After that the solution proceeds along a diagonal path till it reaches the correct solution.

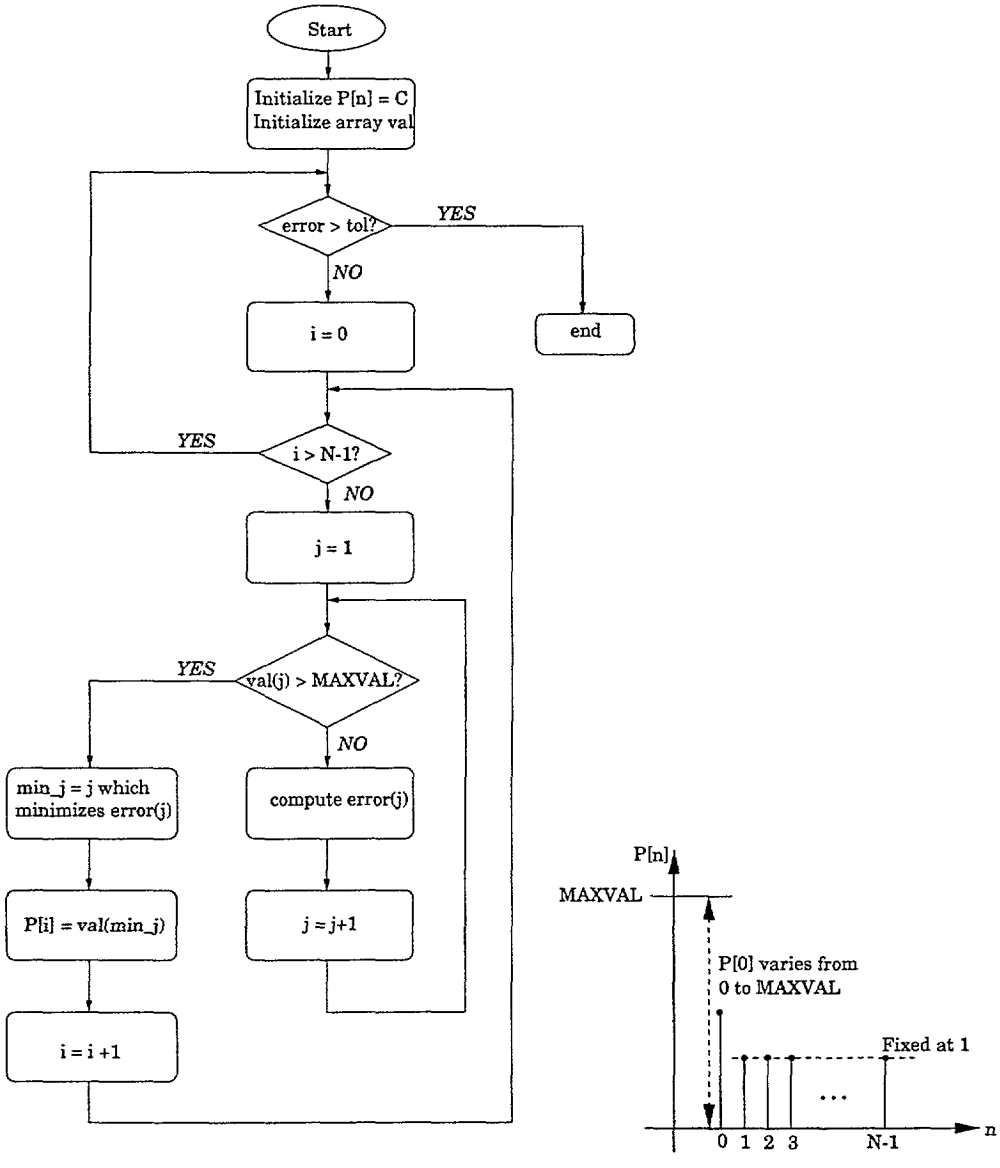

Figure 6-7: Algorithm describing the univariate method.

6.8 Decoding in the Presence of Noise

So far we have considered the case when there is no sensor noise. We now consider the practical case where some noise is present in the system. The encoding process is essentially a low pass filtering process. Hence decoding, which is an inverse operation, is a high pass filtering process and hence any noise present in the system will degrade the decoding process. Thus it becomes interesting to see the effects of noise on the efficiency of the univariate method.

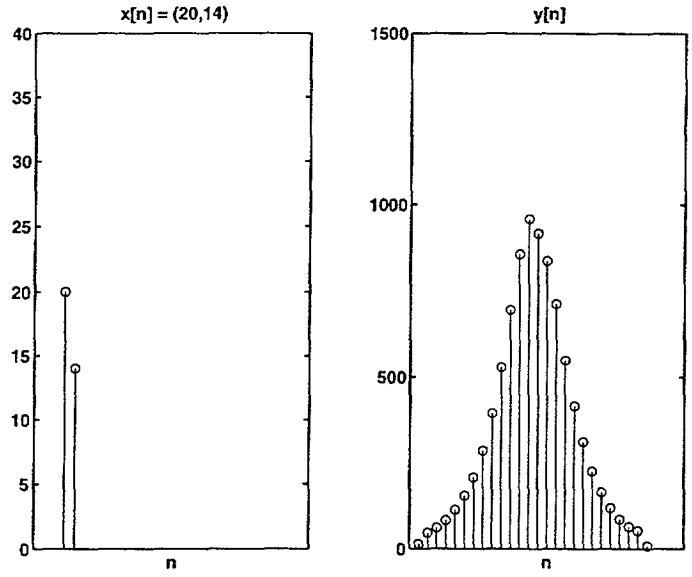

Figure 6-8: Input x[n] and the corresponding y[n] chosen to illustrate the working of the univariate method. The input is chosen to be of length 2 for simplicity.

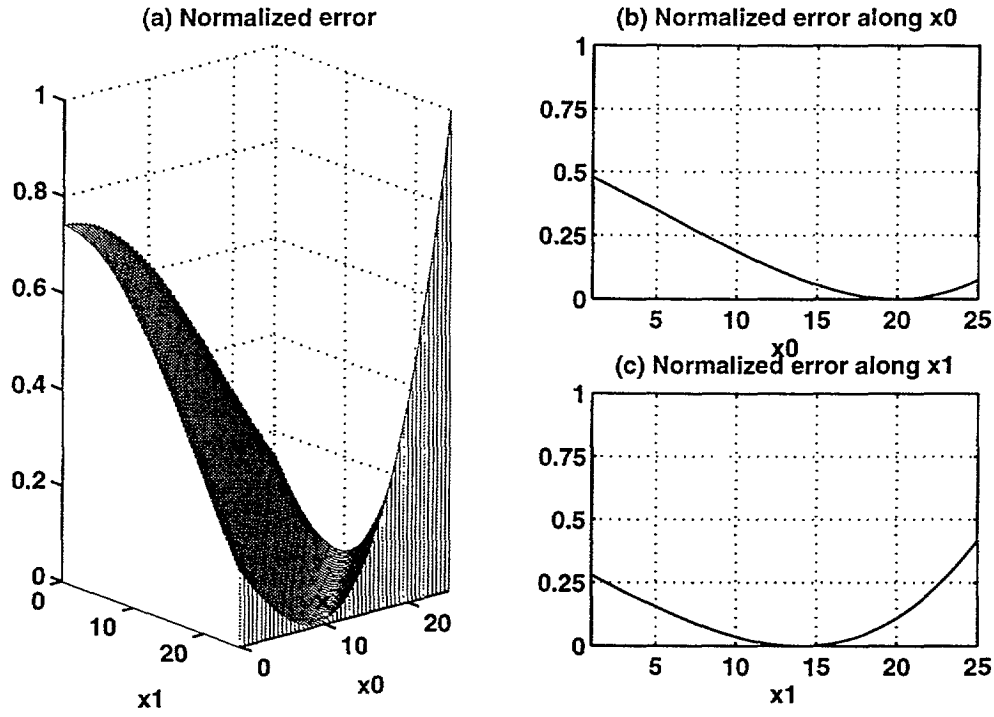

Figure 6-9: Error function for the example problem. Panel (a) shows the error as a function of x0 and x1, the two elements of the input vector. Panels (b) and (c) show the projection of the error function along the two axes. The error is seen to be minimum at x = [20 14] -- shown by the 'x' mark in (a).

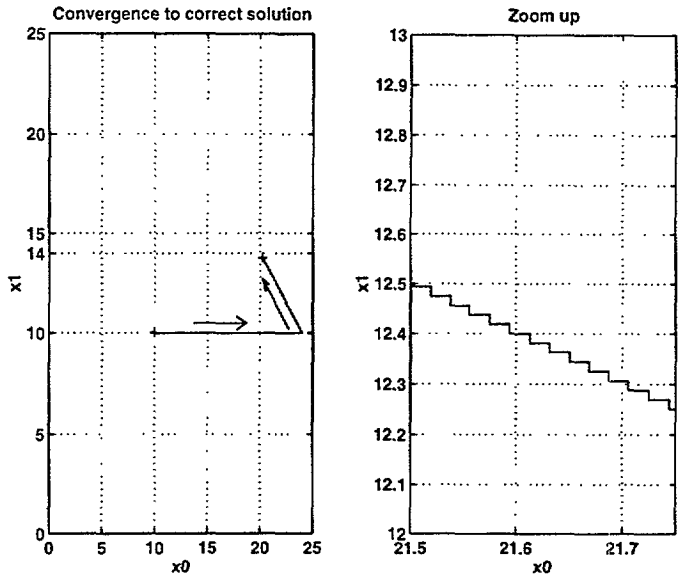

Figure 6-10: Working of the Univariate method. The left panel shows that the solution converges to the correct solution x=[20 14]. The right panel shows that what appears as a straight line is actually a crisscross path in the solution space.

For illustration purpose, we assume that the noise is zero-mean additive and Gaussian distributed. The output (neural responses) is thus the sum of the ideal output (output as computed by the convolution expressions) and the noise. The relative strength of the noise that is added can be varied by varying its variance. Larger variance for the noise leads to smaller SNR (measured at the output) [5]. The univariate method was used in decoding for various values of SNR. Figure 6-11 shows an example for the case when the SNR is about 10 dB. It is seen that in this case the decoding process does not converge to the correct solution.

In order to quantify how successful the decoding process was, we define a normalized error term:

$$\text{Decoding error} = \frac{\sum_{n=0}^{N-1}(x[n] - x_y[n])^2}{\sum_{n=0}^{N-1} x[n]^2} \tag{6.8}$$

where $x[n]$ is the actual input (correct solution) and $x_y[n]$ is the decoded input (as obtained through the univariate method). Figure 6-12 shows the error as a function of SNR. As expected, the error in decoding decreases with increasing SNR. If we accept 10% error to

[5] The SNR is defined as $10\log_{10}(\frac{\text{Variance of signal}}{\text{variance of noise}})$.

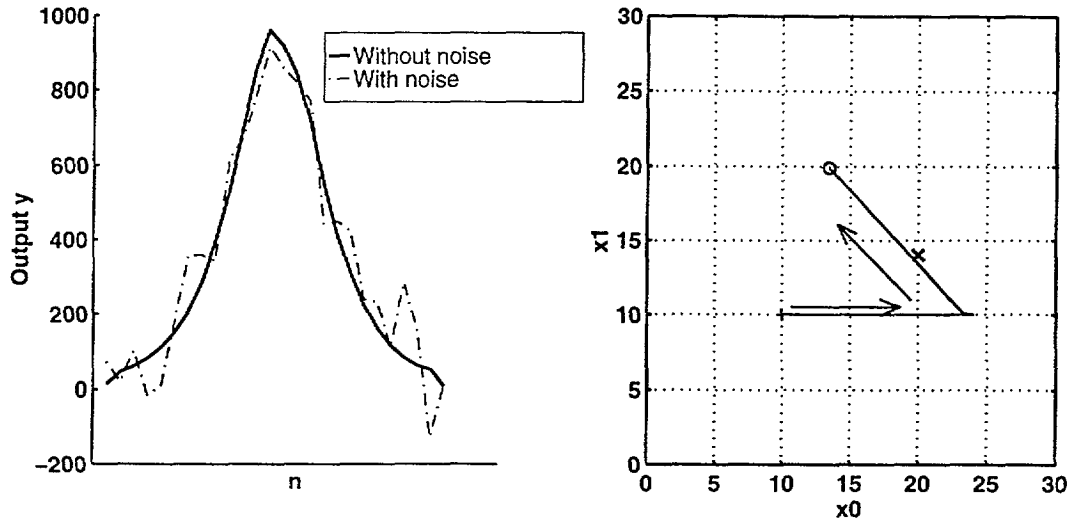

Figure 6-11: Decoding in the presence of noise. The left panel shows the output with and without noise. The noise is zero-mean additive Gaussian noise and the SNR is about 10 dB. The left panel shows the path taken by the solution space. The 'x' mark indicates the correct solution. The '+' and 'o' marks indicate the starting and ending points for the solution space. It is seen that the solution does not converge to the correct solution.

be within the reliability limits, then we can say that the decoding process works for SNR values above 20 dB. It is also to be noted that since the noise is random, even for the same SNR, there is some variability in the decoding process. In Figure 6-12 this variation is shown by the standard deviation. The standard deviation is also seen to decrease with increasing SNR.

6.9 Summary of Systems Approach

The systems approach described here models the human tactile system in terms of input-output relationships. The surface pressure is the input and the neural response is the output. The finger is in general a non-linear and shift-variant system. Using certain assumptions we were able to show that the system could be approximated shift-invariant but non-linear system. The forward encoding process, namely, the computation of neural responses is simplified because the individual stresses and strains are linear functions of the surface loads, and the neural responses can be computed after computing the cartesian stresses and strains. However, the decoding process is significantly more difficult because there is no general way to invert the non-linear transformation. The univariate method

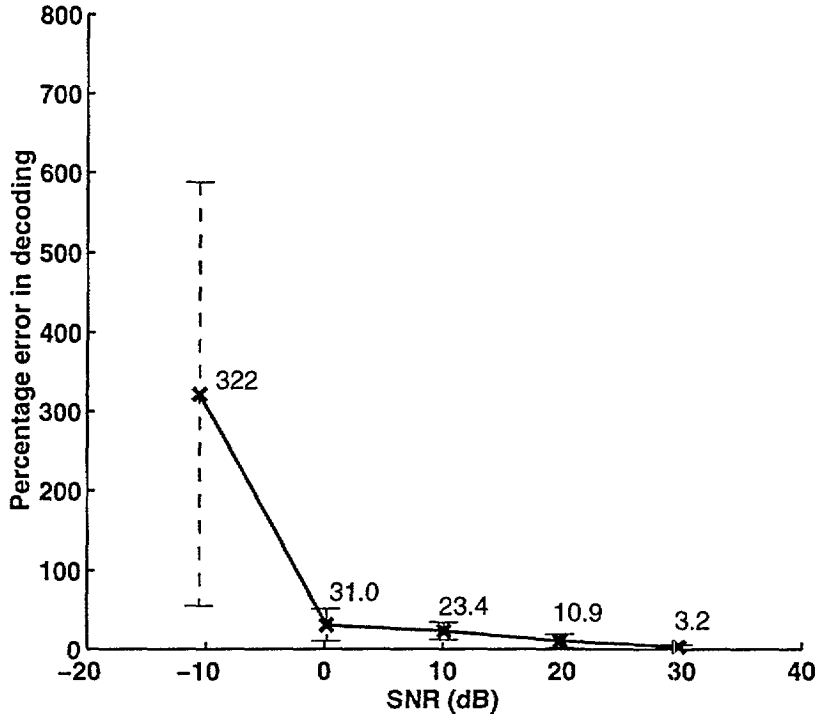

Figure 6-12: Percentage error as a function of SNR: mean values, shown with bars of one standard deviation from the mean. As SNR decreases both the mean error and the variation in the error increase. The mean values are also indicated next to each point.

used in optimization studies was proposed to solve the decoding problem and was illustrated with an example. The decoding problem is also prone to gross error due to noise. The analysis showed that decoding is reliable when the noise (assumed to be zero-mean additive Gaussian) is such that the SNR is greater than 20 dB.

The above results showed that decoding of tactile information is possible even in the presence of non-linearities. However the problem was quite complex and required several assumptions. It is quite likely that the human brain uses a simpler mechanism to decode tactile information. This could be, for example, a simple table look-up. However, even in that case, it is necessary for the brain to create the look-up table in the first place. Such a learning, or training process could be the result of a more complicated computational scheme such as the one discussed in this chapter. Further research in memory acquisition and learning would help to provide a clearer understanding about the information processing processes of the brain.

7 Summary and Future Work

7.1 Summary

This thesis was concerned with biomechanical bases of human tactile sensing, their implications to the neural behavior of mechanoreceptors embedded in the skin, and the development of a systems approach to encoding and decoding of tactile information.

7.1.1 Model development

In order to study the mechanics of contact between the finger and the object, a high resolution three dimensional finite element model of the primate fingertip was developed. The material distribution was inhomogeneous, but assumed to be linear elastic. The model had an element size of about 170 μm on the top surface. The mechanical behavior of the model was validated by comparing simulation results with data available from experiments on surface displacements under line loads.

7.1.2 Biomechanical studies

The model was used to simulate biomechanical experiments of indentation of different shaped objects (rectangular bars, cylinders and sinusoidal step shapes) on the finger. The surface pressure distributions was obtained for each indentation. The pressure was found to be highly dependent on the curvature of the object that indented the finger. Based on the results, a simple model for surface pressure as a function of the local skin displacement and the curvature of the indentor was developed. Subsurface strain measures at a depth of 760 microns from the surface were also obtained. The results showed that the subsurface strain measures were low pass filtered versions of the surface pressure, and different strain measures had different distributions. For example, strain energy density was able to

capture the distribution of surface pressure better than axial stress.

7.1.3 Neurophysiological studies

The model was also used to simulate neurophysiological experiments, for which neural responses of afferent nerve fibers when the shaped objects are indented onto the finger were available. The *spatial response profile* obtained through simulations (SSRP) was compared with available experimental spatial response profiles for three sinusoidal step shapes and two rectangular bars. The comparison was done for 18 different stress-strain measures (3 normal stresses, 3 principal stresses, 3 normal strains, 3 shear strains, 3 principal strains, and 3 invariants). The results showed that three measures, namely maximum compressive strain, maximum tensile strain, and strain energy density were likely candidates for the *relevant stimulus* for SA-I afferent nerve fibers innervating the finger. Among these, strain energy density is a better candidate as it is a scalar and the mechanoreceptors need not be oriented in any specific direction to encode the relevant stimulus.

7.1.4 Systems approach

The thesis also developed the idea of a systems approach to human tactile sensing. The distribution of loads on the surface of the finger can be considered as the input and the corresponding neural responses from a population of mechanoreceptors can be considered as the output. The encoding process, i.e., the computation of the neural responses given the surface loads is trivial as the relevant stimulus can be computed after the cartesian stress-strain components are computed. The individual stresses and strains being linear measures (under certain assumptions detailed in Chapter 6) can be computed as a simple convolution of the surface loads and respective impulse response functions. However, decoding, which is the inverse process of computing the surface loads given the neural responses, is a non-trivial process as the non-linear transformation cannot be generally inverted. The decoding process was solved as an optimal estimation problem using the univariate method. The decoding process was estimated to be reliable for SNR greater than 20 dB, where the noise (assumed to be zero-mean additive Gaussian noise) is added to the neural responses.

7.2 Future Work

There are two main approaches which the author feels would aid studies in human tactile sensing. The first approach is modeling the behavior of the tactile system. The current study was limited to study of shape coding under static conditions, by the SA-I afferents. Dynamic tactile sensing is more involved in that the surface pressure distributions are both space and time dependent, the material properties are viscoelastic, and the receptors also have their own dynamics. The systems approach can be extended to include the dynamic effects and other receptors. The current work dealt mainly with convex shapes. The work can be extended to study the contact mechanics of indentation of concave rigid objects.

The decoding operation was demonstrated only for an example. In order to demonstrate the full potential, the decoding process should be demonstrated using surface pressure distribution with shaped objects. Once the pressure distributions are decoded from the neural responses, the shape of the object (i.e. its curvature) can be obtained. The use of more robust decoding strategies such as genetic algorithms could also be investigated.

The shape of an object is only one of the attributes of the object that is coded by the neural responses. Other attributes include the object's compliance, and texture. The work can be extended to such studies wherein a relationship between the object's attribute and surface pressure would need to be evaluated (similar to Equation 4.1, Section 4.5.1). Such studies may require the incorporation of finger ridge mechanics.

The second approach is the understanding of the physical basis of touch. This approach is quite distinct from the modeling approach and in fact, can be argued to be the inverse. In modeling, one does experiments or simulations and tries to develop mathematical relationships between the observed quantities. In tactile sensing this has been mostly a "black-box" approach. However in the physical approach, one strives to understand why the black-box is behaving the way it is. For example consider the following statement regarding information processing in the visual system: "The rods and cones in the retina do not directly transduce the light stimuli into action potentials – they produce only graded potentials, which are then utilized by a set of intermediate cells to generate action

potentials" (adapted from Weiss (1996)). Such statements do not include mathematical relationships, but provide a fundamental understanding about the visual system. The physical approach uses data from experiments or simulations to see if a physical process can be explained without resorting to mathematical relationships. Such studies are likely to enhance our knowledge about not only the tactile system, but also take us closer to a more complete understanding of the human brain, the most complex system in the known universe.

References

Abaqus, , *ABAQUS/Standard User's Manual*, Hibbit, Karlsson & Sorensen, Pawtucket, RI, **1995.**

Bolanowski, S. J., Gescheider, G. A., Verillo, R. T., and Checkosky, C. M., "Four channels mediate the mechanical aspects of touch," *J.Acoust.Soc.Am*, vol. 84, no. 5, pp. 1680–1694, **1988.**

Dandekar, K. and Srinivasan, M. A., "Role of mechanics in tactile sensing of shape," *RLE Technical Report - 604, MIT*, **1996.**

Darian-Smith, I., "The sense of touch: Performance and peripheral neural processes," *Handbook of physiology - The nervous system -III*, pp. 739–788, **1984.**

Dieter, G. E., *Mechanical Metallurgy*, McGraw-Hill Book Company, New York, **1988.**

Fearing, R. S. and Hollerbach, J. M., "Basic solid mechanics for tactile sensing," *International Journal of Robotics Research*, vol. 4, no. 3, pp. 40–54, **1985.**

Fung, Y. C., *Biomechanics*, Springer-Verlag, New York, **1981.**

Gauss, C. F., "Disquisitiones generales circa superficies curvas," *Commentationes Societatia Regiae Scientiarum Gottingenesis Recentiores*, vol. 6, pp. 99–146, **1827.**

Gonzalez, R. C. and Wintz, P., *Digital Image Processing*, Addison-Wesley, Reading, MA, **1987.**

Goodwin, A. W., John, K. T., and Marceglia, A. H., "Tactile discrimination of curvature by humans using only cutaneous information from the fingerpads," *Experimental brain research*, vol. 86, pp. 663–672, **1991.**

Gulati, R. and Srinivasan, M., "Determination of mechanical properties of the human fingerpad , in vivo, using a tactile stimulator," *RLE Technical Report - 606, MIT*, **1996.**

Ho, C.-H. and Srinivasan, M., "Human haptic discrimination of thickness," *RLE Technical Report - 608, MIT*, **1996.**

Horn, B. K. P., *Robot Vision*, MIT Press, Cambridge, Massachusetts, **1986.**

Howe, R. S. and Cutkosky, M. R., "Dynamic tactile sensing: Perception of fine surface features with stress rate sensing," *IEEE Transactions on Robotics and Automation*, vol. 9, no. 2, pp. 140–151, **1993.**

Johansson, R. S., "Tactile sensibility in the human hand: Receptive field characteristics of mechanoreceptive units in the glabrous skin area," *J. Physiol*, vol. 281, pp. 101–123, **1978.**

Johansson, R. S. and Vallbo, A. B., "Tactile sensibility in the human hand: Relative and absolute densities of four types of mechanoreceptive units in glabrous skin," *Journal of Physiology (London)*, vol. 286, pp. 283–300, **1979.**

Johansson, R. S. and Vallbo, A. B., "Tactile sensory coding in the glabrous skin of the human hand," *Trends in Neuroscience*, vol. 6, pp. 27–32, **January 1983.**

John, K. T., Goodwin, A. W., and Darian-smith, I., "Tactual discrimination of thickness," *Experimental brain research*, vol. 78, no. 1, pp. 62–68, **1989.**

Johnson, K. O. and Phillips, J. R., "Tactile spatial resolution - I. Two point discrimination, gap detection, grating resolution and letter recognition," in *J. Neurophysiol* (Phillips and Johnson, 1981b), pp. 1177–1191.

Karason, S. P., Annaswamy, A., and Srinivasan, M. A., "Identification and control of haptic systems: A computational theory," *RLE Technical Report - 621, MIT*, **1998.**

Karu, Z. Z., *Signals and Systems Made Ridiculously Simple*, ZiZi Press, Cambridge, Massachusetts, **1995.**

Knibestol, M., "Stimulus-Response functions of rapidly adapting mechanoreceptors in the human glabrous skin area," *J. Physiol*, vol. 232, pp. 427–452, **1973.**

Knibestol, M., "Stimulus-Response functions of slowly adapting mechanoreceptors in the human glabrous skin area," *J. Physiol*, vol. 245, pp. 63–80, **1975**.

Knibestol, M. and Vallbo, A., "Single unit analysis of mechanoreceptor activity from the human glabrous skin," *Acta Physiol Scand*, vol. 80, pp. 178–195, **1970**.

Lamb, G. D., "Tactile discrimination of textured surfaces: Psychophysical performance measurements in humans," *Journal of Physiology (London)*, vol. 338, pp. 551–565, **1983**.

LaMotte, R. H. and Srinivasan, M. A., "Responses of cutaneous mechanoreceptors to the shape of objects applied to the primate fingerpad," *Acta Psychologica*, vol. 84, pp. 41–51, **1993**.

Lanir, Y., "Skin mechanics," in *Handbook of Bioengineering*, ch. 11, pp. 11.1–11.25, McGraw-Hill, **1987**.

Lederman, S. J. and Taylor, M. M., "Fingertip force, surface geometry, and the perception of roughness by active touch," *Perception & Psychophysics*, vol. 12, pp. 401–408, **1972**.

Lockhart, R. D., Hamilton, G. F., and Fyfe, F. W., *Anatomy of the Human Body*, J P Lippincott Co., Philadelphia, **1965**.

Loewenstein, W. R. and Skalak, R., "Mechanical transmission in a pacinian corpuscle. An analysis and a theory," *J. Physiol*, vol. 182, pp. 346–378, **1966**.

Loomis, J. M., "An investigation of tactile hyperacuity," *Sensory Processes*, vol. 3, pp. 289–302, **1979**.

Loomis, J. M. and Lederman, S. J., "Tactual perception," in *Handbook of perception and human performance*, ch. 31, pp. 31.1–31.41, John Wiley & Sons, **1986**.

Mountcastle, V. and Powell, T., "Central nervous mechanisms subserving position sense and kinesthesis," *Bulletin of the Johns Hopkins Hospital*, vol. 105, pp. 173–200, **1959**.

Mountcastle, V., LaMotte, R., and Carli, G., "Detection thresholds for stimuli in humans and monkeys: Comparison with thresholds events in mechanoreceptive afferent nerve fibers innervating in the monkey hand," *J. Neurophysiol*, vol. 35, pp. 122–136, **1972**.

O'Rahilly, R., "Skin, hair, and nails," in *Anatomy: A Regional Study of the Human Structure* (Gardner, E. and O'Rahilly, D. G. R., eds.), W. B. Saunders and Co., **1969**.

Pati, Y. C., Friedman, D., Krishnaprasad, P. S., Yao, C. T., and Peckerar, M. C., "Neural networks for tactile perception," *Proceedings of the IEEE Conference on Robotics and Automation*, pp. 135–139, **1988**.

Pawluk, D. T. V., *A Holistic Model Of The Human Sense of Touch and a Dynamic Contact Model of the Human Fingerpad*. PhD thesis, Harvard University, **1997**.

Phillips, J. R. and Johnson, K. O., "Tactile spatial resolution - II. Neural representation of bars, edges and gratings in monkey afferents," in *J. Neurophysiol* (Phillips and Johnson, 1981b), pp. 1192–1203.

Phillips, J. R. and Johnson, K. O., "Tactile spatial resolution - III. A continuum mechanics model of skin predicting mechanoreceptor responses to bars, edges and gratings," *J. Neurophysiol*, vol. 46, pp. 1204–1225, **1981b**.

Rao, S. S., *Optimization: Theory and applications*, Halsted Press, New York, **1984**.

Rossi, D. D., Caiti, A., Bianchi, R., and Canepa, G., "Fine-form tactile discrimination through inversion of data from a skin-like sensor," *Proceedings of the IEEE International Conference on Robotics and Automation*, pp. 398–403, **1991**.

Serina, E. R., *Characterization and modeling of the fingertip pulp under repeated loading*. PhD thesis, University of California at Berkeley, **1997**.

Speeter, T. H., "Three dimensional finite element analysis of elastic continua for tatile sensing," *International Journal of Robotics Research*, vol. 11, no. 1, pp. 1–19, **1992**.

Srinivasan, M. A., "Surface deflection of primate fingertip under line load," *J. Biomechanics*, vol. 22, no. 4, pp. 343–349, **1989**.

Srinivasan, M. A. and Dandekar, K., "An investigation of the mechanics of tactile sense using two-dimensional models of the primate fingertip," *Journal of Biomechanical Engineering*, vol. 118, pp. 48–55, **1996**.

Srinivasan, M. A. and LaMotte, R. H., "Tactual discrimination of softness," *J.Neurophysiol*, vol. 73, no. 1, pp. 88–101, **1995**.

Srinivasan, M. A. and LaMotte, R. H., "Tactile discrimination of shape: Responses of slowly and rapidly adapting mechanoreceptive afferents to a step indented into the monkey fingerpad," *Journal of Neuroscience*, vol. 7, no. 6, pp. 1682–1697, **1987**.

Srinivasan, M. A. and LaMotte, R. H., "Encoding of shape in the responses of cutaneous mechanoreceptors," in *Information Processing in the Somatosensory system* (Franzen, O. and Westman, J., eds.), Wenner-Gren Intl. Symposium series, pp. 59–69, Macmillan Press, **1991**.

Talbot, W. H., Darian-Smith, I., Kornhuber, H. H., and Mountcastle, V. B., "The sense of flutter-vibration: Comparison of the human capacity with response patterns of mechanoreceptive afferents from the monkey hand," *J.Neuorphysiol*, vol. 31, pp. 301–334, **1968**.

Thomine, J., "The skin of the hand," in *The Hand* (Tubiana, R., ed.), vol. 1, ch. 6, pp. 107–120, W. B. Saunders and Co., **1981**.

Tregear, R. T., *Physical Functions of Skin*, Academic Press, New York, **1966**.

Verillo, R. T., Fraioli, A. J., and Smith, R. L., "Sensation magnitude of vibrotactile stimuli," *Perception & Psychophysics*, vol. 6, pp. 366–372, **1969**.

Weiss, T. F., *Cellular biophysics*, MIT Press, Cambridge, **1996**.